DEVELOPMENT OF ORGANIC AND ORGANIC-INORGANIC HYBRID SOLAR CELLS

By

P VEERENDER

(ENGG01201004007)

Bhabha Atomic Research Centre, Mumbai

A thesis submitted to the

Board of Studies in Engineering Sciences

In partial fulfillment of requirements

for the Degree of

DOCTOR OF PHILOSOPHY

of

HOMI BHABHA NATIONAL INSTITUTE

January, 2014

STATEMENT BY AUTHOR

This dissertation has been submitted in partial fulfillment of requirements for an advanced degree at Homi Bhabha National Institute (HBNI) and is deposited in the Library to be made available to borrowers under rules of the HBNI.

Brief quotations from this dissertation are allowable without special permission, provided that accurate acknowledgement of source is made. Requests for permission for extended quotation from or reproduction of this manuscript in whole or in part may be granted by the Competent Authority of HBNI when in his or her judgment the proposed use of the material is in the interests of scholarship. In all other instances, however, permission must be obtained from the author.

P VEERENDER

DECLARATION

I, hereby declare that the investigation presented in the thesis has been carried out by me. The work is original and has not been submitted earlier as a whole or in part for a degree / diploma at this or any other Institution / University.

P VEERENDER

List of Publications arising from the thesis

Journals:

1. **P. Veerender**, V. Saxena, A.K. Chauhan, S.P. Koiry, P. Jha, A. Gusain, S. Choudhury, D.K. Aswal, S.K. Gupta, Probing the annealing induced molecular ordering in bulk heterojunction polymer solar cells using in-situ Raman spectroscopy, Solar Energy Materials and Solar Cells, 120 (2014) 526-535.

2. **P. Veerender**, S.P. Koiry, P. Jha, V. Saxena, A.K. Chauhan, S. Bhattacharya, R. Tewari, D.K. Aswal, S.K. Gupta, An Electrochemical Approach for Deposition of Polyfullerene Films on ITO Substrates, Journal of The Electrochemical Society, 159 (2011) D13-D18.

3. N. Ramgir, M. Ghosh, **P. Veerender**, N. Datta, M. Kaur, D.K Aswal, S.K. Gupta, Growth and gas sensing characteristics of p-and n-type ZnO nanostructures, Sensors and Actuators B: Chemical, 156 (2011) 875-880.

4. V. Saxena, **P. Veerender**, A.K. Chauhan, P. Jha, D.K. Aswal, S.K. Gupta, Efficiency enhancement in dye sensitized solar cells through co-sensitization of TiO2 nanocrystalline electrodes, Applied Physics Letters, 100 (2012) 133303-133304.

5. **P. Veerender**, V. Saxena, P. Jha, S.P. Koiry, A. Gusain, S. Samanta, A.K. Chauhan, D.K. Aswal, S.K. Gupta, Free-standing polypyrrole films as substrate-free and Pt-free counter electrodes for quasi-solid dye-sensitized solar cells, Organic Electronics, 13 (2012) 3032-3039.

Conference proceedings:

1. **P. Veerender**, V. Saxena, A. Gusain, P. Jha, S.P. Koiry, A.K. Chauhan, D.K. Aswal, S.K. Gupta, Effect of Co-sensitization and acid treatment on TiO_2 photoanodes in dye-sensitized solar cells, AIP Conference Proceedings, 1512 (2013) 778.

2. **P. Veerender**, A. Jain, A. Gusain, V. Saxena, D.K. Aswal, S.K. Gupta, Dye Sensitized Solar Cells Based On Metal-Free Organic Dyes and Aqueous Electrolytes, Fuelling the Future: Advances in Science and Technologies for Energy Generation, Transmission and Storage, (2012) 168.

3. **P. Veerender**, A.K. Chauhan, V. Saxena, P. Jha, D.K. Aswal, S.K. Gupta, Reproducible bulk heterojunction polymer solar cell arrays, AIP Conference Proceedings, 1451 (2012) 70.

4. **P. Veerender**, S.P. Koiry, V. Saxena, P. Jha, A.K. Chauhan, D.K. Aswal, S.K. Gupta, Electrochemical polymerization of tetra-(4-hydroxyphenyl) porphyrin for organic solar cells, AIP Conference Proceedings, 1447 (2012) 727.

5. **P. Veerender,** V. Saxena, A. Gusain, P. Jha, S.P. Koiry, A.K. Chauhan, D.K. Aswal, and S.K. Gupta, Conducting polymers based counter electrodes for dye-sensitized solar cells, DAE-SSPS 2013, Patiala.

6. **P. Veerender,** V. Saxena, A. Gusain, S.P. Koiry, P. Jha, A.K. Chauhan, D.K. Aswal, and S.K. Gupta, A simple method for increasing the efficiency of Rhodamine 19 perchlorate based dye sensitized solar cells, Nanoenergy Symposia, 12 (2013) 163.

7. V. Saxena, **P. Veerender**, A.K. Chauhan, P. Jha, D.K. Aswal, S.K. Gupta, Metal-free organic dye for dye sensitized solar cells, AIP Conference Proceedings, 1447 (2012) 663.

8. V. Saxena, **P. Veerender**, S.P. Koiry, A.K. Chauhan, D.K. Aswal, S. Mula, N. Shivran, S. Chattopadhyay, S.K. Gupta, Borondipyrromethane (BODIPY) as sensitizer for dye sensitized solar cell, AIP Conference Proceedings, 1451 (2012) 272.

9. V. Saxena, S.P. Koiry, **P. Veerender**, D.K. Aswal, S.K. Gupta, N. Shivran, S. Mula, S. Chattopadhyay, J. Yakhmi, A Simple Photoelectrochemical Cell Using Fe^{+3}/Fe^{+2} (aq) as Redox Couple, AIP Conference Proceedings, 1313 (2010) 400.

10. M. Ghosh, M. Kurian, **P. Veerender**, N. Padma, D.K. Aswal, S.K. Gupta, J. Yakhmi, Photovoltaic Properties Of ZnO Nanoparticle Based Solid Polymeric Photoelectrochemical Cells, arXiv preprint arXiv:1008.0112, (2010).

P VEERENDER

Dedicated to my parents

ACKNOLWDGEMENTS

The first and foremost, I take this opportunity to express my deepest gratitude to my research supervisors **Prof. S.K. Gupta** & **Prof. R. Tewari** for their continuous guidance, encouragement and support during the thesis work. I am greatly indebted to my mentor **Prof. D. K. Aswal**, who inspired me most during my research journey over last 4 years and encouraged me to see the positive side of every failure. His continued motivational pursuit has resulted in good peer reviewed journals and timely submission of this dissertation.

I am greatly indebted to **Dr. A. K. Chauhan, Dr. Vibha Saxena, Dr. S. P. Koiry, and Dr. P. Jha** for their help in carrying out experiments, learning various characterization techniques, continuous support and encouragement during the course of the work. Continuous discussions with them have strengthened my fundamentals and sharpened the new ideas proposed in the thesis.

I am extremely grateful to **Dr. S Bhattacharya**, **Dr. Niranjan Ramgir, and Dr. Soumen Samanta** for their continuous support and carrying out SEM images whenever I requested.

I owe my deepest gratitude to **Dr. K.P. Muthe, Dr. N. Padma, Dr. A. K. Debnath, Dr. Ajay Singh, Shri R. Prasad, Dr. Manmeet Kaur, Dr Ranu Bhat, Mrs Ranita Basu, Mrs Niyanta Dutta, Mrs K Ganapati and Shri K.N. Meshram** for extending support and help at various stages of the thesis work. I am also thankful to my labmates **Arvind, Nirav, Tanvi, Avani, and Abhay** for their help during the course of the work.

Last but not least, I would like to thank **my family and friends**, who have always motivated and supported me. I thank them for their unending support through difficult times, for believing in me, and for being there for me whenever I needed them most.

CONTENTS

CHAPTER 2 : Experimental and characterization techniques 57

SYNOPSIS

Currently the estimated energy requirement for the world population is about 13 terawatts (TW), which is expected to increase upto 25 TW by 2050. To meet this demand, it is desirable to explore all possible sources of available energy. Sunlight, an abundant energy resource is freely available and amount of energy reaching the surface of the earth is 120000 TW. Harvesting this energy directly from the sunlight using photovoltaic (PV) technology with efficiency of 10% could easily meet our demand for huge energy consumption. Since 1954, when the first modern Si p-n junction solar cell were invented at Bell labs, many efforts have been made in search of high-efficiency and low-cost solar cells, which lead to the advent of various photovoltaic technologies, such as, (i) crystalline Si cells (single crystal and multi-crystalline), (ii) single-junction GaAs, (iii) thin film photovotaics e.g. Cu(In,Ga)Se_2, CIGS, CdTe etc. These photovoltaic technologies require both high energy for processing and high purity materials, and in many cases use of toxic materials. In parallel, researchers discovered alternative photovoltaic technologies such as polymer solar cells, dye-sensitized solar cells, and quantum dot solar cells. During last two decades, polymer and dye sensitized solar cells have gained importance owing to their low material costs, ease of fabrication, high throughput, flexibility, etc. The maximum efficiency of ~15% in perovskite based dye sensitized solar cells has been reported. However, the reported efficiency of polymer and dye sensitized solar cells varies over a wide range of 0.1-15%. To understand this wide variation in efficiency, it is desirable to investigate various aspects of polymer and dye sensitized solar cells, including optimization of various device parameters, selection of appropriate materials, device structures and understanding of processes etc. In the case of polymer solar cells, light absorption, exciton dissociation, charge transport and collection are the primary concern for low efficiencies, whereas in the case of dye sensitized solar cells light absorption, electrolyte leakage/ evaporation, and electron recombination are the key issues. This thesis aims at solving some of these issues. The specific studies carried out during the thesis work are as follows:

(i) Understanding the *in-situ* morphology evolution of P3HT:PCBM blend as a function of temperature using Raman and optical microscope, and the relationship between the morphology and efficiency of the bulk-heterojunction polymer solar cells.

(ii) Studies on fabrication and characterization of porphyrin/polyfullerene diffuse bilayer solar cells and porphyrin-modified ZnO-NW/P3HT hybrid solar cells.

(iii) Studies on dye-sensitized solar cells fabricated using: (a) different photoanodes e.g. ZnO or TiO_2; (b) photoanodes sensitized using single or two dyes; (c) different electrolytes, liquid or gel; and (d) different counter electrodes, Pt or novel free-standing polypyrrole films.

Above mentioned investigations have been organized into five chapters and contents of each chapter are briefly discussed in the following.

Chapter 1: Introduction

In this chapter, we begin with the basics of solar energy and brief history of various solar technologies that have emerged during past three decades. This chapter introduces the basic concepts of silicon solar cells and their working mechanism with a schematic depiction. Current-voltage characteristics and photovoltaic parameters such as open-circuit voltage, short-circuit current density, and fill factor are introduced with equivalent circuit models. A brief history and illustrative working mechanism of polymer solar cells, dye-sensitized solar cells are presented. A literature survey has been carried out and major current issues pertaining to the polymer and dye-sensitized solar cells are discussed. The Chapter concludes by bring out the scope of the thesis.

Chapter 2: Experimental techniques

In this chapter we describe various tools used for the fabrication of the bilayer and bulk heterojunction polymer solar cells as well as dye sensitized solar cells. Bulk heterojunction polymer solar cells are fabricated in an inert glove box (H_2O and $O_2 < 0.1$ ppm) containing spin coating unit and thermal evaporator. Various polymer films are prepared using interfacial polymerization, electrodeposition or spin coating. The process for fabrication of dye-sensitized solar cell is described. Various characterization techniques, such as, scanning electron microscopy (SEM), atomic force microscopy (AFM), Fourier transform infra-red spectroscopy (FTIR), UV-visible spectroscopy (UV-Vis), scanning Kelvin probe system (SKP), High resolution transmission microscopy (HREM), electrochemical setup and Raman spectroscopy are briefly described. The details of the solar simulator and spectral response instrument employed for the measurement of the photovoltaic parameters of fabricated solar cells are presented.

Chapter 3: Bulk-heterojunction and bilayer polymer solar cells

This chapter describes the studies pertaining to the fabrication and characterization of (i) P3HT:PCBM bulk-heterojunction solar cells, (ii) porphyrin/fullerene bilayer solar cells, (iii) porphyrin-modified ZnO-NW/P3HT hybrid solar cells.

P3HT:PCBM bulk-heterojunction solar cells fabricated with device configuration ITO/PEDOT:PSS/P3HT:PCBM/Al, showed improved photovoltaic performance when subjected to thermal annealing at various temperatures. A maximum efficiency of 3.2% was obtained on annealed at 130°C for 30 min. To investigate the structural and morphological changes occurring in the blend films during heating and cooling stages of thermal annealing, we employed an *in-situ* Raman spectroscopy equipped with an optical microscope. The full-width at half-maximum of symmetric C=C stretching mode, C=C/C-C intensity ratio and Raman shift of C=C mode of P3HT reveals, molecular disorder/order of P3HT chains during heating/cooling cycles of thermal annealing. A correlation between the morphological evolution and various photovoltaic parameters of the P3HT:PCBM solar cells has been established.

Porphyrin/polyfullerene bilayer solar cells have been fabricated using layer by layer electrodeposition of donor and acceptor layers for the first time. For this purpose, the growth of donor (i.e., porphyrin) and acceptor (polyfullerene) layers was individually studied on ITO substrates. Porphyrin thin films were deposited on ITO substrates by cycling the potential from 0 to 1 V in a three electrode electrochemical cell, containing 1:1 v/v ratio of 0.1M THPP and 0.1M TBAP in methanol. The growth of these films with varied number of CV scans was studied by UV-Vis spectroscopy, SEM and other techniques. Polyfullerene films were deposited, initially by reducing C_{60} solution to C_{60}^{-2}, and later linearly sweeping the potential from -1V to 0V in a three electrode electrochemical cell, containing 1:1 v/v ratio of C_{60}^{-2} and 0.1M TBAP in dichloromethane. The thickness and morphology of these films varied with number of linear scans, which was confirmed by increased UV-Vis absorbance and SEM. The bilayer solar cells fabricated with device configuration

ITO/PEDOT:PSS/porphyrin/fullerene/Al, showed modest photoactivity yielding short-circuit currents of 0.02-0.08 mA/cm^2, open-circuit voltages of 100-300 mV, and power conversion efficiency of 0.004 - 0.01%.

Hybrid solar cells based on ZnO-NW/P3HT and porphyrin-modified ZnO-NW/P3HT configurations were fabricated and the results obtained are discussed.

Chapter 4: Dye-sensitized solar cells:

Dye-sensitized solar cells (DSSC) typically comprise a photoanode (dye adsorbed on mesoporous TiO_2 electrode), a redox electrolyte (usually I_3^-/I^- redox couple), and a platinized counter-electrode (CE). This chapter deals with several approaches which have been attempted to individually study and improve these components.

(i) *ZnO Photoanodes:* Vertically grown ZnO nanowires, synthesized by hydrothermal route were employed as photoanodes in DSSCs. The DSSC was fabricated using the low cost organic BODIPY dye as well as inorganic N3 dye. The efficiencies obtained were 0.7 and 0.8%, respectively. The reported efficiency for BOIPY dye is one of the highest reported till date. The low efficiency in case of N3 is attributed to the formation of Zn^{++} dye aggregates at ZnO surface in N3 based devices.

(ii) *TiO_2 photoanodes:* The co-sensitization of TiO_2 electrode with an inexpensive rhodamine 19 perchlorate (RhCl) laser dye along with N3 dye not only enhanced the incident-photon-to-current conversion efficiency but also reduced dark current. The devices showed an average power efficiency of 4.7% as against 2.3% and 0.6% obtained for N3 and RhCl dye based devices, respectively. The improvement in efficiency is attributed to the enhanced dye absorption on TiO_2 electrode as well as reduced dye aggregation that resulted from the usage of two dyes on different anchoring sites of single TiO_2 electrode.

(iii) *Effect of Electrolyte:* The stability and performance studies were carried out using five different electrolytes: (a) I^-/I_3^- redox couple in acetonitrile solvent, (b) I^-/I_3^- redox couple in 3-methoxypropionitrile solvent, (c) I^-/I_3^- redox couple in D.I. water, (d) Fe^{+3}/Fe^{+2} redox couple in D.I. water, and (e) gel polymer electrolyte (GPE) with polyethylene oxide as a polymer matrix. Typical issues of electrolytes such as evaporation and leakage were minimized by incorporation of gel polymer electrolyte. The power conversion efficiencies retain to 60% of the initial values after 72 hours in case of GPE, while cells with other electrolyte show poor stability.

(iv) *Conducting polymer counter electrode:* Studies were carried out to replace expensive Pt/FTO counter electrodes with free-standing polypyrrole counter electrodes, which are synthesized by liquid-liquid interfacial polymerization in a beaker containing (1:1 v/v ratio of 0.1M pyrrole in dichloromethane and 0.1M $FeCl_3$ in water. The films thus formed have a unique morphology of porous top (useful for high interfacial catalytic area) and dense base (useful for charge transport and mechanical strength). The films exhibit good catalytic activity towards I^-/I_3^- redox couple which are studied by cyclic voltammetry and electrochemical impedance spectroscopy measurements. These films were successfully employed as counter electrodes for the very first time in DSSCs yielding power conversion efficiency of 3.5% under AM 1.5, 100 mW/cm^2 illumination. These results demonstrate that free-standing polypyrrole films are potential candidate as substrate-free and Pt-free counter electrodes for low cost DSSC fabrication.

Chapter 5: Summary and Conclusions

The summary of the thesis work and main conclusions are presented in this chapter. The chapter concludes with the future scope of the research, related to the thesis work.

LIST OF FIGURES

LIST OF TABLES

Chapter -1

Introduction

1.1 Introduction to solar cells

The current world energy requirement is estimated to be ~13 terawatts (TW), which is expected to increase up to 25 TW by 2050[1]. So far the fossil fuels have been the major sources of energy. However, the reserves of fossil fuels are depleting. In addition, excessive use of fossil fuels have led to enhanced CO_2 level in the atmosphere that is responsible for the global warming. These issues have made researchers to exploit alternative sources of energy that are environmental friendly. Renewable energy (wind, solar, hydro, bio, etc.) which neither run out nor have any significant harmful effects on the environment has been one of the frontier alternative energy sources. Among various renewable energy sources, solar power has several advantages over other renewable resources. For example, wind, geothermal and hydroelectric power systems are limited to specific geographic regions and have limited potential, whereas solar power can be collected at almost any location on the earth surface and can easily meet world energy requirement.

1.1.1 Solar energy spectrum

Sunlight is an abundant energy resource freely available to everyone as the amount of solar energy reaching the surface of the earth is 1.7×10^5 TW and a practical terrestrial global solar potential value is estimated to be about 600 TW. The spectrum of the solar light that reaches the earth is influenced by absorption of radiation in the earth's atmosphere and therefore by the path length of the photons through the atmosphere. Fig. 1.1 shows the spectrum of solar radiation, which is close to that of a black body at temperature of about 5800K. The AM0 spectrum corresponds to solar irradiance just outside atmosphere (1353 W/m^2), whereas AM1.5G spectrum corresponds to an angle between the incident solar radiation and the zenith point of the measurements of 42° (1000 W/m^2)[2]. The decrease in irradiance from 1353 W/m^2 to 1000 W/m^2 (or the dips in AM 1.5G spectrum) arise from atmospheric absorption by H_2O, O_3, and CO_2 gases (as shown in Fig. 1.1). Harvesting the energy directly from the sunlight using even low efficiency photovoltaic (PV) technology could supply the demand for huge energy consumptions.

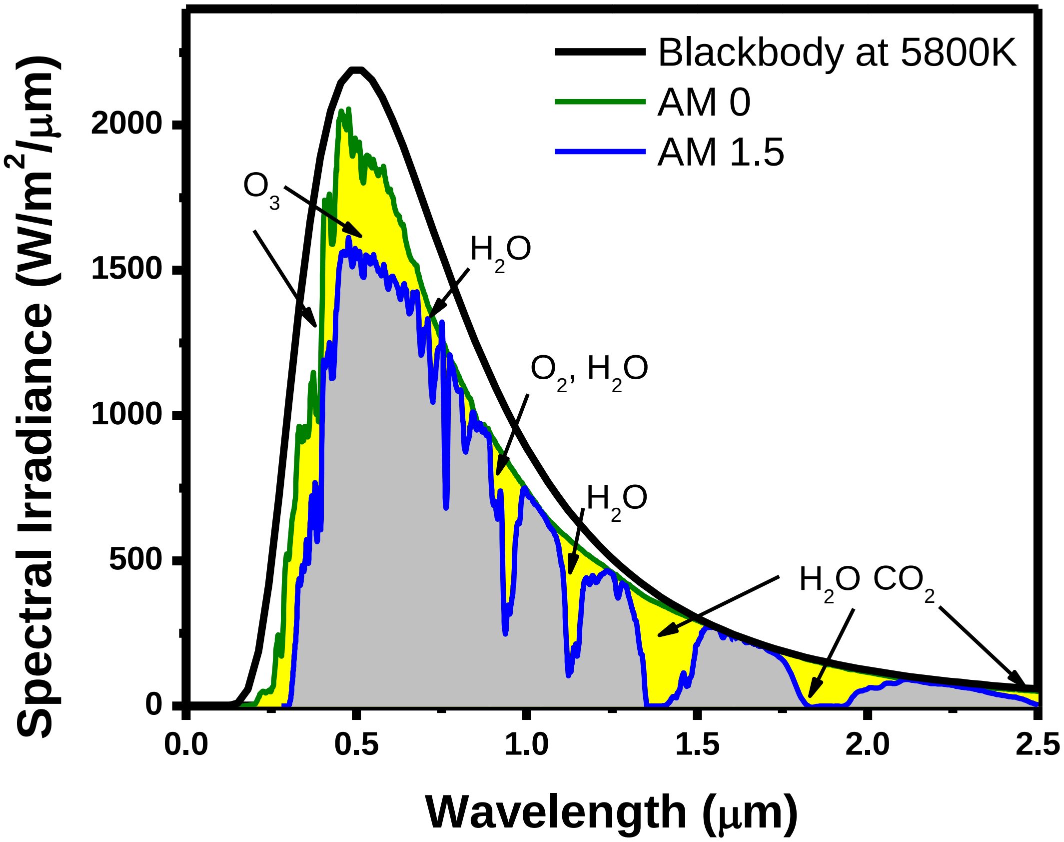

Figure 1.1: Solar irradiance at Sun, AM 0, and AM1.5G illumination.

1.1.2 Basics of solar cells

Solar cells are semiconductor devices that convert sunlight into direct current electricity. Si-solar cells typically comprise of a thin wafer consisting of an ultra-thin layer of phosphorus-doped (n-type) silicon on top of a thicker layer of boron-doped (p-type) silicon. An electrical field is created near the top surface of the cell where these two materials are in contact, called the p-n junction. The p side contains holes as majority charge carriers, while n side contains electrons as majority charge carriers. In the region near the junction an electric field is formed. The electrons and holes, which are generated through light absorption in the bulk of Si, diffuse to this junction, where they are directed by the electric field towards the respective electrodes (as shown in Fig. 1.2). The amount of current or power generated from a solar cell along with some other characteristics are presented in next sections.

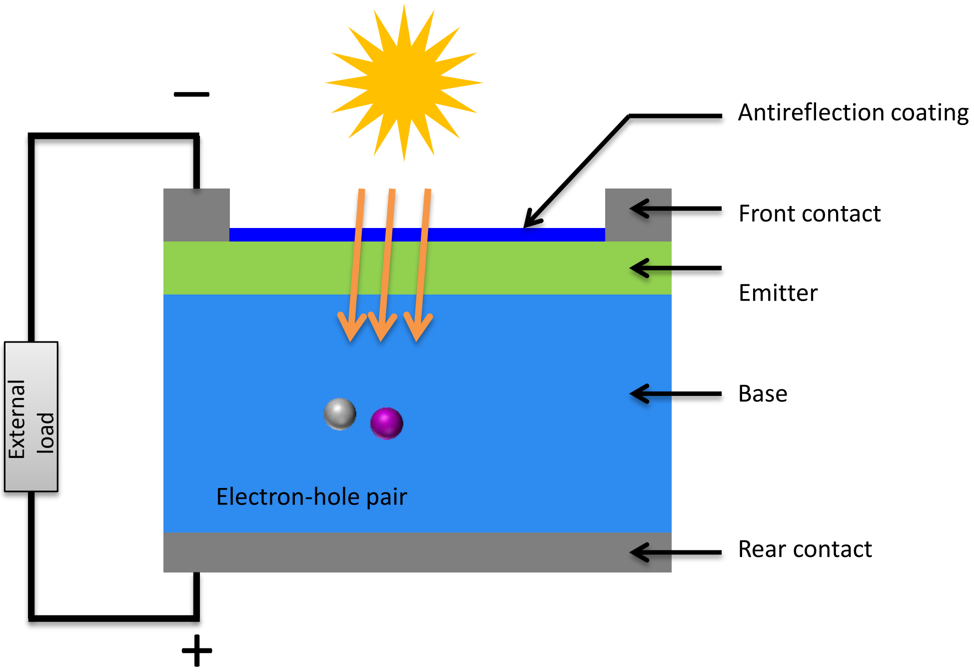

Figure 1.2: A schematic depiction of *p-n* junction Si solar cell.

1.1.3 Characteristics of solar cells

The most basic parameters of solar cells are the power conversion efficiency (PCE) usually measured under simulated AM1.5 G (1 Sun) standard conditions, and the spectral dependent external quantum efficiency (EQE), which is also called as incident photon to current collected efficiency (IPCE).

(a) I-V Characterization

The current density-voltage measurements of solar cells are usually performed under 1 sun AM 1.5G illumination of intensity 100 mW/cm^2. A typical I-V curve is shown in Fig. 1.3, from which following parameters are determined.

Short-circuit current (I_{sc}): The short-circuit current is the cell photocurrent measured at zero voltage. In general, it is presented in the form of the short circuit current density (J_{sc}) defined as the ratio of the short circuit photocurrent to the active cell area.

Open-circuit voltage (V_{oc}): The open-circuit voltage (V_{oc}) is the cell voltage measured when current within the cell is equal to zero. Maximum open circuit voltage is limited to difference in Fermi levels on p and n sides and may only be obtained at very high incident radiation intensity.

Fill Factor (FF): The fill factor (*FF*) is defined as the ratio of the maximum power output (P_{max}) to the product of short circuit photocurrent and open circuit voltage, which is defined as:

$$FF = \frac{P_{max}}{I_{sc}V_{oc}} = \frac{I_{max}V_{max}}{I_{sc}V_{oc}} \tag{1.1}$$

where I_{max} and V_{max} represent the current and voltage corresponding to the maximal power point, respectively.

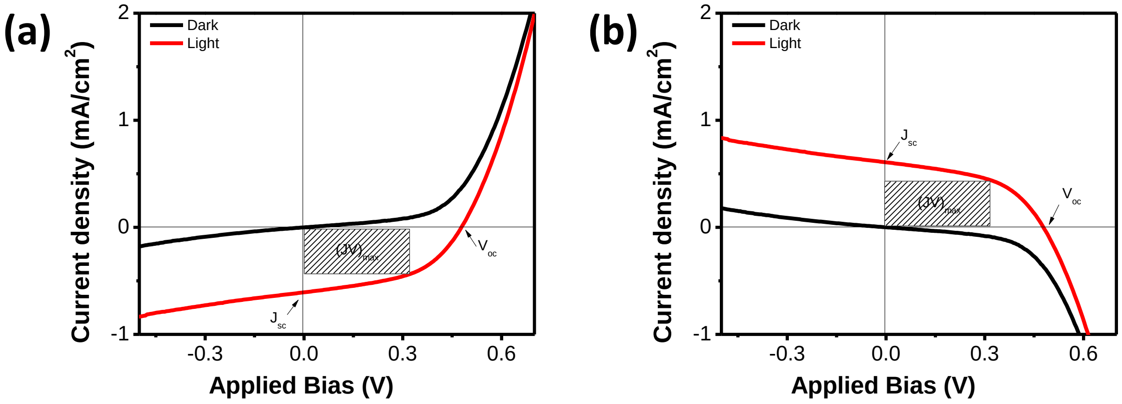

Figure 1.3: (a) Typical *J-V* characteristics of solar cells under dark and 1Sun illumination, (b) Another way of representing the *J-V* data, which is obtained after changing the sign of the photocurrent. This usually done as power generated by the device is positive.

Power conversion efficiency: The energy conversion efficiency is defined as the ratio of P_{max} to the incident radiation power (P_{in}) illuminated on the solar cell surface.

$$\eta = \frac{P_{max}}{P_{in}} = \frac{J_{sc}\,.\,V_{oc}\,.FF}{P_{in}} \tag{1.2}$$

As η is a function of I_{sc}, V_{oc} and *FF*, improvement of the solar cell performance is achieved by optimization of all the three parameters. η is also dependent on the incident irradiation power P_{in}, a white light intensity of 5, 20 mW/cm^2 was used in some of solar cell measurements.

(b) *Incident photon to current conversion efficiency*

The IPCE is measured by illuminating the solar cell with monochromatic light with the power P_{in} and recording the short circuit current I_{sc} at different wavelengths λ. Thus, the IPCE can be calculated as follows:

$$IPCE\ (\%) = \frac{number\ of\ collected\ electrons}{number\ of\ incident\ photons} * 100 = \frac{1240\frac{nm}{eV} * J_{sc}}{\lambda\ (nm) * P_{in}} * 100$$

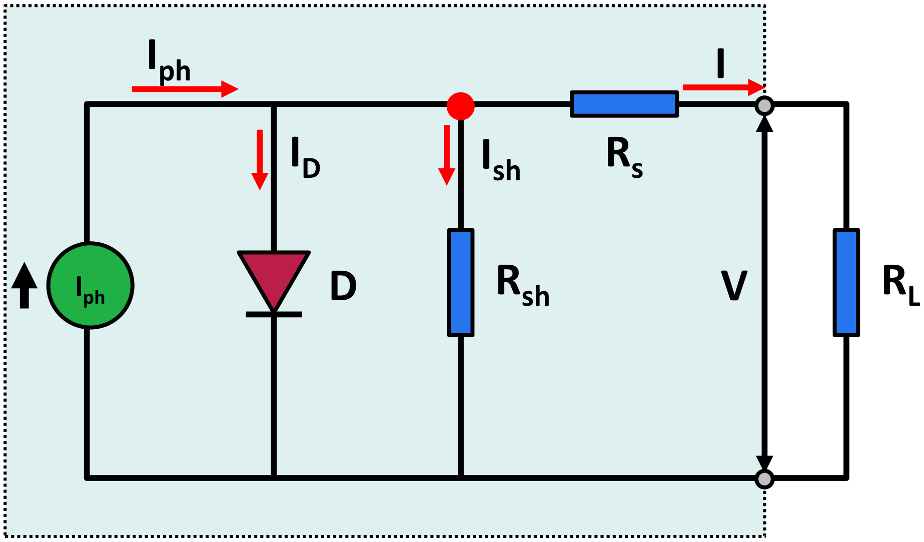

Figure 1.4: Equivalent circuit diagram of a solar cell. The blue shaded region represents the inside of the solar cell.

In order to understand the current voltage characteristics of a solar cell, the equivalent circuit diagram (ECD) of a solar cell can be drawn as shown in Fig. 1.4. From this, the external current is given as

$$I = I_{ph} - I_d - I_{sh} \qquad (1.3)$$

Where diode current (I_d) and shunt current (I_{sh}) are written respectively as

$$I_d = I_0 \left\{exp\left(q\frac{V+IR_s}{nkT}\right) - 1\right\} \qquad (1.4)$$

$$I_{sh} = \frac{V+IR_s}{R_{sh}} \tag{1.5}$$

Therefore the circuit equation is rewritten in the form of

$$I = I_{ph} - I_0 \left\{exp\left(q\,\frac{V+IR_s}{nkT}\right) - 1\right\} - \frac{V+IR_s}{R_{sh}} \tag{1.6}$$

Where I_{ph} is photo current, I_0 is saturation current, R_s is series resistance, R_{sh} is shunt (parallel) resistance, n ideality factor, q elementary electric charge, k Boltzmann constant, T is an absolute temperature.

In this equation:

i. The first term i.e. I_{ph} (photocurrent) is generated by the device upon illumination. This current results from the generation of excitons and their subsequent dissociation into free charges. The magnitude of the current will depend on the illumination intensity but it is assumed to be independent of the voltage in this model.

ii. The second term is the current due to recombination, which depends upon dark current (I_0), series resistance (R_s), and the ideality factor (n). Ideally the R_s should be as low as possible. The n describes how closely the J-V curve follows the theoretical model, and provides information on the recombination processes. The value of n=1 implies solar cell is close to an ideal diode. The values of n>1, indicates recombination from the localized states (traps) [3].

iii. The third term represents the shunt currents, which is governed by shunt resistance (R_{sh}), and represents losses due to any leakage in the device. Ideally the value of R_{sh} should be infinity.

With the help of the equivalent circuit diagram and the Eq.1.6, measured *J-V* curves can be fitted to obtain characteristic parameters of the components. Even though this simplified model may not fully represent the physical reality, it helps to detect problems in the device limiting the device efficiency, from which improvements of the device structure can be deduced.

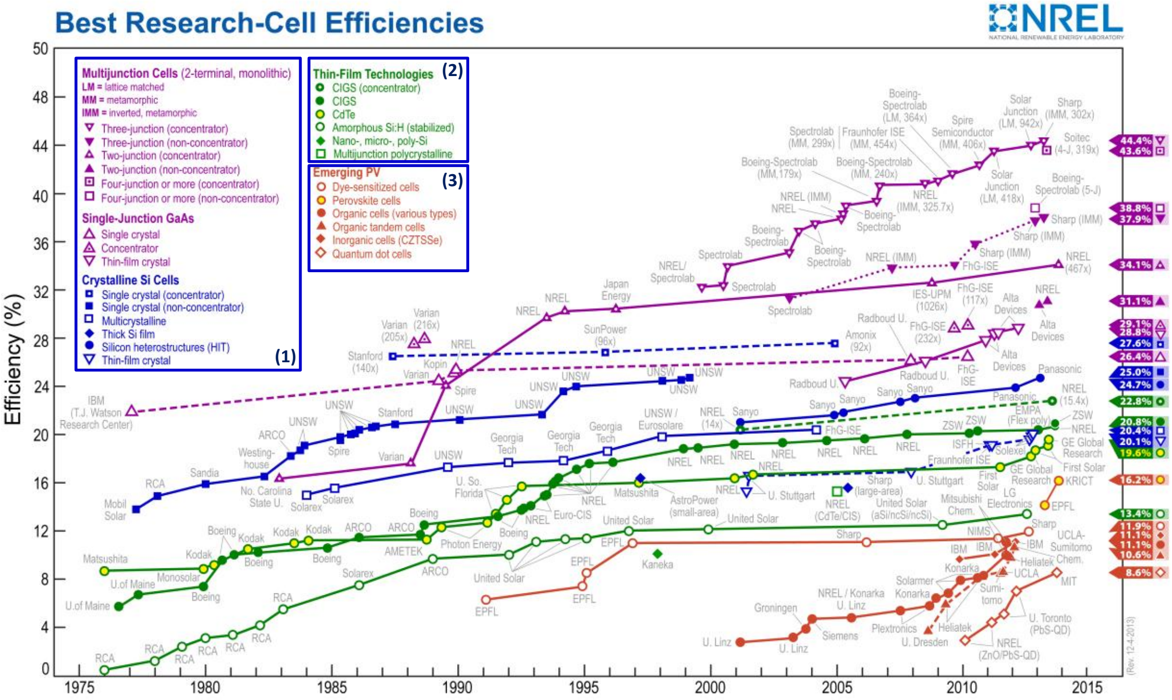

Figure 1.5: Efficiency improvement of various solar cell technologies.

1.2 Evolution of solar cell technology

The evolution of various solar cell technologies along with their efficiencies are summarized in Fig 1.5 (taken from NREL solar cell efficiency charts). It is clearly evident from this figure, many different solar technologies have emerged over a period of time, which can be broadly classified into three generations: (1) First generation solar cells based on single crystal Si, GaAs, and multi-junctions; (2) Second generation solar cells based on thin films of chalcogenides and amorphous Si; and (3) Third generation solar cells based on organic semiconductors, inorganic quantum dots and hybrid materials.

1.2.1 First generation solar cells

The first crystalline silicon solar cell having an efficiency of 6% was developed at Bell Laboratories during 1950s, and today its efficiency has reached upto 24% [4, 5] . These crystalline Si solar cells currently account for more than 85% of the commercial market. Along with crystalline Si solar cells, technologies based on single-junction GaAs (current efficiency ~34.1%) and multi-junctions (current efficiency ~43%) are developed. Despite of such high efficiencies of these single and multi-junction solar cells, they could not find commercial market owing to high-cost and limitation in large-scale production.

1.2.2 Second generation solar cells

The second generation solar cells are based on thin film technology, where the material cost is believed to be reduced due to less quantity of the material used. In addition, thin film solar cell materials can be deposited onto large surfaces, which is beneficial for volume production (i.e. high throughput). The materials used in thin film solar cells include, amorphous silicon (a-Si), cadmium telluride (CdTe), copper indium gallium diselenide (CIGS) etc.[6-8]. Most of these materials have much higher absorption coefficient than silicon, and therefore, needed effective thickness of the film is < 1µm thick, which is ~300 times less than in single crystal Si solar cells.

Among various thin film solar cell technologies, the CIGS solar cells have reached an efficiency of ~20%. A typical device structure of CIGS solar cells with typical individual layer thicknesses is shown in Fig. 1.6. Soda lime glass or flexible substrates (polyimide or metal foils) coated with molybdenum layer (as back contact and for reflection of unabsorbed light back into the device) are used as substrates. A p-type CIGS absorber layer is then deposited followed by deposition of thin n-type buffer layer (typically CdS). The buffer is overlaid with a thin, intrinsic ZnO layer (i-ZnO) which is capped by a thicker, Al doped ZnO layer (serves as a transparent conducting oxide to collect and move electrons out of the cell while absorbing as little light as possible). The efficiencies of a-Si and CdTe solar cells have reached to 13 and 19.6%, respectively. The major problem with a-Si has been the degradation of efficiency with time. CdTe thin films solar cells may not be suitable for deployment at large scale due to the presence of poisonous cadmium content of the cells.

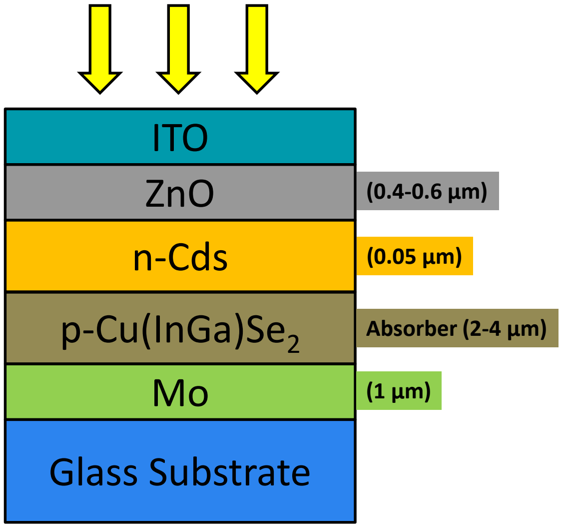

Figure 1.6: Schematic view of the typical substrate structure of CIGS solar cells (with typical film thickness).

1.2.3 Third generation solar cells

Though the first generation solar cells have demonstrated high efficiencies, they lack large area production and do not have possibility of using flexible surfaces. The second generation solar cells have overcome the limitation of the flexibility of first generation as well as large area production to certain extent. However, their efficiencies are moderately low and the employment of hazardous cadmium material has a bearing on environment. Therefore, the third generation solar cells have emerged which are largely based on organic materials, inorganic nanocrystals and hybrids (shown in Fig. 1.5, Inset box with no. 3).

Briefly, organic solar cells are typically fabricated by employment of organic semiconductors as absorber materials. Small molecule solar cells (introduced by C.W. Tang *et.al.*[9]) have shown efficiencies upto 12% (Heliatek), whereas polymer solar cells (introduced by Heeger *et.al.)* have reached efficiencies upto 10% (Toray). These solar cells with tandem structure comprising two or more sub cells (with complementary absorption) show improved efficiencies with their individual counterparts either resulting in increase of currents (connected in parallel) or voltages (connected in series). Dye-sensitized solar cells introduced by Grätzel and O'Regan in 1991[10] have emerged as low-cost solar cells, which have already demonstrated a potential market for portable electronics and Bi-PV. Gratzel's group holds current world record efficiency of 12.6% with novel porphyrin based dyes and cobalt redox electrolytes [11]. The molecular engineering of dyes, novel catalyst materials and new electrolytes (quasi solid electrolytes) made this technology very near towards commercialization. Quantum dot solar cells employing semiconductor nanocrystals with tunable bandgaps (by changing the quantum dot size) have attained efficiencies of ~10%. Perovskite solar cells, with organic-inorganic perovskites as absorber materials have shown efficiencies upto 15 % [12]. Among the several emerging solar cells, polymer solar cells and dye-sensitized solar cells are of interest for thesis work and are discussed in detail in further sections.

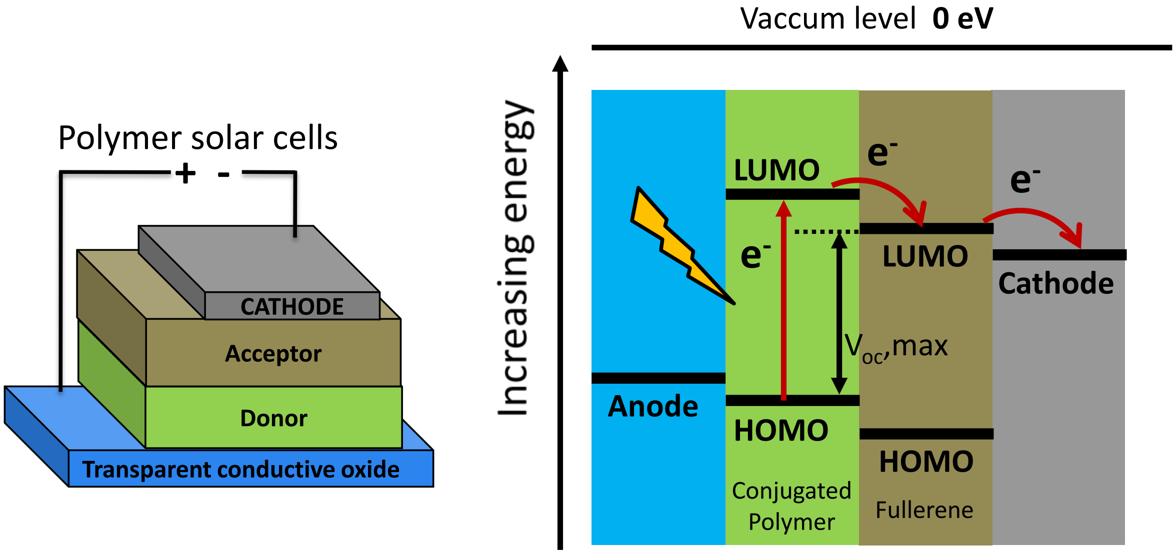

Figure 1.7: Schematic depiction of polymer solar cells with corresponding energy diagram

1.3 Polymer solar cells

Device structure: A polymer solar cell is a solar cell made by sandwiching the photon absorber layer (typically called as photoactive layer) between two different electrodes (as shown in Fig. 1.7). The active layer consists of either a “mixture of conducting polymer (electron donor) and fullerene molecules (electron acceptor)” or “stacked layers of conducting polymer and fullerene”, a corresponding energy diagram is described in Fig.1.7. A 100-150nm thickness of active layer is sufficient to harvest all the incident light illuminated on solar cells. However, charge carriers generated in the active layer are bound to form an electron-hole pair (termed as exciton), whereas in Si solar cells which leads to formation of free electrons and holes. The detailed working principle of these polymer solar cells are described as follows.

1.3.1 Working principles

Working mechanism: In a typical polymer solar cell operation, there are the four fundamental physical processes, which are described by schematic depiction (Fig. 1.8) and energetics of materials (Fig. 1.9)[13]:

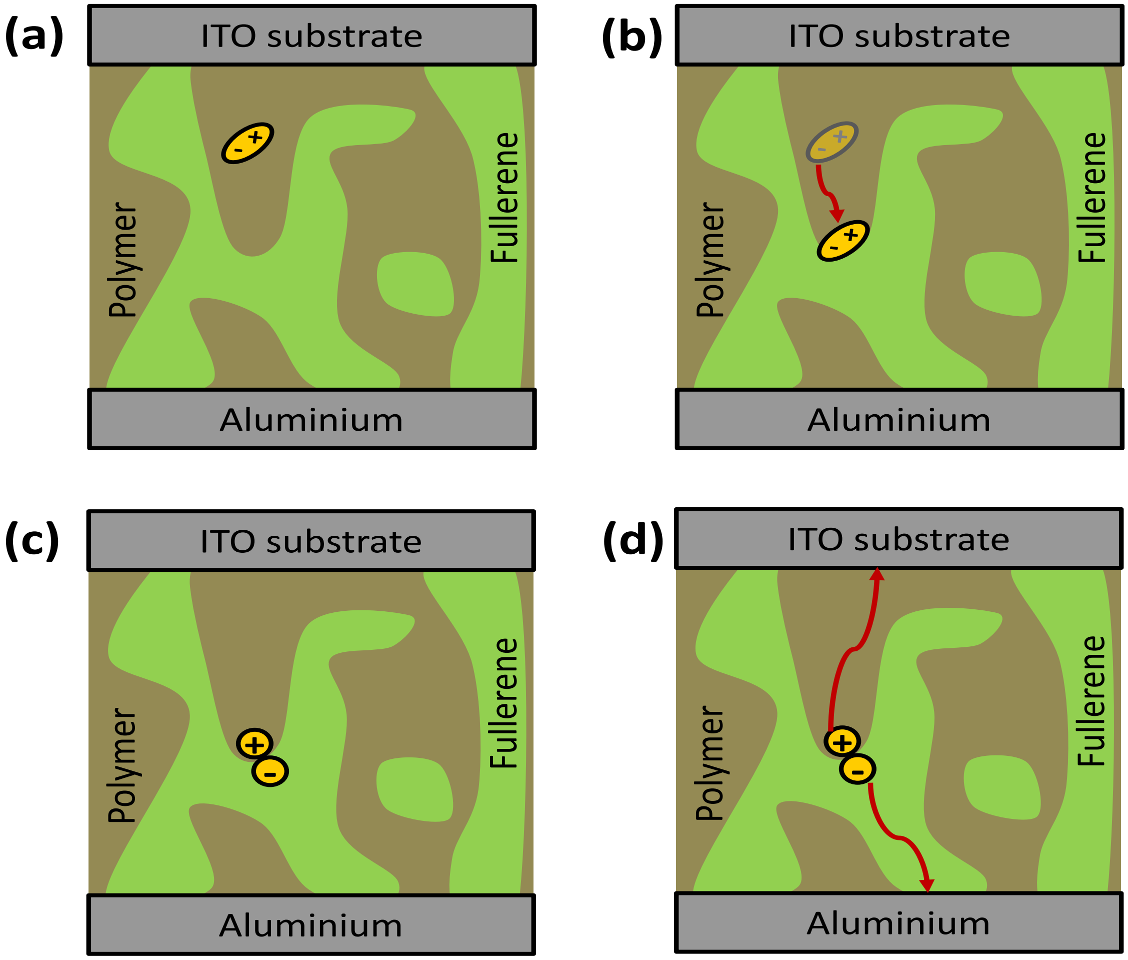

Figure 1.8: (a-d) Schematic depiction of various processes during the operation of polymer solar cells under 1Sun illumination

Step 1: Light absorption

When light is absorbed in the donor material (usually a conjugated polymer), strongly bound electron-hole pairs (so called excitons) are created (Fig. 1.8a, Fig. 1.9a).

Step 2: Exciton diffusion

The photogenerated excitons are strongly coulomb bound due to the low dielectric constant in organic materials, and the correspondingly low screening length. Thus, electrically neutral excitons can only move by diffusion in order to dissociate into an electron-hole pair at interface of donor-acceptor molecules (as shown in Fig. 1.8b & Fig.1.9b).

Step 3: Exciton dissociation

The excitons dissociate only at energetically favorable donor acceptor interfaces when the energy gain is larger than the exciton binding energy. An electron transfer (or charge transfer) takes place, dissociating the exciton into an electron on the fullerene acceptor, and a hole remaining on the polymer (shown in Fig. 1.8c and Fig. 1.9c). After dissociation, this electron-hole pair is still coulombically bounded, which is called geminate pair or polaron pair.

Step 4: Charge transport

The polaron pair are dissociated into free electron and hole with built-in electric field provided by two different electrodes. Finally the electrons and holes are transported to the respective electrodes, driven by the electric field. The carriers in respective phases are moved by a hopping transport process, which is a very slow charge transport with low carrier mobility (at least a factor of 1000 smaller) compared to crystalline silicon.

However, there are several loss mechanisms involved during the operation of solar cells (shown in Fig 1.9 e,f). Briefly, the loss mechanisms are an exciton decay, geminate recombination of bound electron-hole pairs, and bimolecular recombination of free charge carriers.

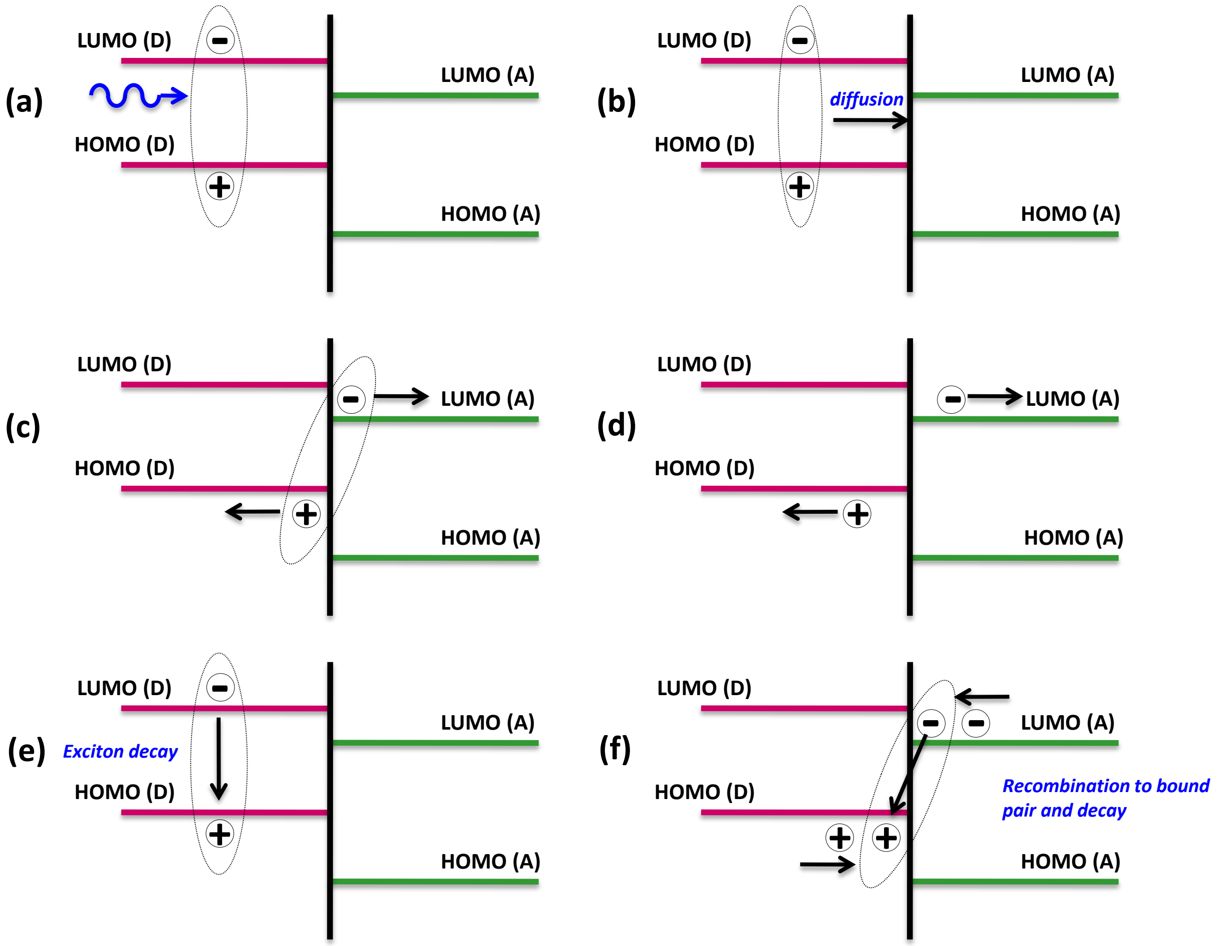

Figure 1.9: (a-f) various process involved in polymer solar cells.

1.3.2 Literature survey and issues

The concept of *organic solar cells* originates from conventional p-n junction silicon solar cells, where the former employ organic semiconductors and later inorganic semiconductors as the active materials. As schematically depicted in Fig. 1.10, light absorption in “Inorganic semiconductors” leads to free charge carriers owing to their perfectly ordered atomic structures, whereas in “Organic semiconductors” light absorption leads to formation of “*Excitons”* (coulombically bound electron-hole pair) due to high exciton binding energy in organic materials. Typically, Frenkel Excitons having binding energy ~ 0.1 - 0.4 eV, binding radius ~ 10 Å are observed in organic semiconductors. These localized neutral excitons which are bound to specific atoms or molecules move by hopping from one atom to another. Organic semiconductors can be widely classified into two groups on the basis of their molecular weight, conjugated polycyclic compounds of molecular weight less than 1000, and heterocyclic polymers with molecular weight greater than 1000. Solar cells fabricated with small molecules as active materials are termed as “Small molecule solar cells”, whereas solar cells employing high molecular weight conducting polymers as active materials are called as “Polymer solar cells”. Among this, polymer solar cells have attracted a great interest in research and industrial community due to their potential advantages over conventional Si solar cells, such as, low cost, light weight, flexibility, ease of fabrication, high throughput etc.[14-18].

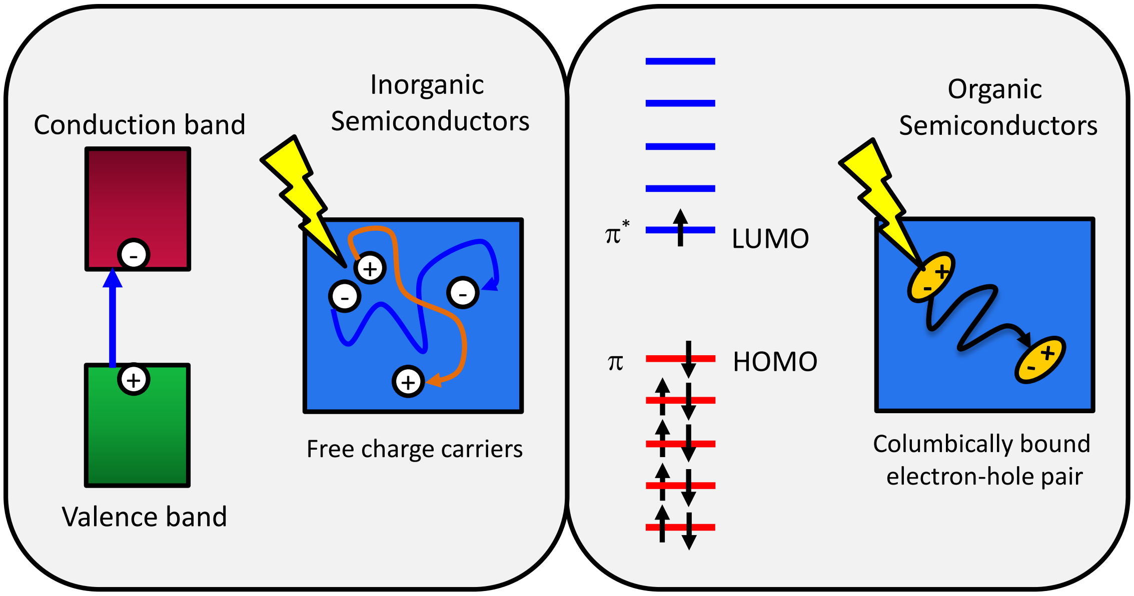

Figure 1.10: Schematic depiction of carrier transport in inorganic and organic semiconductors

The field of *polymer solar cells* (often called as polymer-fullerene solar cells) has taken a huge splurge with the discovery of conducting polymers [14]. Conducting polymers are highly conjugated polymers, having backbones of continuous sp^2 hybridized carbon centers which have a large overlap between p_z orbitals providing large delocalized states. As described in above section, polymer solar cells employ conducting polymers as electron donor materials and fullerenes as electron acceptor materials. Since its inception, the power conversion efficiency of polymer solar cells has improved rapidly from below 1% to over 9 %. This impressive achievement is mainly achieved by molecular engineering (synthesis) of novel low-bandgap polymers, introduction of various transport layers (hole & electron transport), tuning of active layer morphologies, employment of various device structures etc.[19]. In this regard, various conducting polymers were evolved, (i) firstly, poly(phenylene vinylene)s (PPV), poly(2-methoxy-5-(2′-ethylhexyloxy)- 1,4-

phenylenevinylene) (MEH-PPV) and poly(2-methoxy-5-(3′,7′- dimethyloctyloxy)-1,4-phenylenevinylene) (MDMO-PPV) were introduced. Power conversion efficiencies upto 3% were achieved by employing PPV based polymers as donors and Phenyl-C_{61}-butyric acid methyl ester ($PC_{61}BM$) as acceptors materials [20, 21]. (ii) Secondly, smaller-band-gap polymers (thiophenes) were investigated. Regioregular poly(3-hexylthiophene) (rr-P3HT) with PCBM as acceptor material demonstrated PCE upto 5% [22, 23]. (iii) Lately, polycarbazole based polymers and some patented absorber materials have demonstrated world record efficiencies over 9%. Although, many investigations were made during this period, no suitable materials were found to replace highly efficient fullerene derivatives ($PC_{61}BM$, $PC_{71}BM$, ICMA, ICBA) as acceptor materials in polymer solar cells. Some of the photovoltaic properties with various conducting polymers are presented from the literature in Table 1.1.

Table 1.1: Photovoltaic parameters of BHJ with different conducting polymers.

Polymer	Optical Bandgap (eV)	Acceptor	J_{sc} (mA/cm^2)	V_{oc} (V)	*FF*	η (%)	Ref.
MDMO-PPV	2.3	[60]PCBM	5.25	0.82	0.61	2.5	[20]
P3HT	1.9	[60]PCBM	12	0.57	0.67	4.6	[24]
PFDTBT	1.9	[60]PCBM	4.66	1.04	0.46	2.2	[25]
PCDTBT	1.9	[70]PCBM	10.6	0.88	0.66	6.1	[26]
PCPDTBT	1.4	[70]PCBM	16.2	0.62	0.55	5.5	[27]
C-PCPDTBT	1.3	[70]PCBM	15.5	0.37	0.48	2.7	[28]
PBnDT-DTffBT	1.7	[60]PCBM	12.91	0.91	0.61	7.2	[29]

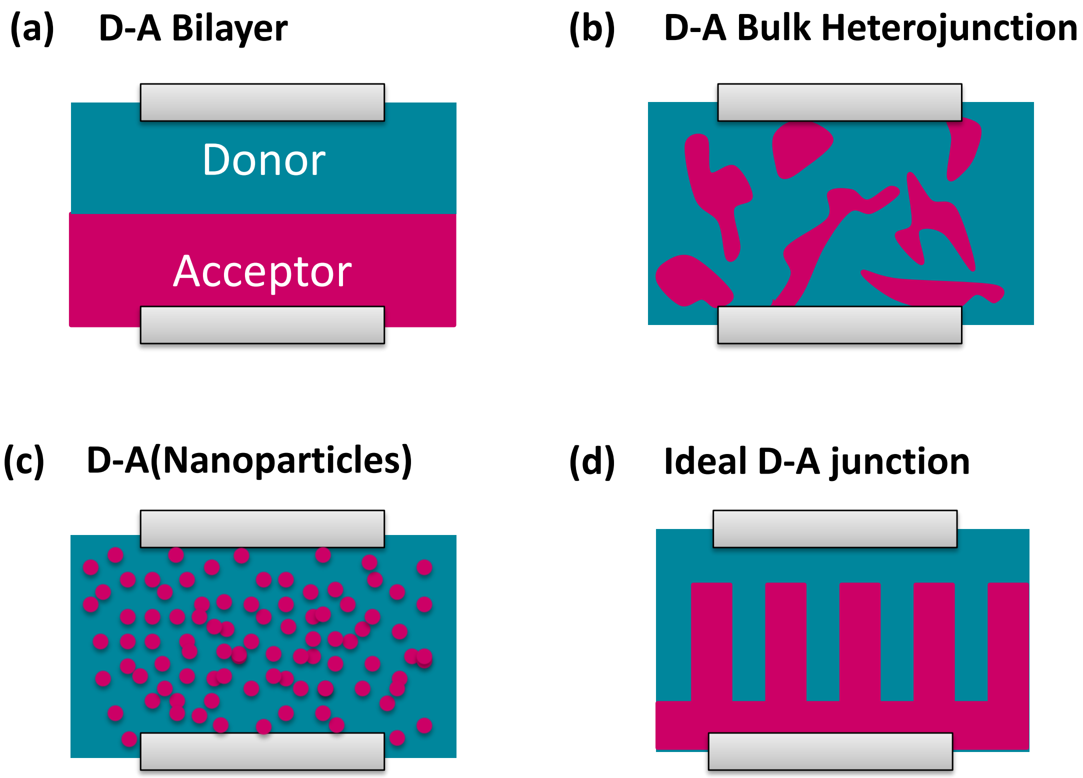

Figure 1.11: (a-d) various device architectures employed in the fabrication of polymer solar cells

In the initial stages of research, the polymer solar cells were fabricated by sandwiching a thin film of conducting polymer (called homojunctions) between two different metal electrodes [19]. Since, the excitons generated in this homojunctions are so strongly bound, the field in a photovoltaic device, which arises from the work function difference between the electrodes, is much too weak to dissociate the excitons. Later, Tang *et. al.* [9] used two different materials (called donor and acceptor materials), which are stacked in layers, to efficiently dissociate the photogenerated excitons. This donor and acceptor materials are selected by carefully matching their energy levels, to prompt electron transfer from the donor to the acceptor (or hole transfer from the acceptor to the donor)[19]. Since then, the various device structures evolved (as shown in Fig 1.11) in polymer solar cells are presented as follows.

(a) *Bilayer solar cells:* In bilayer heterojunction solar cells, donor and acceptor layers are sequentially stacked on top of each other (Fig. 1.11 a) [30, 31]. In this devices, only excitons created within the distance of 10-20 nm (known as exciton diffusion length) from the interface can reach the heterojunction interface. Hence, the thickness of the individual films chosen typically ~20-30 nm. The thin films doesn't absorb all the incident radiation, while the thicker films results in recombination of charge carriers generated away from the donor-acceptor interface. Thus the efficiency of bilayer solar cells are mostly limited by the thickness of the active materials.

(b) *Bulk-heterojunction solar cells:* The concept of bulk-heterojunction (BHJ) solar cells was introduced to overcome the limitations presented in the bilayer solar cells. In this solar cells, an active layer comprising a blend of both donor and acceptor materials, is sandwiched between two electrodes [32-34]. Unlike in bilayer solar cells, the interface is not planar but spatially distributed over the entire volume of the active layer. This results in a formation of three dimensional interpenetrating network with increased interfacial area between phase-separated donor and acceptor materials. As listed in Table 1.1., among the many conducting polymers employed in polymer solar cells, till date, the most successful BHJ polymer solar cells are based on P3HT and PCBM materials[35]. The efficiencies of this system is dependent mainly on film morphologies to provide high interfacial area between P3HT and PCBM phases and charge transport properties[13]. However, achieving such morphology is difficult in reality as the structure and morphology depends upon interplay between various complex thermodynamic and kinetic factors [36]. Experimentally, the efficiencies of bulk heterojunction P3HT:PCBM based solar cells have been reported in the range of 2–5%[1], whereas the theoretically predicted value is as high as 8% [37, 38]. Thus there is a great experimental interest in the investigation of the structural and morphological evolution of P3HT:PCBM films so that the solar cells fabricated using them has high efficiencies. In order to control the structure and morphology of P3HT:PCBM films different approaches such as thermal annealing [39, 40], solvent annealing [41], electrical field annealing [42] and nano-patterning [43] have been employed. Among these, thermal annealing is widely employed owing to its simplicity and effectiveness in controlling the morphology via de-mixing of PCBM and stacking of P3HT in coplanar conjugated segments. Experimental results show that the highest efficiency is obtained when the active layer is annealed at a temperature in the range of 120-150°C [13, 44]. As of now it is not fully understood that how annealing processes affects the ordering of molecules, morphology and domain size of each component in the P3HT:PCBM films.

(c) *Hybrid solar cells:* To increase the interfacial area further between donor and acceptor phases, inorganic semiconductor nanoparticles were introduced as acceptor materials forming hybrid solar cells (Fig. 1.11 c). Although, efficiencies upto 5% were achieved, this technology still has poor control of morphologies with increased aggregates of nanoparticles[45].

(d) *Ideal solar cells:* Ideal solar cells are derived from ordered BHJ concept, where photogenerated excitons are within the exciton diffusion length of each phases. Also, this structure provide donor-acceptor phases a continuous straight pathways to the respective electrodes, to reduce carrier recombination and increase charge collection efficiency. Efforts were made to fabricate this ideal device structure by nano-patterning of conducting polymers [43]. Although, the efficiency of this solar cells are low, the ideal device architecture is among the most promising approach to obtain high efficiency in polymer solar cells.

(e) *Novel device architecture:* As ideal device structures with individual widths within exciton diffusion lengths are difficult to make, a new device architecture which are conceptually in between the bilayer and bulk-heterojunction configurations, so called “diffuse bilayer solar cells” are introduced. This device structure has the advantages of both device configurations, i.e., an increased donor-acceptor interface and spatially uninterrupted pathway for the opposite charge carriers to their respective electrodes. This device configuration has been achieved earlier in several ways. (i) Laminating two polymer thin films by applying moderate pressure and temperatures[46]. (ii) Spin-coating the second layer from a solvent that partially dissolves the underlying polymer layer[47, 48]. (iii) Annealing a bilayer device just over its melting point to cause inter-diffusion between donor and acceptor phases yielding intermixed interfacial regions [49]. All the above approaches have resulted in diffuse interface which improves their performance.

Briefly, from the above literature survey, the specific issues which limit the performance of polymer solar cells are as follows:

(1) Charge dissociation, extraction and collection.

(2) Low interfacial area between donor and acceptor phases etc.

(3) Low efficiencies and limited device architectures

All these issues play a vital role in determining the performances of polymer solar cells, and therefore, their roles need to be investigated in detail.

1.4 Dye-sensitized Solar Cells (DSSCs)

Dye-sensitized solar cells, also known as Grätzel cells, were invented by Grätzel and O’Regan at École Polytechnique Fédérale de Lausanne (EPFL) in 1991 [10]. The concept/mechanism for dye-sensitized solar cells was originated from nature’s photosynthesis principle. In photosynthesis, plant leaves are tiny factories in which sunlight absorbed by chlorophyll converts carbon dioxide gas and water into carbohydrates (glucose) and oxygen, thus providing for the energy requirements of the plant. Dye-sensitized solar cells (artificial photosynthesis) are based on the concept of a dye analogous to chlorophyll absorbing light and thus generating electrons which enter the conduction band of a high surface area semiconductor film and further move through an external circuit, thus converting light into "green" power (a schematic of DSSC is shown in Fig. 1.12).

A typical DSSC contains a fluorine-doped tin oxide (SnO_2:F, FTO) covered glass as transparent conducting substrate, a thin wide-bandgap oxide semiconductor, such as ZnO or TiO_2 film coated on FTO, a monolayer of dye attached to the surface of TiO_2 layer by self-assembly, an electrolyte (liquid-state dye-sensitized solar cell) or hole transport material (HTM) (solid-state dye sensitized solar cell) which fully covers the TiO_2/dye surface and a counter electrode (such as platinum on glass used for electrolyte contained DSSCs, silver or gold electrode for hole transport materials contained solid-state dye-sensitized solar cells. Although DSSC have achieved excellent device performance, several limitations hinder their large scale applications.

1.4.1 Working principle

The schematic of the interior of a DSSC is shown in Fig. 1.12. Generally it comprises, the mesoporous oxide layer composed of a network of TiO_2 nanoparticles that have been sintered together to establish electronic conduction. Typically, the film thickness is say 10 μm and the nanoparticle size 10-30 nm in diameter. The mesoporous layer is deposited on FTO on a glass or plastic substrate. Attached to the surface of the nanocrystalline film is a monolayer of the charge-transfer dye (say Ruthenium polypyridyl complexes). Photoexcitation of the dye molecules results in the injection of an electron into the conduction band of the TiO_2, leaving the dye in its oxidized state. The dye is restored to its ground state by electron transfer from the electrolyte, usually an organic solvent containing the iodide/triiodide redox system. The regeneration of the sensitizer by iodide intercepts the recapture of the conduction band electron by the oxidized dye. The I_3^- ions formed by oxidation of I^- diffuse a short distance (<50 μm) through the electrolyte to the cathode, which is coated with a thin layer of platinum catalyst, where the regenerative cycle is completed by electron transfer to reduce I_3^- to I^-. The voltage generated under illumination corresponds to the difference between electrochemical potential of the electron at the two contacts, which generally for DSSC is the difference between the Fermi level of the mesoporous TiO_2 layer and the redox potential of the electrolyte.

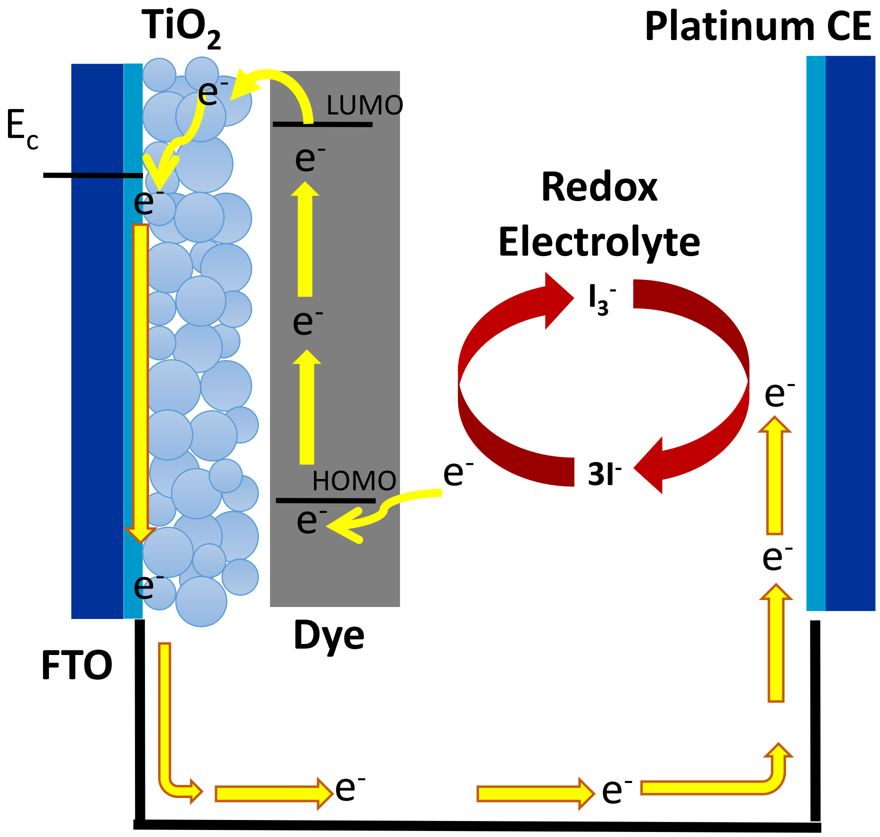

Figure 1.12: Schematic depiction of a dye-sensitized solar cell.

The basic electron transfer processes in a DSSC, comprising ruthenium based N_3 dye adsorbed on TiO_2 and I^-/I_3^- as redox couple in the electrolyte is shown in Fig. 1.13. Besides the desired pathway of the electron transfer processes (with black arrow 3, 4, 5, and 8) occurring in DSSC, the recombination processes (with red arrow 2, 6, and 7) are indicated. Reaction 2 is direct recombination of the excited dye, which is reflected by the excited state lifetime. Recombination of injected electrons in the TiO_2 with either oxidized dyes or acceptors in the electrolyte are shown in 6 and 7, respectively. In principle, electron transfer to I_3^- can occur either at the interface between the nanocrystalline oxide and the electrolyte or at areas of the anode contact (usually a fluorine-doped tin oxide layer on glass) that are exposed to the electrolyte. In practice, the second route can be suppressed by using a compact blocking layer of oxide deposited on the anode by $TiCl_4$ treatment [50, 51].

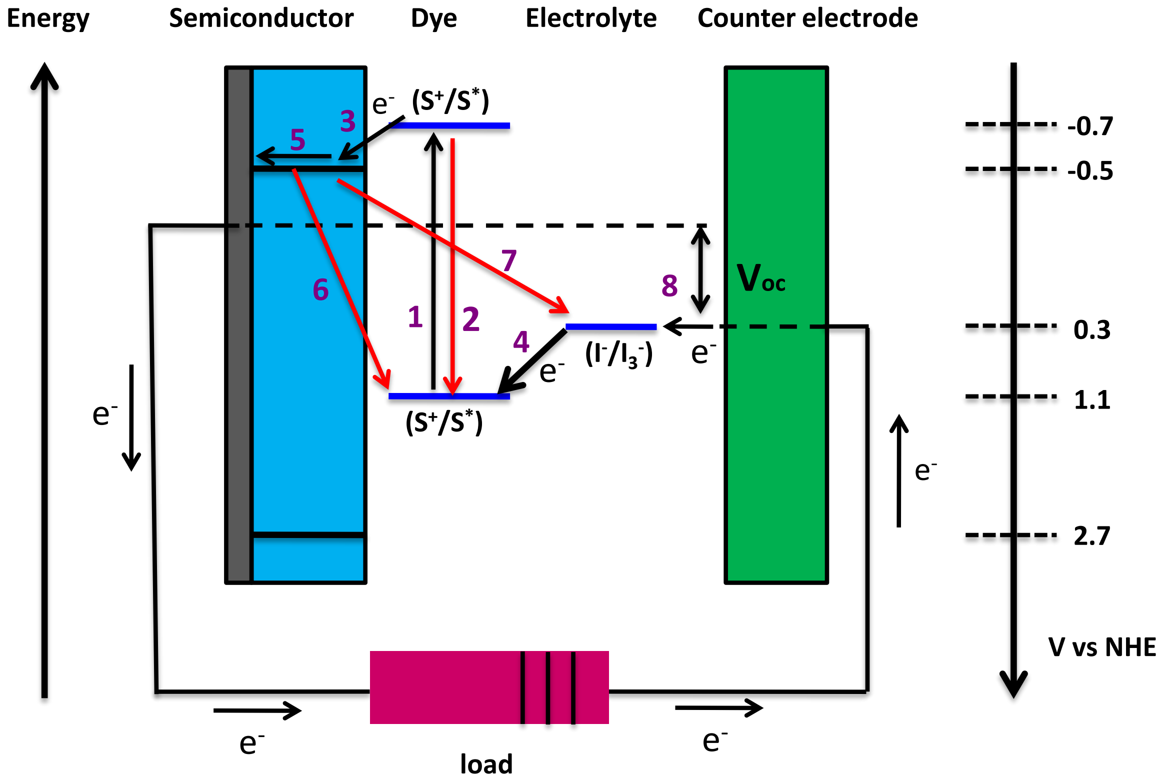

Figure 1.13: Simple energy level diagram for a DSSC. The basic electron transfer processes are indicated by numbers (1-7). The potentials for a DSSC based on the N_3 dye, TiO_2, and the I^-/I_3^- redox couple are shown.

1.4.2 Literature survey and issues

As described earlier, dye-sensitized solar cells compose many individual components that have to be optimized, both individually and then again as a whole device. The key components, affecting the performance of the DSSC are dye coated photoanodes, electrolyte, and counter electrodes. The progress made in each of these key areas with current major issues are discussed as follows.

a) ***Photoanode:*** Photoanodes typically comprise of dye molecules adsorbed on the surface of wide bandgap metal-oxide semiconductor films, which are deposited on TCO (Transparent conductive oxide) substrates. So far, ITO has been the most commonly employed substrates for photonic and optoelectronic devices. The employment of high temperature annealing conditions limits the usage of ITO as substrates for DSSC, because of poor thermal stability of ITO. Hence, fluorine-doped tin oxide (F:SnO_2, FTO) with superior performance are employed as substrates for both electrodes, which accounts to half of total cost of the solar cell. Many wide bandgap metal-oxide semiconductors (such as TiO_2, ZnO, SnO_2, etc.) have been employed as photoanodes for DSSC. Among them, TiO_2 (in its anatase form) mesoporous films and one dimensional (1D) ZnO nanostructures have turned out to be the most versatile materials delivering better efficiency.

ZnO as photoanode: ZnO had an advantage of high electron mobility as compared to that of TiO_2[52]. Unfortunately, ZnO suffers from several problems as listed below.

(i) The amount of dye loading onto ZnO is generally low, which to certain extent can be increased by prolonged sensitization.

(ii) Prolonged sensitization often leads to the formation of ZnO/dye complexes. This requires designing of new dyes which do not react with ZnO.

(iii) Formation of Zn^{2+}/dye complexes could block the injection of electrons from the dye molecules to the electrodes [53]. In addition, the interface can act as deep traps for the electron transfer resulting in enhanced dark current.

(iv) Desorption of dye into electrolyte takes place as the DSSC works for prolonged period.

<u>TiO_2 as photoanode</u>: Although TiO_2 has less electron mobility as compared to ZnO, it has been studied widely owing to its superior dye loading capacity with many organic and inorganic dyes. Although it has been widely been investigated, there are several issues pertaining to the TiO_2 photoanode that remained yet unsolved. Some of these are:

(i) The recombination of photo-electrons from TiO_2 to electrolyte is significant, which causes enhanced dark currents.

(ii) Mesoporous structures of TiO_2 yields poor connectivity of nanoparticles, which leads to low electron mobility.

(iii) Desorption of dye into electrolyte takes place as the DSSC works for prolonged period for some specific dyes.

All the above three issues leads to poor efficiency of TiO_2 photoanode based DSSC's. In order to improve the power conversion efficiency of DSSCs, following three approaches have been normally employed:

(i) Fabrication of tandem device, i.e., a DSSC made by using different dyes being connected in series [54]

(ii) Use of single panchromatic sensitizers that are capable of absorbing light from visible to IR region [55] and

(iii) Usage of mixture or cocktail of dyes on TiO_2 electrode to achieve broad absorption range [56, 57].

While tandem cells require tuning of J_{sc} and V_{oc} along with adjustment of transmittance of the top cell; usage of single panchromatic sensitizers with wide absorption spectrum causes difficulty in injection of electrons from the dye to the TiO_2 electrode. This difficulty in single panchromatic sensitizer arises because the lowest unoccupied molecular orbital (LUMO) of the dye is at the same level as the conduction band (CB) of TiO_2 whereas a minimum gap of 0.2 eV is necessary to provide the thermodynamic force for efficient electron injection from the dye to TiO_2 CB [58]. Sensitization of TiO_2 electrode by a cocktail of dyes has been adopted widely for attaining higher levels of efficiency in DSSCs. However, this introduces problems in controlling the dye sensitization process on a TiO_2 electrode, as the adsorption kinetics of different dyes on TiO_2 electrode could be widely different. In addition, it becomes difficult to inject electrons from a mixture of dyes because of occurrence of unfavorable electron transfer between the dyes themselves, which consequently lowers the cell efficiency. This issue was addressed by either using step-by-step sensitization of TiO_2 electrode with dyes under pressurized CO_2 environment [59] or by introducing a blocking layer of Al_2O_3 between two dyes while fabricating the DSSC [60]. All these processes while improving the efficiency of DSSCs, involve an increase in the number of steps for device fabrication, and therefore, tend to be cumbersome at a commercial scale.

b) ***<u>Electrolyte:</u>*** Electrolytes typically consist of a redox couple and additives dissolved in a liquid solvent. The main function of the electrolyte is the dye regeneration and charge transport between the TiO_2 photoanode and platinized counter electrodes. The photovoltaic performances of dye-sensitized solar cells mainly depend on the choice of redox couple and on the choice of electrolyte solvent employed. Generally, either organic solvents or ionic liquids have been used as liquid electrolyte solvents in DSSC. A huge number of organic solvents have been employed such as alcohols, ethylene carbonate, tetrahydrofuran, acetonitrile, propionitrile, valeronitrile, methoxyacetonitrile etc. Acetonitrile (ACN) has been the most successfully and efficient organic solvent used in electrolytes due to its low viscosity, good solubility to dissolve organic components and additives. However, owing to its high vapor pressure and liquid electrolyte, leakage and evaporation of solvent has become a critical issue in encapsulation of devices. In this regard, less volatile organic solvents such as 3-methoxypropionitrile (MPN) and butyronitrile got great attention owing to its high boiling point which showed a good stability performance, retaining over 90% of their initial efficiencies under light soaking at 60°C for 1000 hours [61]. However, the common problems of leakage and evaporation are still investigated by employing polymer matrix materials.

c) ***<u>Counter electrode:</u>*** The catalytic activity of counter electrodes is the main important step for the efficient reduction of triiodide ions into iodide ions at the surface of the electrode. So far platinum (Pt) coated on FTO glass substrates is the most common catalyst material used for reduction of I_3^- to I^- ions in redox electrolyte due to its excellent electrochemical activity. In this regard, various methods have been used for the formation of Pt thin layer, such as sputtering, electro-deposition, and electrophoresis, in which sputtering is the most commonly employed method. However, sputtering requires ultra-high vacuum environment and uses more amount of platinum to produce one flat surface while the amount of Pt necessary to obtain the desired catalytic effect is very small. The usage of platinum as a counter electrode in DSSCs has been limited (However, the commercial viability of platinum as CE has been limited) because of

i. High cost and limited flexibility,
ii. Corrosion of the platinum in presence of small traces of water in the electrolyte,
iii. High temperature processing (> 400ºC),
iv. Platinum dissolution in corrosive electrolyte and formation of PtI_4 and H_2PtI_6 [62].

To address these issues, a great deal of research is oriented towards finding an alternative to platinum counter electrodes. In the pursuit, conducting polymers show the promise for enabling the replacement of platinum CEs in DSSC because of their unique properties, including low cost, ease of synthesis, good catalytic activity, and remarkable stability. Many conducting polymers such as, poly(3,4-ethylenedioxythiophene) (PEDOT) [63], poly(3,3-diethyl-3,4-dihydro-2H-thieno-[3,4-b][1,4]dioxepine) (PProDOT-Et_2) [64], polyaniline [65], and polypyrrole [66] were studied as alternative CEs for DSSCs. In most cases, the films of conducting polymers were prepared by spin casting on TCO substrates and annealed at high temperatures in order to improve film adhesion on TCO substrate. However, the conducting polymer films prepared in this manner have limited thickness. Additionally, the poor film adhesion on the substrate requires high temperature processing. In order to avoid the use of high temperature processing, Xia *et. al.* [67] deposited conducting polymer films on TCO substrates by vapor phase polymerization in two steps: first an oxidant material was spin casted on TCO substrate and then the substrate was kept in monomer saturated vapor to polymerize the monomer on the substrate. However, the conducting polymer films formed this way have low surface area owing to the limited thickness of the film. It is reported that conducting polymers based CEs require thicker and porous films for efficient charge transport properties. This issue was addressed by adopting template assisted electrochemical deposition of conducting polymer, which resulted in high surface area films [68]. However, the electrochemical deposition of conducting polymers requires TCO substrates, which adds to the cost of the DSSCs. Since the use of TCO substrate and platinum account for 50% of the total cost of DSSCs [69], a greater need for the development of cost effective (TCO-free and Pt-free) counter electrodes are required.

All these components play a vital role in determining the overall efficiencies of the DSSCs, and therefore, their roles need to be investigated in detail.

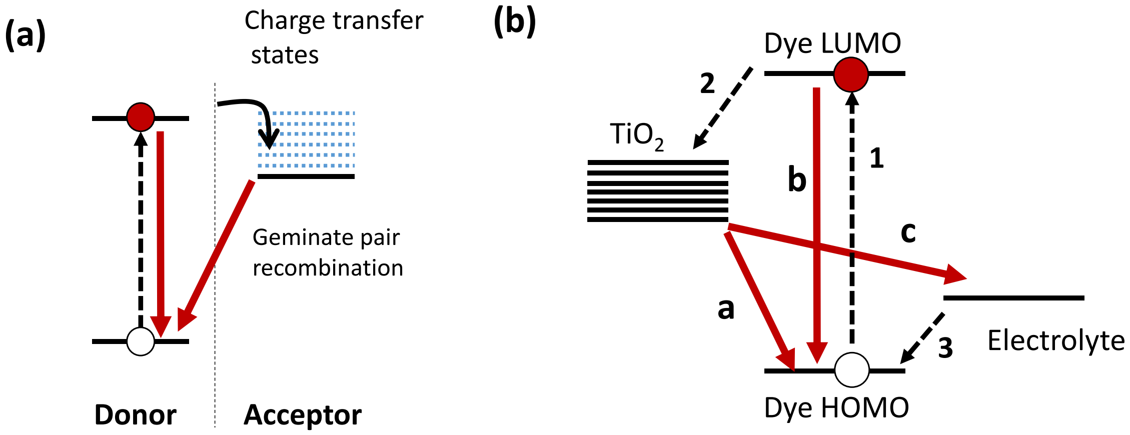

Figure 1.14: Various possible recombination processes (indicated with red solid line) occurring in (a) polymer solar cells, and (b) dye-sensitized solar cells.

1.5 Scope of thesis

Polymer solar cells as well as dye sensitized solar cells are promising candidates for the flexible and low-cost photovoltaic devices. In the case of polymer solar cells the efficiency depends on several factors, such as, molar extinction coefficient of donor and acceptor materials, energy gap, energy level alignment between donor-acceptor phases, exciton dissociation, interface between donor and acceptor phases, extraction and collection of carriers and selectivity of hole/electron transport layers etc. For dye sensitized solar cells the major factors that govern the efficiency are molar extinction coefficient of dyes, energy gap, energy level alignment between dye and TiO_2 semiconductor, charge injection, charge recombination, electrolyte leakage and evaporation, catalytic activity of counter-electrodes etc. However, in both polymer and dye sensitized solar cells, as shown in Fig. 1.14, recombination is a major factor that strongly influence the efficiency. In case of polymer solar cells, geminate and bimolecular recombinations are predominant, whereas in case of dye-sensitized solar cells recombinations at TiO_2-dye (recombination with the oxidized dye), and TiO_2-electrolyte (recombination with the oxidized redox mediator) interface are significant. In both devices, presence of disorders at the interfaces causes trapping of charge carries, which enhances the charge recombination. Therefore, in order to enhance the efficiency it is essential to minimize the disorders in the devices, which can be done by optimizing the materials parameters (i.e. morphology, structure, interfaces etc).

Both polymer and dye sensitized solar cells have been investigated because the primary aim of the thesis is to develop low cost and flexible technologies. Among such technologies, polymer and DSSC have been selected due to following similarities between them:

a. Fabrication uses similar contact materials and substrates i.e. Indium tin oxide (ITO) or Fluorine tin oxide (FTO) coated glass substrates.

b. Both type of devices have varying degree of sensitivity to environment and involve similar encapsulation techniques.

c. Conducting polymers are used in both type of solar cells (for example solid state DSSC also use polymer hole transport layers) and we have employed free-standing polypyrrole in DSSC and poly(3-hexylthiophene) and PEDOT:PSS etc. in polymer solar cells.

d. ZnO, TiO_2 and other inorganic semiconductor nanomaterials are employed in both type of solar cells: as photoanode in DSSC and electron transport layer in polymer solar cells.

e. Both devices require similar understanding of semiconductor organic molecules and use solution processes for fabrication. Similar techniques as electrochemistry, infrared absorption spectroscopy are used for characterization.

This thesis aims at fabrication of both polymer and dye sensitized solar cells with an emphasis to enhance their efficiency by tailoring the materials properties. We have measured the photovoltaic characteristics of the devices and estimated various device parameters by fitting to an equivalent circuit model. The correlations between materials parameters and device parameters have been established. The specific devices investigated during this thesis work are as follows:

(i) Polymer solar cells namely, bulk-heterojunction P3HT:PCBM, porphyrin/polyfullerene diffuse bilayer solar cells, and porphyrin-modified ZnO-NW/P3HT hybrid solar cells, have been investigated.

(ii) Dye-sensitized solar cells have been fabricated using: (a) different photoanodes e.g. ZnO or TiO_2; (b) photoanodes sensitized using single or two dyes; (c) different electrolytes, liquid or gel; and (d) different counter-electrodes, Pt or novel free-standing polypyrrole films.

The experiments and obtained results on above mentioned investigations have been organized into following chapters

In Chapter 2, we describe details of experimental procedure employed for the fabrication of diffuse bilayer solar cells and bulk-heterojunction polymer solar cells; growth of ZnO nanostructures by hydrothermal method; fabrication of dye-sensitized solar cell; synthesis of novel gel polymer electrolyte and free-standing polypyrrole films. The details of various characterization tools studied during the thesis work are presented.

In Chapter 3, results of various studies pertaining to bulk-heterojunction P3HT:PCBM, porphyrin/polyfullerene diffuse bilayer solar cells, and porphyrin-modified ZnO-NW/P3HT hybrid solar cells are discussed. The devices characteristics of P3HT:PCBM BHJ solar cells were found to depend upon annealing temperatures. Therefore, temperature dependent *in-situ* Raman spectroscopy of P3HT:PCBM films were investigated to gain insight into the structural and morphological changes. Diffuse bilayer solar cells, were fabricated by simultaneous deposition of porphyrin and fullerene films on ITO substrates yielding moderate photo-responses. In hybrid solar cells, the modification of ZnO-NW surface with porphyrin yields better performance as compared to ZnO-NW/P3HT configuration.

In Chapter 4, the dye-sensitized solar cells were fabricated using different photoanodes, electrolytes and counter-electrodes. Briefly, we show that a proper selection of an organic dye with ZnO photoanodes results in better performances compared to ruthenium counterparts. In addition, the major recombination loss in TiO_2 photoanodes was restricted with an application of co-adsorbent (formic acid), which later used as an anchoring site for a co-sensitization of two dyes resulting in improved efficiencies. A gel polymer electrolyte was synthesized to prevent common leakage and evaporation problem of typical liquid based electrolytes. A novel free-standing polypyrrole films synthesized by interfacial polymerization were applied as substrate-free, TCO-free counter-electrodes for cost effective DSSC.

The summary of the present thesis work and the future scope of work are presented in Chapter 5.

Chapter -2

Experimental and Characterization Techniques

This chapter deals with the brief description of various materials employed in the fabrication of polymer and dye-sensitized solar cells and details of the fabrication processes. In addition, brief descriptions of the equipment utilized for the fabrication and characterization of the solar cells are presented.

2.1 Materials

The molecular structures of various materials employed in the fabrication of both polymer and dye-sensitized solar cells are presented in Appendix (Fig. A1 & Fig. A2). The key materials employed during this thesis work are presented as follows.

2.1.1 Materials for polymer solar cells

(a) *ITO Substrates*: Indium tin oxide (ITO) coated glass substrates were purchased from *Visiontek systems ltd., U.K.* The soda lime float glass is coated with a primary layer of silicone oxide (SiO_2), which acts as a barrier layer and secondary layer of ITO with a thickness of 150nm. These substrates have a sheet resistance of 6 – 12 ohm/sq as measured by four-probe resistivity, transmittance >80% at 550 nm as measured by UV-Vis spectroscopy, and rms roughness of 0.5 nm measured by atomic force microscopy. These properties make ITO substrates ideal for the fabrication of polymer solar cells.

(b) *PEDOT:PSS* - Poly(3,4-ethylenedioxythiophene) poly(styrenesulfonate) of make *Heraeus Clevios*™ (PH1000) was purchased from *Ossila, U.K.* PEDOT:PSS thin films on glass substrates have conductivities of 100 S/cm measured by four-probe resistivity, transmittance > 80 % at 550 nm as measured by UV-Vis spectroscopy. PEDOT:PSS thin films have a work function of 5.1 eV, which matches energetically with most p-type conducting polymers and ITO substrate acting as a hole transport material.

(c) _P3HT:_ Poly(3-hexylthiophene-2,5-diyl) of make *Plextronics (Plexcore® OS 2100)* was purchased from *Sigma Aldrich, India*. P3HT is an electronic grade material with an average molecular weight M_n = 54000-75000, ultra-high purity (< 25 ppm trace metals), and regioregularity (98% head-to-tail), was employed as an electron donor material in polymer solar cells.

(d) _PCBM:_ [6,6]-Phenyl C_{71} butyric acid methyl ester ([70]PCBM), hereafter termed as PCBM, was purchased from *Sigma Aldrich, India.* PCBM is a functionalized fullerene (suitable for solution processing) with extended visible absorption for more energy harvesting, which is employed as an electron acceptor material in polymer solar cells.

(e) _Porphyrin:_ 5,10,15,20-tetrakis(4-hydroxyphenyl)- porphyrin, hereafter termed as THPP, was purchased from *Sigma Aldrich, India.* Porphyrin being naturally occurring chromophore has a strong visible absorption, was employed as an electron donor for bilayer polymer solar cells.

(f) _Fullerene:_ Sublimed grade fullerene (C_{60}), with 99.9 % purity was purchased from *Sigma Aldrich, India.* Fullerene which has a high electron-affinity, was polymerized via electro-polymerization and later used as an electron acceptor for bilayer polymer solar cells.

(g) _Aluminum:_ Aluminum evaporation slug with 99.999% trace metal basis was purchased from *Sigma Aldrich, India* for deposition of top metal contacts for both bilayer and bulk-heterojunction solar cells.

(h) *Sealant:* UV curable encapsulation epoxy has been used for sealing polymer solar cells fabricated in Glove Box, which was purchased from *Ossila Limited, U.K.* The devices fabricated inside the Glove Box are sealed for photovoltaic characterization.

(i) *Kelvin clips:* The contacts for top and bottom electrodes of the sealed devices are made by using a gold coated flat alligator clip (known as Kelvin clips), purchased from *Synkera Technologies Inc.*

(j) *Solvents:* 1,2-dichlorobenzene (anhydrous) was used in the preparation of Active layer mixture, methanol (anhydrous) & dichloromethane (anhydrous) were used for electro-deposition of poly-THPP and poly-fullerene films. Hellmanex-III glass cleaning detergent, ultrapure milli-Q water, semiconductor grade solvents (Acetone, 2-propanol) were used for cleaning ITO substrates.

2.1.2 Materials for dye-sensitized solar cells

(a) *FTO Substrates*: Fluorine-doped tin oxide (FTO) coated glass substrates, with trade name "TCO22-7" were purchased from *Solaronix Inc. Switzerland.* As the preparation of nanostructured TiO_2 electrodes and platinum counter electrodes involve high annealing temperatures of 450ºC, FTO has been the only choice of TCO, stable at these temperatures. These substrates have a sheet resistance of 7 ohm/sq, with transmittance >80% at 550 nm.

(b) *Photoanodes*

(i) ZnO photoanodes: For the growth of ZnO nanostructures, Zinc acetate dihydrate of reagent grade with purity >98 %, AR grade Sodium hydroxide

(NaOH) pellets (purity >98.5%), reagent grade Zinc nitrate hexahydrate ($Zn(NO_3)_2 .6H_2O$) with purity 98%, and ACS reagent grade hexamethylenetetramine (HMT) with purity >99% were purchased from *Sigma Aldrich, India.*

(ii) TiO_2 photoanodes: Highly transparent nanocrystalline Titanium dioxide (TiO_2) paste with trade name "Ti-Nanoxide HT" was purchased from *Solaronix Inc. Switzerland.* The paste containing anatase TiO_2 nanoparticles of 8-10 nm yields highly transparent films after deposition.

(c) *Sensitizer Dyes*

(i) Organic dyes – High molar extinction coefficient BODIPY based laser dye with trade name "PM567" was synthesized in our research labs. Rhodamine 19 perchlorate (RhCl) with absorption maxima at 517nm was purchased from *Sigma Aldrich, India.*

(ii) Ruthenium dyes – Widely employed ruthenium polypyridyl complex, N3 dye (cis-bis(isothiocyanato)bis(2,2'-bipyridyl-4,4'-dicarboxylato)-ruthenium(II)) was purchased from *Solaronix Inc. Switzerland.*

(d) *Electrolyte:* Electrolyte containing I^-/I_3^- redox couples were prepared by using Lithium Iodide (LiI) and Iodine (I_2) purchased from Sigma Aldrich, India. Solvents required for different types of organic, aqueous, and gel polymer electrolyte were purchased from Sigma Aldrich India.

(e) *Counter electrodes*

(i) Platinum precursor: Hexachloroplatinic(IV) acid with 11-15% Pt in Iso-propanol was purchased from *Merck GmbH.*

(ii) Pyrrole: Analytical grade pyrrole was purchased from *Sigma Aldrich, India* to synthesize polypyrrole thin films via electro-deposition and interfacial polymerization.

(f) *Sealant:* Prior to photovoltaic characterization, the devices were sealed by using either a parafilm or a 60 μm thermoplast hot-melt sealing foil. (Suryln®, *Solaronix Inc.)*

2.2 Fabrication of polymer solar cells

2.2.1 Glove box: spin coater and thermal evaporator

Conducting polymers and small molecules commonly employed in the fabrication of solar cells readily degrade (are doped) when exposed to atmospheric conditions. Hence, an inert Glove Box (MB 20G, M. BRAUN INERTGAS-SYSTEME GMBH) with oxygen and moisture levels <0.1 ppm, was used to fabricate the polymer solar cells. The Glove Box system works by the principle of gas circulation, where the working gas circulates between the Glove Box and the gas purifier. The gas purification system removes moisture and oxygen from the inert gas Glove Box atmosphere. It utilizes a proprietary reactive agent to withdraw oxygen from the inert gas and a proprietary adsorbent to remove water, thus maintaining both H_2O and O_2 at <0.1 ppm. The photograph of the Glove Box is shown in the Fig. 2.1. The custom-made Glove Box contains two boxes, Box 1 contains a Spin coater (Delta6 BM/TT, *Suss Microtec Lithography GmbH*) for deposition of thin films and Box 2 contains a thermal evaporator (custom made by BOC Edwards Inc.) for metal contacts. The entire fabrication of polymer solar cells starting from solution preparation to final device encapsulation is carried out in Glove Box.

Figure 2.1: The photograph of the MBraun modular glove box system.

2.2.2 Fabrication process

In this section we describe the detail fabrication process of P3HT:PCBM bulk-heterojunction solar cells, porphyrin/polyfullerene diffuse bilayer solar cells, and porphyrin-modified ZnO-NW/P3HT hybrid solar cells

(a) P3HT:PCBM bulk-heterojunction solar cells

Bulk-heterojunction polymer solar cells with a device architecture of ITO/PEDOT:PSS/P3HT:PCBM/Al were fabricated inside Glove Box as depicted in schematically Fig. 2.2. The steps involved in the fabrication are as follows:

(i) ITO substrates were cut into required dimensions of 1” x 1”, and patterned into definite stripes by masking through a tape. These masked substrates are placed in Acid etchant solution for 30 min. The patterned substrates are subsequently cleaned using detergent, de-ionized water, acetone and 2-propanol respectively.

(ii) hole transport layer PEDOT:PSS (thickness: 50 nm) was deposited onto clean ITO substrates by spin coating, which were then transferred to glove box having moisture and oxygen <0.1 ppm. These samples were then annealed at 130^{o}C for 30 min.

(iii) A mixture of P3HT and PCBM (with 1:1 W/W, 20 mg/ml) were dissolved in 1,2-dichlorobenzene solvent by continuous stirring for 24 hrs and later filtered through 0.45 μm syringe filters. An active layer P3HT:PCBM (thickness:100 nm) layer was deposited by spin coating the filtered solution onto PEDOT:PSS coated ITO substrates. These samples were annealed at various temperatures between 25 and 180°C for 30 min.

(iv) The solar cell configuration was established by thermal deposition of Al under a base vacuum of ~ 10^{-6} torr through a shadow mask to obtain an active area of 6 mm^2.

(v) These solar cells were encapsulated using UV curable epoxy inside the glove box and taken out for the photovoltaic characterization.

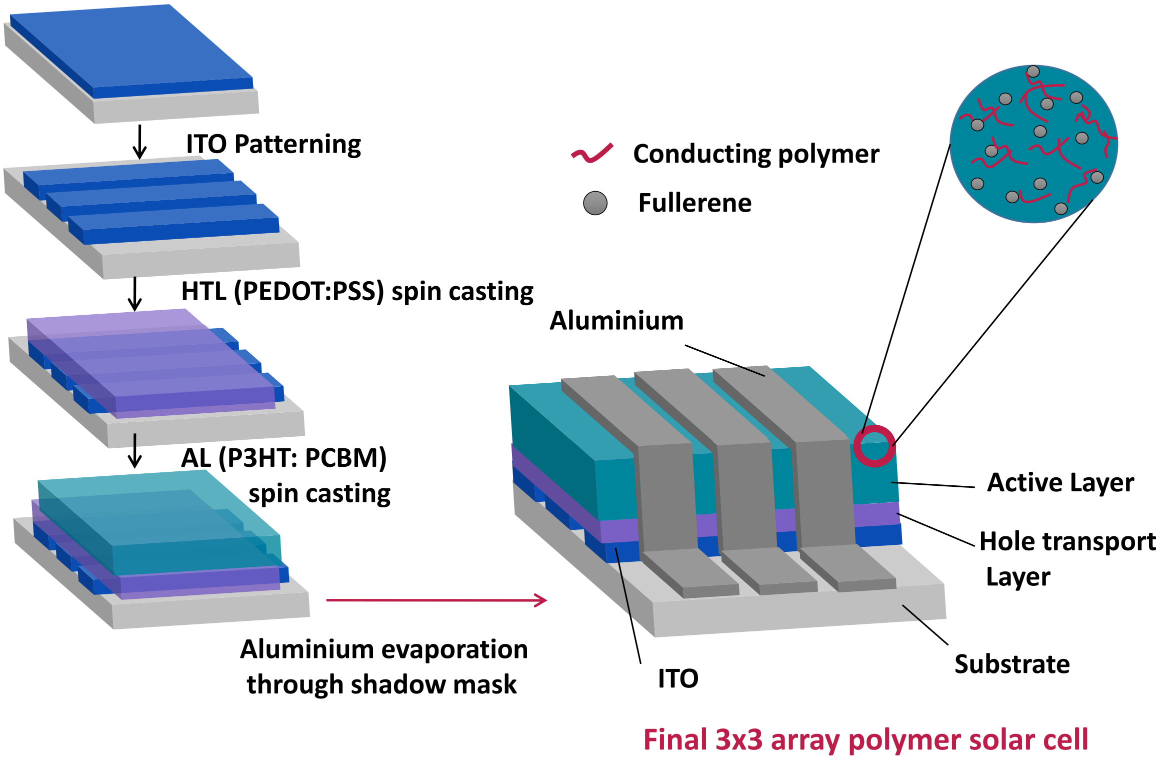

Figure 2.2: A schematic depiction of various processes involved in making 3 x 3 array polymer solar cell.

(b) Porphyrin/polyfullerene diffuse bilayer solar cells

Bilayer polymer solar cells were fabricated by sequential deposition of donor and acceptor layers on ITO substrates as mentioned below. A schematic picture representing fabrication of bilayer solar cells is shown in the Fig 2.3. Firstly, porphyrin was electro-deposited on PEDOT:PSS coated ITO substrates which acts as donor, and later poly-fullerene films were electro-deposited on top of porphyrin films, thus forming a bilayer heterojunction. Finally, thermal evaporation of Al defines the active area of the devices. The deposition of porphyrin films and poly-fullerene films are presented individually as follows.

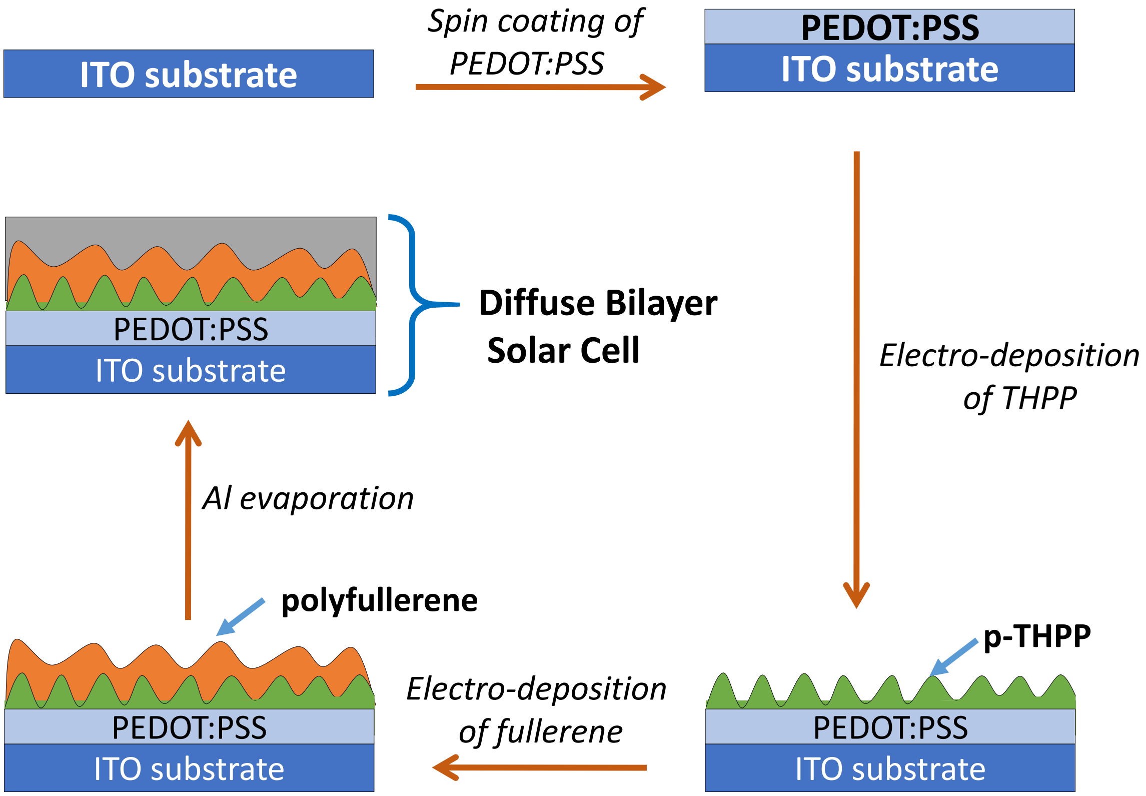

Figure 2.3: Schematic depiction of fabrication of bilayer solar cells

Electro-deposition of porphyrin: The following procedure was employed for electro-deposition of 5,10,15,20-tetrakis(4-hydroxyphenyl)porphyrin (THPP) on ITO substrates.

(i) 1mM THPP in methanol as a monomer solution and 0.1M tetra butyl ammonium perchlorate (TBAP) in methanol as a supporting electrolyte are prepared in volumetric flasks.

(ii) After total dissolution of the above two solutions, they are mixed in 1:1 (V/V) ratio in a separate weighing bottle.

(iii) The solution is now placed in a conventional three electrode cell where ITO substrate acts as working electrode, platinum strip as counter electrode, and Ag/AgCl wire as reference electrode.

(iv) The polymerization is carried out with a potentiostat/galvanostat system by cyclic voltammetry (CV) method. Briefly for electro-deposition, the solution mixture is cycled between 0 to 1V for 5-100 cycles/scans at a scan rate of 50 mVs^{-1}.

(v) This yields in uniform growth of polymeric THPP on ITO substrates.

(vi) The porphyrin coated substrates are washed in methanol, dried under N_2 stream and stored in desiccator under dark, which are later characterized by spectroscopic techniques and used as a working electrode for deposition of poly-fullerene, to fabricate diffuse bilayer solar cells.

<u>*Electrodeposition of polyfullerene films:*</u> The following procedure was employed to electro-polymerize fullerene on ITO substrates

(i) The ITO coated glass substrates were first cleaned with detergent, ultrasonicated in acetone and isopropyl alcohol, and subsequently dried under Argon flow.

(ii) C_{60} solution (0.72 mM) in Dichloromethane was extensively sonicated prior to use and mixed (1:1, v/v) in a 0.1M TBAP.

(iii) The resulting solution was reduced extensively at -1.5V vs Ag/AgCl reference electrode using platinum strip as working and counter electrode.

(iv) After reduction (a color change from pale pink to pale brown was observed), linear sweep voltammetry was carried using ITO as working electrode and electrochemical measurement was done.

(v) It is observed that the thickness of C_{60} films increased with no. of linear sweeps.

(vi) All characterizations were performed in an ambient environment without a protective atmosphere.

(c) Hybrid solar cells

Growth of ZnO-NWs on ITO substrates

A two-step process has been followed to grow ZnO nanowires from ZnO seed particles [70, 71], and the growth of ZnO nanostructures were schematically depicted in Fig 2.4.

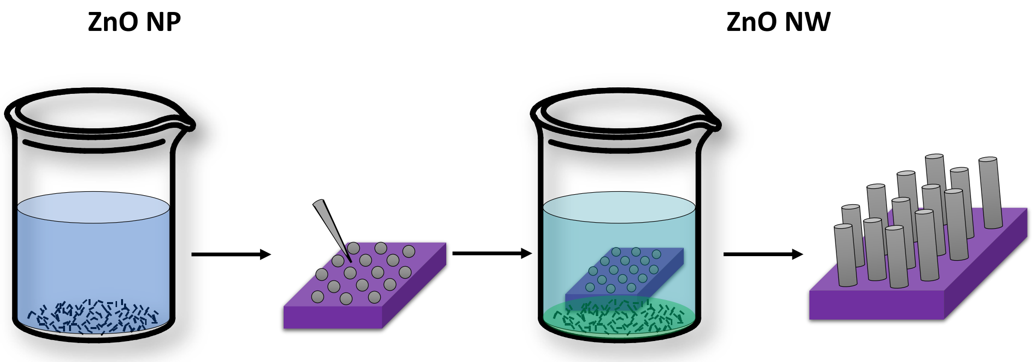

Figure 2.4: Schematic depiction of ZnO NW growth on ITO substrates via hydrothermal route through ZnO nanoparticles. The schematic shows step by step process from seed layer to nanowire growth

The major steps involved are:

Step 1: ZnO NPs have been synthesized by acetate route, where 50 mM zinc acetate dihydrate and 100 mM NaOH solution in ethanol were reacted for 6 h at temperature, 70–75°C, to produce ZnO nanocrystals of size, 15-30 nm. Our objective was to control the density of the nanorods that were grown on these seeds. The density of the rods grown depends on the density of the seed particles. To grow the nanorod arrays with controlled density, we have optimized the process using different amounts of ZnO seed particles. ZnO nanoparticles so formed were of size 30-40 nm, which were used as the seed layer for ZnO NWs array growth. The ZnO nanoparticles were dispersed thoroughly in ethanol and then coated onto ITO substrates by drop casting different amounts of the solution. The seeded substrates were annealed for 1hr at a temperature of 150°C for good adhesion of seed particles on to the substrate. The seed layer thus prepared, act as nucleating sites for growth of nanowires due to the lowering of the thermodynamic barrier [72].

Step 2: The ZnO NWs are grown by solution phase hydrothermal route due to ease of handling, low temperatures, low cost, and scalability for large area applications. A precursor solution containing an equimolar mixture of zinc nitrate hexahydrate ($Zn(NO_3)_2 .6H_2O$) and alkaline reagent (such as hexamethylenetetramine (HMT)) are used for ZnO NW growth. The various chemical reactions occurring with this precursor solution are presented in Eq. 2.1 - 2.4. The ZnO seeded substrates were dipped in constantly stirred aqueous solution of 30 mM $Zn(NO_3)_2. 6H_2O$and 30 mM HMT for 6hrs at a temperature of 95°C. The seed layer promotes the nucleation for the growth of ZnO NW due to lowering of the thermodynamic barrier [72]. The resultant substrates were then washed with de-ionized water followed by annealing at 120ºC in vacuum for 30 minutes, in order to improve adhesion of ZnO NW onto ITO substrates.

The following chemical reactions occur during the growth of ZnO NW’s

i. Decomposition reaction:

$$(CH_2)_6N_4 + 6H_2O \rightarrow 6HCHO + 4NH_3 \qquad (2.1)$$

ii. Hydroxyl supply reaction:

$$NH_3 + H_2O \leftrightarrow NH_4{}^+ + OH^- \quad (2.2)$$

iii. Supersaturation reaction:

$$2OH^- + Zn^{2+} \rightarrow Zn(OH)_2 \quad (2.3)$$

iv. ZnO nanowire growth reaction:

$$Zn(OH)_2 \rightarrow ZnO + H_2O \quad (2.4)$$

Fabrication of hybrid solar cells

Two different solar cells were fabricated by employing device structures (i) ITO/ZnO-NW/P3HT/Au and ITO/porphyrin-modified ZnO-NW/P3HT/Au as depicted schematically in Fig 2.5.

(i) The hybrid solar cells with device configuration as shown in Fig. 2.5 (a) are fabricated by spin-coating P3HT solution onto ZnO-NW electrodes thermally grown on grown on patterned ITO substrates, followed by thermal evaporation of gold.

(ii) The hybrid solar cells with device configuration as shown in Fig. 2.5(b) are fabricated by first electrodepositing porphyrin film onto ZnO-NW electrodes (hereafter called as porphyrin-modified ZnO-NW), followed by spin-coating of P3HT and thermal evaporation of gold.

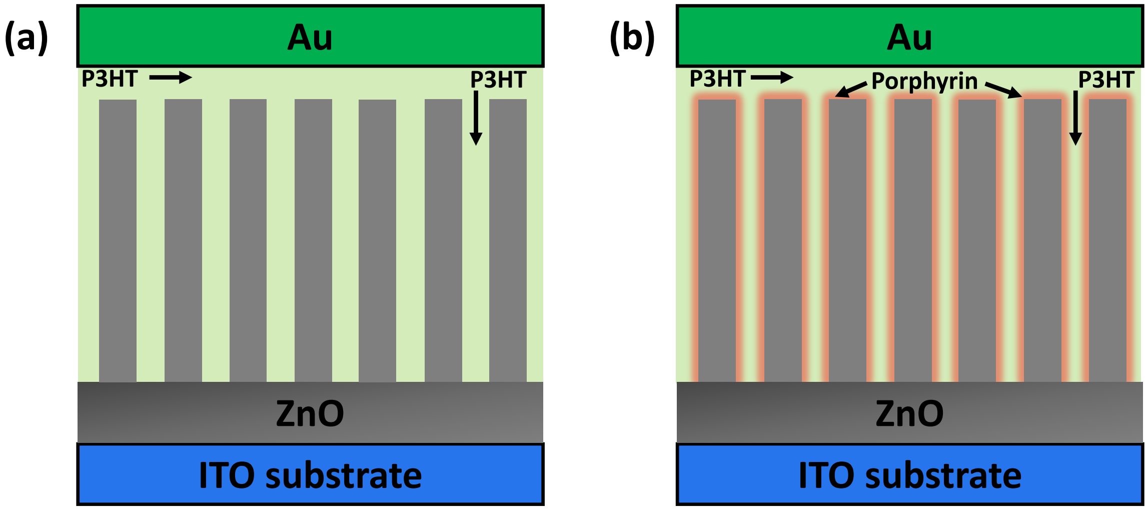

Figure 2.5: Hybrid solar cells based on (a) ZnO-NW structures and (b) porphyrin-modified ZnO-NW structures.

2.3 Fabrication of dye-sensitized solar cells

2.3.1 Fabrication process

The fabrication of dye-sensitized solar cell involves preparation of three individual components, instead polymer solar cells are fabricated on single substrate. (i) Fabrication of photoanodes on FTO substrates, (ii) Fabrication of counter electrode on either FTO or ITO substrates, and (iii) preparation of redox electrolyte. The fabrication of all these individual components are discussed below briefly.

2.3.2 Synthesis of photoanodes

As mentioned in Chapter 1, typical photoanodes are either prepared by ZnO nanostructures or TiO_2 nanostructures. The fabrication of this two photoanodes are discussed briefly.

(a) ZnO photoanodes

ZnO-NWs on ITO substrates as described in above section were used as ZnO photoanodes for dye-sensitized solar cells.

(b) Co-sensitized TiO_2 photoanodes

In the present work we used following two dyes for the co-sensitization: (i) Rhodamine 19 perchlorate, which is a very stable and economical laser dye and has not been explored earlier for DSSC, and (ii) N3 dye (widely employed ruthenium polypyrrole complex). RhCl dye was chosen on account of its high molar extinction coefficient ($2\times10^5 M^{-1}cm^{-1}$) as compared to N3 dye (10^4 $M^{-1}cm^{-1}$) owing to which only a little amount of RhCl dye is required to be absorbed on TiO_2 surface for yielding sufficient optical density for effective PCE. Briefly, the co-sensitized electrode is fabricated as follows:

(i) TiO_2 photoanodes are prepared by doctor blading TiO_2 paste (solaronix make) on FTO substrates, followed by annealing at 450ºC for 30 mins in a tubular furnace.

(ii) Prior to sensitization, the TiO_2 electrode was treated with formic acid solution (0.05M in ethanol) for 2 h and later washed with ethanol and dried under N_2 stream.

(iii) This formic acid treated TiO_2 electrode were refluxed in a round bottomed flask containing RhCl dye solution (0.6 mg/ml in ethanol) equipped with a water-jacketed reflux condenser and a heating source at 70°C for 2 h. This RhCl dye coated electrodes were later removed and washed with ethanol and dried under N_2 stream.

(iv) RhCl sensitized TiO_2 photoanodes are later dipped in N3 dye solution (0.3 mg/ml in ethanol) for different time intervals (t_d) and later washed with ethanol solvent and dried under N_2 stream thus forming co-sensitized TiO_2 photoanodes.

2.3.3 Synthesis of electrolyte

Electrolytes typically consist of a redox couple and additives dissolved in a liquid or quasi gel. The main function of the electrolyte is the dye regeneration and charge transport between the TiO_2 photoanode and platinized counter electrodes. Electrolytes employed in the present thesis work are described below.

a) *Organic electrolyte 1:* Typically this electrolyte is prepared by mixing 0.1 M LiI and 0.05 M I_2 in dry acetonitrile organic solvent.
b) *Organic electrolyte 2:* this electrolyte is prepared by mixing 0.1 M LiI and 0.05 M I_2 in dry 3-methoxypropionitrile solvent.
c) *Aqueous electrolyte 1:* Briefly the electrolyte is prepared with 0.5 M LiI and 0.05 M I_2 in deionized water.
d) *Aqueous electrolyte 2:* Briefly the electrolyte is prepared with 0.01 M $FeCl_3$ and 0.1M KCl in deionized water.
e) *Gel polymer electrolyte:* The quasi-solid state electrolyte or gel polymer electrolyte (GPE) is the electrolyte being in a state of both liquid and solid coexistence. Generally, this electrolyte is defined as a system which consists of a polymer network (polymer host) swollen with liquid electrolytes. Quasi-solid-state electrolytes are usually prepared by incorporating a large amount of a liquid electrolyte into organic monomer or polymer matrix, forming a stable gel with a network structure via a physical or chemical method. Briefly, it is prepared by first dissolving 1.338 g lithium iodide (LiI) and 0.254 g Iodine (I_2) in 4 ml propylene carbonate and 10 ml acetonitrile solution and then 3 g of polyethylene oxide (PEO,

MW– 1×10^6, Alfa Aesar) was added to this mixture. Later, this mixture was heated at 70–80°C under continuous stirring for 7–8 h. Finally, a homogeneous highly viscous GPE was obtained.

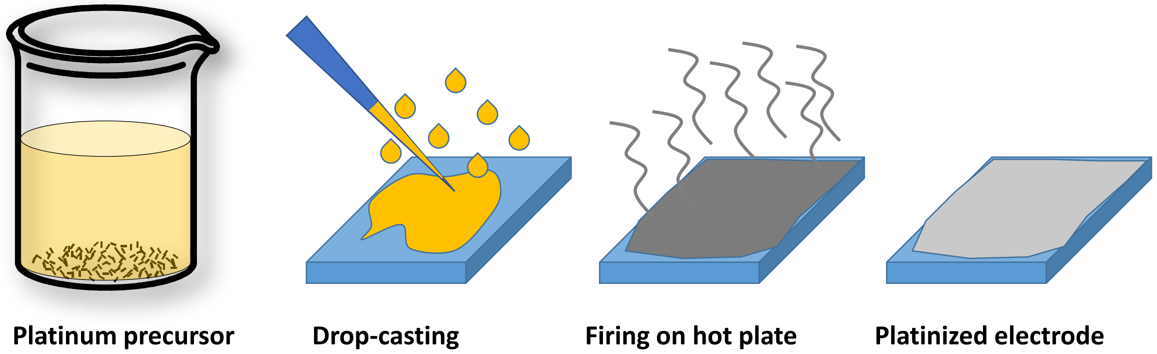

Figure 2.6: Schematic depiction of preparation of platinum films on FTO electrodes with hexachloroplatinic acid solution.

2.3.4 Synthesis of counter electrodes

The fabrication details of counter electrodes used in the present thesis work are briefly discussed in the following:

a) *Pt/FTO counter electrode:* These counter electrodes are prepared by thermal decomposition of platinum either by drop-casting or spin-coating of 5 mM H_2PtCl_6 in 2-propanol solution on FTO substrate, and reducing the Pt precursor in the air furnace at 450°C for 30 min (as schematically depicted in Fig. 2.6). Although the thermal cluster Pt has many advantages, such as, low Pt loading, the superior catalytic activity, and good mechanical stability, it requires heating up to 450°C, which is energy consumptive and not suitable for commercial applications and flexible solar cells.

b) *Growth of free-standing polypyrrole films:* Pyrrole (Aldrich, 98%) was double distilled under reduced pressure prior to use. PPy free-standing films were synthesized typically by placing 20 ml, 0.1M aqueous $FeCl_3$ and 20 ml, 0.1M pyrrole in dichloromethane (DCM) in a beaker for varied times (4hrs to 18 hrs). A free-standing PPy film of thickness ~ 1μm is formed at the liquid-liquid interface after 4 hrs. The free-standing PPy film thickness increases with polymerization time, and finally a thick 75 μm film was formed after 18 hrs. These films are later lifted onto glass/plastic substrates, and subsequently, washed with de-ionized water and DCM to remove un-reacted $FeCl_3$ and pyrrole. The films thus obtained were dried overnight and can be handled using a pair of tweezers (shown in Fig.2.7).

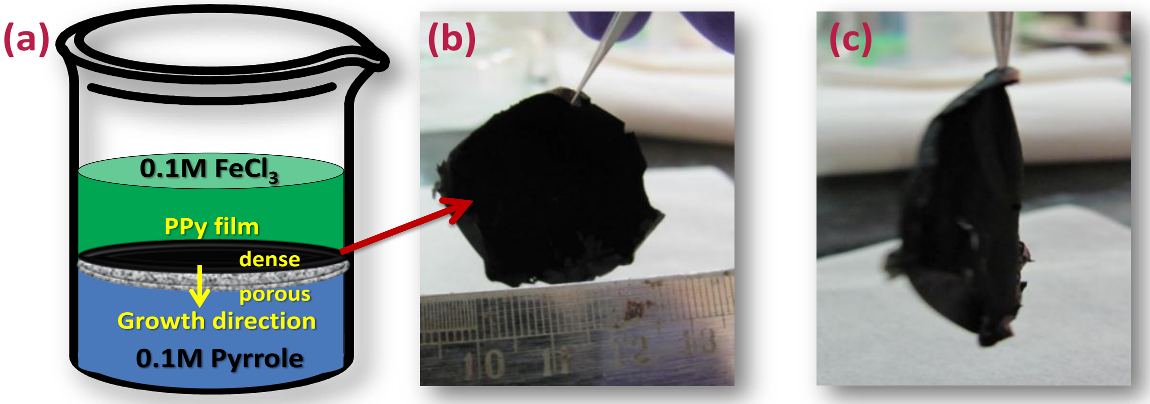

Figure 2.7: (a) Schematic showing the formation of free-standing PPy films at the aqueous (0.1 M $FeCl_3$)/organic (0.1 M pyrrole) interface. (b) & (c) Photograph of the free-standing PPy films mechanically lifted with a pair of tweezers.

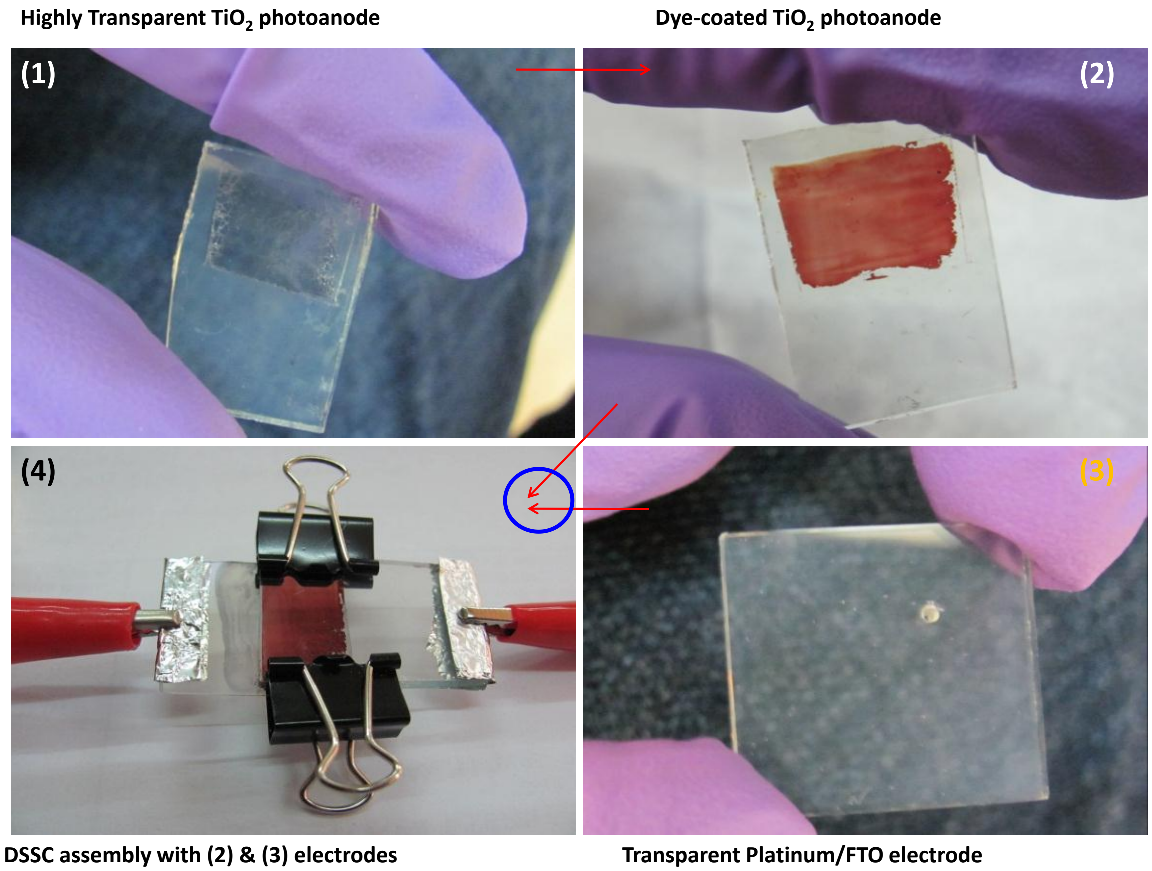

Figure 2.8: Photographs of DSSC components, (1) Highly transparent TiO_2 photoanode, (2) Dye-coated TiO_2 photoanode, (3) platinum/FTO counter electrode, and (4) DSSC assembly with (2) and (3) electrodes

2.3.4 Device assembly

All the three components (i.e, photoanode, electrolyte, and counter electrode) are assembled together as described in Fig. 2.8. The dye coated electrode and counter-electrode are either sandwiched together by using a stretched parafilm or suryln thermoplastic film as spacer. The electrolyte is injected between the electrodes through a perforated counter electrode by using a vaccum syringe filter and later encapsulated with epoxy or surly film. The assembled device is thus characterized by taking connections through alligator clips.

2.4 Characterization techniques

Several characterization techniques were employed during the course of thesis, which are described briefly as follows

UV- visible spectroscopy: UV-Vis spectroscopy is an absorption/reflectance spectroscopy technique used to determine the electronic transitions of materials, whose absorption is in the ultraviolet and visible region of an electromagnetic spectrum. The following data were recorded by using (Jasco V-530) UV-Vis spectrophotometer.

a) The transmittance of ITO, FTO, PEDOT:PSS coated ITO, Pt/FTO, electro-deposited platinum on ITO/PEN substrates.
b) Absorption of conducting polymers, PCBM, porphyrin dye in solution and their respective films.
c) Absorbance of dye sensitized photoanodes and the amount of dye loading on TiO_2 photoanodes were recorded.

Fourier transform infrared spectroscopy: Fourier Transform Infrared spectroscopy (FTIR) provides the information of different vibrational frequencies related to chemical bonds and the nature chemical functional groups present in the organic molecule. FTIR works on the principle of interferometer that gives an interferogram, a plot of light intensity versus optical path difference. This interferogram is finally Fourier transformed to give a spectrum of infrared radiation intensity versus wave number. The following spectra were recorded using Bruker spectrometer (model: Vertex 80 V) in ATR mode from 4000 to 400 cm^{-1} with a resolution of 4 cm^{-1}. Prior to measurements, the instrument was calibrated by recording the spectra with a standard sample.

a) The electro-deposited fullerene films were characterized by FTIR for the confirmation of poly-fullerene.
b) Structural changes in TiO_2 photoanode after acid treatment, the adsorption of dye molecules onto TiO_2 photoanodes are recorded by FTIR spectroscopy.

Scanning electron microscopy: The SEM is the focused probe of electrons accelerated to a moderately high energy and positioned on to the sample by electro-magnetic fields. These beam electrons interact with atoms of the specimen by inelastic (energy is transferred to the sample leads to secondary electrons emission) and elastic (energy is not transferred to the sample leads to back scattered electrons emission) collisions. The most widely used signal, produced by the inelastic interaction of the primary electron beam with the sample is the secondary electron signal, which is used for examining surface structure with best resolutions <100 nm. The surface morphologies of thin films deposited by either spin-coating or electro-deposition or interfacial polymerization technique are imaged by TESCAN (VEGA MV2300T/40) scanning electron microscopy at an accelerating voltage 30 kV.

Atomic force microscopy: Nanonics (Multiview 4000) atomic force microscopy was used in the present thesis work to image surface morphology of thin films. Briefly, the probe used for imaging is made of the glass fiber tip (diameter 10nm) which is attached to tuning fork with piezocrystal. The images are recorded in the tapping mode by oscillating the tip at resonance frequency (20-50 kHz depending on the tips). The probe was scanned in phase mode. During scan, phase changes due to tip surface interaction. The difference in signal called an error signal; t signal is sent to proportional, integrator and differentiator (PID) controller. PID sends the feedback via high voltage piezo driver to make constant phase by moving piezo driver in z direction at that x, y point, thus generating an image. The surface morphology with surface roughness of ITO/FTO substrates, thin films deposited by spin-coating or electro-deposition technique were imaged in the present work. Prior to imaging, the system was calibrated by imaging a standard grid (defined Au pads of 10 μm x 10 μm x 120 nm on Si wafer)

Kelvin probe microscopy: Kelvin probe microscopy is a versatile technique to measure the surface potentials of the samples. In this technique an AC voltage with frequency of 27kHz is applied to gold coated tip mounted just above the sample surface which is kept at a ground potential. When the tip is at a proximal distance to the sample, it senses an electrical force, which is used as a feedback to estimate the work-function of sample. The work-function measurements were performed at room temperature and ambient conditions using Au electrode having tip diameter of 2mm. 2D work function mapping of ITO/FTO substrates, PEDOT:PSS thin films, electro-deposited porphyrin and polyfullerene films are imaged by KP technology (SKP 5050) kelvin probe system.

Raman spectroscopy: Structural characterization of PEDOT:PSS, P3HT:PCBM, Porphyrin thin films are studied by Jobin-Vyon (LabRAM HR800) Raman spectrophotometer. The spectra were collected in the 180^o backscattering geometry using the Ar$^+$ laser (514nm) as an excitation source. *In-situ* Raman measurements of P3HT:PCBM films were recorded by placing 1" x 1" substrates in a Linkam (THMS 600) heating stage, which has an accuracy and stability of 0.1^{o}C. Prior to measurements, the system was calibrated by using the spectral position of Si wafer. The obtained spectra were fitted using a Lorentzian function to determine the peak position, bandwidth and intensity ratio with Labspec5 software.

Photovoltaic characterization

a) *Current-Voltage (J-V) characteristics*: current-voltage characteristics of polymer solar cells and dye-sensitized solar cells were recorded with computer controlled Keithley 2400 digital source-meter and PARSTAT32 potentiostat/galvanostat. For photovoltaic characterization, the measurements were measured using a custom made solar simulator (Sciencetech, Canada) under 1sun (AM1.5G), 100 mW/cm^2 illumination. Prior to measurements, the intensity of the solar simulator was calibrated using a reference silicon solar cell.

b) *Incident-photon to current conversion efficiency (IPCE)*: The spectral response of dye-sensitized solar cells were measured using custom made solar simulator (Sciencetech, Canada).

c) *Electrochemical Impedance Spectroscopy:* Electrochemical impedance spectroscopy (EIS) technique is employed to study the various electron transfer processes occurring at the interfaces, during the operation of DSSC. EIS measurements were carried out by using potentiostat/Galvanostat (PGSTAT 30, Autolab, Eco Chemie, Netherlands), the DSSC was kept at open circuit potential and an AC amplitude of 10mV was applied under an illumination of 1 Sun (AM 1.5 G, 100 mW/cm^2). The measured data were fitted by using ZSimpwin software.

d) *Solar cell parameter evaluation:* The obtained (measured) current-voltage characteristics of both polymer and dye-sensitized solar cells were fitted by using Shockley one diode equation (Eq. 1.6). The fitted solar cell parameters (ideal diode factor, diode saturation current, series resistance, shunt resistance, and photogenerated current) are presented with respective *J-V* characteristics.

Chapter -3

Bulk-heterojunction and bilayer polymer solar cells

In this Chapter, the results on the characteristics of P3HT:PCBM bulk-heterojunction solar cells measured as a function of annealing temperature are discussed. In order to investigate the temperature dependent evolution of structural/morphological changes in P3HT:PCBM films, the results of in-situ optical and Raman spectroscopy are presented and a correlation between the morphology and efficiency of P3HT:PCBM solar cells is established. We also present results on the two different types of bilayer solar cells: (i) porphyrin/polyfullerene solar cells fabricated for the first time using electrochemical technique. For this purpose, the growth mechanism of electrodeposited porphyrin and polyfullerene films on ITO substrates are investigated. (ii) porphyrin-modified ZnO-NW/P3HT hybrid solar cells.

3.1 P3HT:PCBM bulk-heterojunction polymer solar cells

As discussed in Chapter 1, BHJ polymer solar cells based on P3HT and PCBM blends are widely studied owing to their low-cost, flexibility, ease of material synthesis and manufacturing advantages[14-18]. In these solar cells, thermal annealing is widely employed as post processing treatment for controlling the morphology of the blend, and hence, the efficiency. Literature survey shows that the best efficiency is obtained when the active layer is annealed at a temperature in the range of 120-150°C[13, 44]. As of now it is not fully understood that how annealing processes affects the ordering of molecules, morphology and domain size of each component in the P3HT:PCBM films. In order to gain an insight into the annealing induced structural and morphological changes, we present *In-situ* Raman spectroscopy - a powerful inelastic light scattering based technique that is capable of monitoring the nanoscale changes in the polymer structure through the measurement of vibrational modes[73].

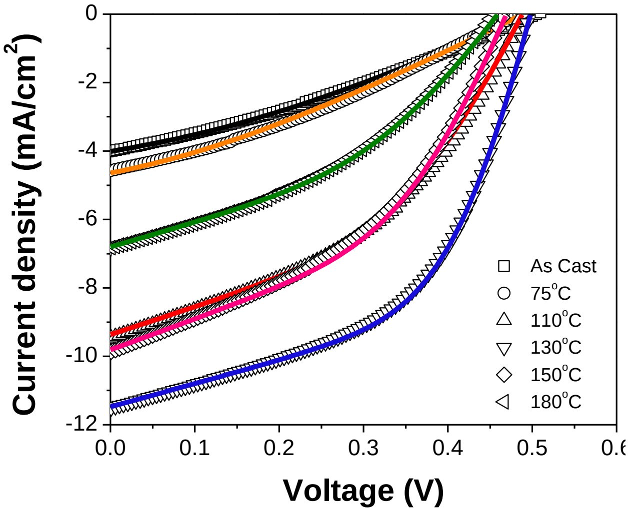

Figure 3.1: Measured (symbol) and fitted (solid line) *J–V* characteristics of as-prepared and thermally annealed (at various temperatures) P3HT:PCBM bulk-heterojunction solar cells.

3.1.1 Photovoltaic characteristics

Fig. 3.1 shows the measured current-voltage (*J-V*) characteristics of as-prepared and thermally annealed (75°C, 110°C, 130°C, 150°C, and 180°C for 30 min) P3HT:PCBM bulk-heterojunction solar cells, which were measured under AM 1.5G, 1 Sun illumination. From these data, various photovoltaic parameters i.e. open-circuit voltage (V_{oc}), short-circuit current (J_{sc}), fill factor (FF), and power conversion efficiency (η) were calculated. The variation of these parameters as a function of annealing temperature is shown in Fig. 3.2. From this figure following inferences can be drawn:

(i) The value of V_{oc} is ~0.5 V for as fabricated solar cells, which almost remains independent of the annealing temperature upto 130°C. However for higher annealing temperatures it marginally decreases.

(ii) J_{sc} initially remains unaffected upto 75°C, increases rapidly with annealing temperature and attains a maximum of 12.4 mA/cm^2 at 130°C. However at higher annealing temperature the J_{sc} decreases sharply. This behavior is associated with structure/morphological evolution as a function of annealing temperature, and this will be elaborated in the next section.

(iii) Both FF and η follows the same trend as that of J_{sc}, indicating a critical role played by annealing induced structure/morphology of the P3HT:PCBM films. The maximum values FF and η obtained at 130°C are 0.5 and 3.1% respectively. The value of η is reasonable considering the fact that we have not employed any electron transport layers. A higher efficiency is normally obtained when calcium is used as top electrode and Lithium fluoride is used as electron transport layer [74].

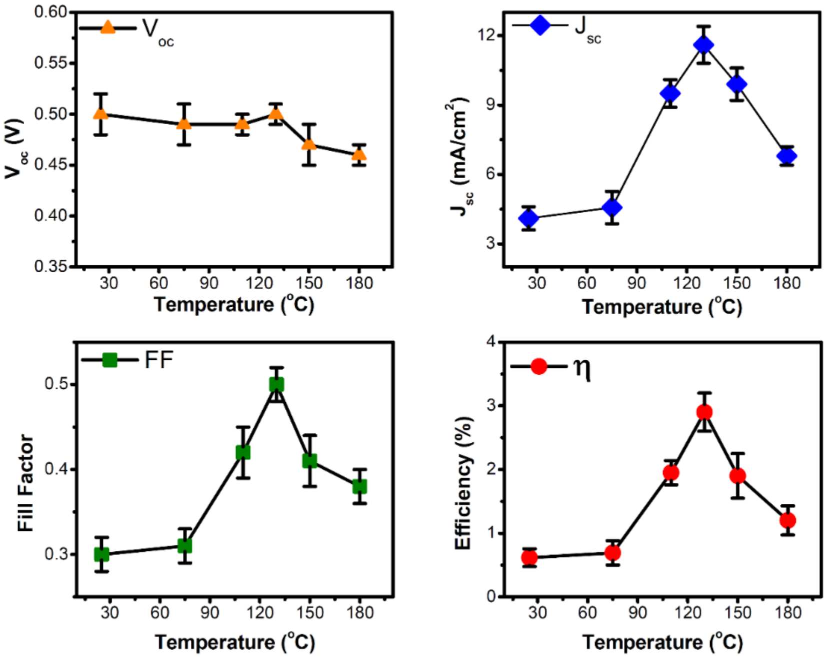

Figure 3.2: Variation of different photovoltaic parameters namely open-circuit voltage (V_{oc}), short-circuit current (J_{sc}), fill factor (*FF*), and power conversion efficiency (η) of P3HT: PCBM bulk-heterojunction solar cells as a function of annealed temperature.

The measured *J-V* characteristics presented in Figure 3.1 were fitted using the Shockley one diode equation (Eq. 1.6). The initial values of various parameters i.e., ideality factor (*n*), diode saturation current (*I₀*), series resistance (*Rₛ*), shunt resistance (*Rₛₕ*), and photogenerated current (*Iₚₕ*) were estimated as follows[75].

At short circuit condition, I = I_{sc} and V = 0, Eq. 1.6 becomes

$$I_{sc} = I_0\left\{exp\left(\frac{qR_sI_{sc}}{nk_BT}\right) - 1\right\} + \frac{R_sI_{sc}}{R_{sh}} - I_{ph} \tag{3.1}$$

At open circuit condition, I = 0, and V = V_{oc}, Eq. 1.6 derives as

$$0 = I_0\left\{exp\left(\frac{qV_{oc}}{nk_BT}\right) - 1\right\} + \frac{V_{oc}}{R_{sh}} - I_{ph} \tag{3.2}$$

Combining Eqs. 3.1 and 3.2, leads to

$$I_0 = \frac{\left(I_{sc} + \frac{R_sI_{sc} - V_{oc}}{R_{sh}}\right) exp\left(\frac{-qV_{oc}}{nk_BT}\right)}{1 - exp\left(\frac{q(R_sI_{sc} - V_{oc})}{nk_BT}\right)} \tag{3.3}$$

and

$$I_{ph} + I_0 = \frac{I_{sc} + \frac{R_sI_{sc} - V_{oc}}{R_{sh}}}{1 - exp\left(\frac{q(R_sI_{sc} - V_{oc})}{nk_BT}\right)} + \frac{V_{oc}}{R_{sh}} \tag{3.4}$$

The above expressions can be simplified if we make the assumption that

$$exp\left(\frac{q(R_sI_{sc} - V_{oc})}{nk_BT}\right) \ll 1 \tag{3.5}$$

this assumption reduces Eqs. 3.3 and 3.4 to

$$I_0 = \left(I_{sc} + \frac{R_sI_{sc} - V_{oc}}{R_{sh}}\right) exp\left(\frac{-qV_{oc}}{nk_BT}\right) \tag{3.6}$$

$$I_{ph} + I_0 = I_{sc} + \frac{R_sI_{sc}}{R_{sh}} \tag{3.7}$$

Again from Eq. 1.6, *dV/dI* is expressed as

$$\frac{dV}{dI} = \frac{nk_BT/q}{I_{ph}+I_0+I-\left(V-R_sI-\frac{nk_BT}{q}\right)/R_{sh}} + R_s \tag{3.8}$$

Substituting Eq. 3.7 into 3.8,

$$\frac{dV}{dI} = \frac{nk_BT/q}{I_{sc}+I-\frac{V}{R_{sh}}+\frac{nk_BT}{qR_{sh}}+\frac{(I+I_{SC})R_S}{R_{sh}}} + R_s \tag{3.9}$$

At short-circuit condition, I = I_{sc}, and V=0

$$\left.\frac{dV}{dI}\right|_{I=I_{sc},V=0} = R_{sh} + R_s \approx R_{sh} \tag{3.10}$$

And around the open-circuit condition (I=0 and V=V_{oc})

$$\frac{dV}{dI} = \frac{nk_BT/q}{I_{sc}+I-\frac{V}{R_{sh}}+\frac{nk_BT}{qR_{sh}}+\frac{(I+I_{SC})R_S}{R_{sh}}} + R_s \tag{3.11}$$

$$\approx \frac{nk_BT/q}{I_{sc}+I-\frac{V}{R_{sh}}} + R_s \tag{3.12}$$

Which can be rewritten as

$$\frac{dV}{dI} = \left(\frac{V_t}{I_{sc}+I-\frac{V}{R_{sh}}}\right) \times n + R_s \tag{3.13}$$

Where V_t (= k_BT/q = 0.0258V) is thermal voltage.

The initial values of n and R_s are calculated by linear fitting of *dV/dI* as a function of V_t / (I_{sc} + I – V/R_{sh}). The value of y-intercept yields the value of R_s and the slope gives the value of *n*. Using these calculated initial values of *n*, R_s, and R_{sh}, and experimentally measured values of I_{sc}, and V_{oc} the initial values of I_0 and I_{ph} were calculated using Eqs. (3.6) and (3.7). Using these initial values, the transcendental equation (1.6) is solved using softwares, and the extracted parameters are summarized in Table 3.1.

Table 3.1: Solar cell parameters evaluated from current-voltage characteristics presented in Fig. 3.1.

Device parameters	**P3HT-25**	**P3HT-75**	**P3HT-110**	**P3HT-130**	**P3HT-150**	**P3HT-180**
n	2.4	2.2	1.69	1.55	1.6	1.78
R_s (Ω-cm^2)	78	70	14.5	6	11.5	21
R_{sh} (kΩ-cm^2)	0.28	0.32	0.11	0.14	0.10	0.12
I_0 (nA/cm^2)	1100	790	84	33	72	190
I_{ph} (mA/cm^2)	5.25	5.90	10.60	11.96	10.94	8.0
I_{sc} (mA/cm^2)	4.0	4.6	9.5	11.5	9.8	6.8
V_{oc} (V)	0.50	0.49	0.49	0.50	0.47	0.46
FF (%)	0.3	0.32	0.42	0.49	0.4	0.39
η (%)	0.7	0.9	2.1	3.2	2.2	1.4

From Table 3.1 it is evident that the active layer annealed at 130ºC, yields highest efficiency of 3.2 %, along with lowest value of n, I_0, R_s and highest values of I_{ph}. These results indicate that there a correlation among the materials and device parameters. Before, we discuss these correlation, it is essential to investigate why an annealing temperature of 130ºC leads to best efficiency. It may be noted that similar annealing temperature variation in η has been reported by several groups [76-78], with an optimum temperature in the 110-150°C range. This relatively wide annealing temperature range could be possibly due to a difference in the temperature calibration of the heating stage. To under this behavior, we have investigated the structure/morphological evolution by conducting the *in-situ* Raman as well as optical microscopy, which were further supported by *ex-situ* AFM, SEM, elemental x-ray imaging and UV-Vis spectroscopic measurements. The results of these studies are discussed below.

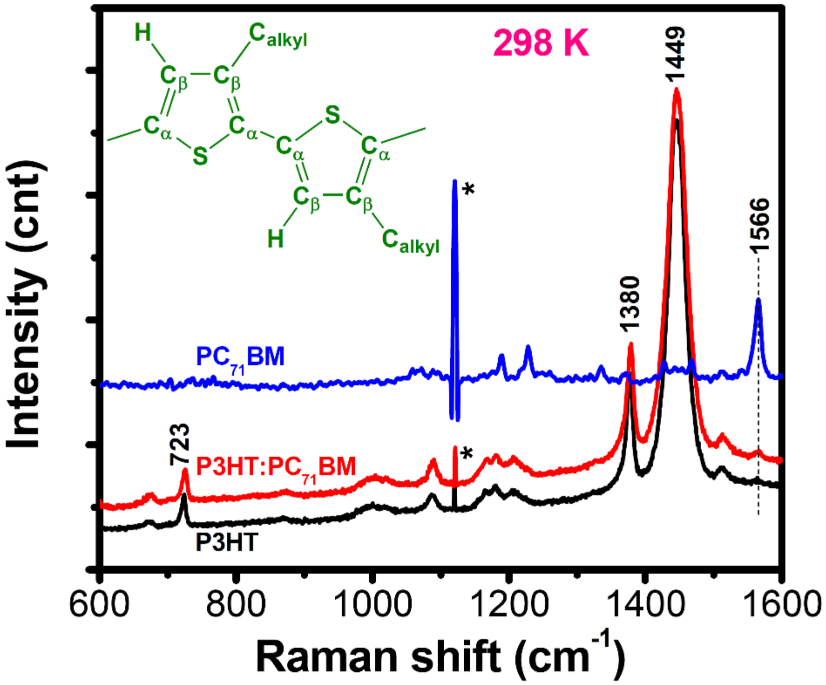

Figure 3.3: Raman spectra of as-cast P3HT, PCBM and P3HT:PCBM films recorded using 514 nm excitation. Inset shows the molecular structure of P3HT molecule. Substrate peak is represented by(*).

3.1.2 In-situ Raman spectroscopy and optical microscopy

Typical Raman spectra of as-deposited P3HT, PCBM and P3HT:PCBM films reordered at room temperature are shown in Fig. 3.3. The inset of the figure shows the molecular structure of P3HT. Various identified Raman modes observed in the case of P3HT films are 1449 cm^{-1} (symmetric C=C stretch mode), 1380 cm^{-1} (C-C intra-ring stretch mode), 723 cm^{-1} (C-S-C ring deformation), 1204 cm^{-1} (inter-ring C-C stretch mode) and 1170 cm^{-1} (C-H bending mode with C-C inter-ring stretch mode)[79, 80]. Among various these modes, symmetric C=C ring stretching (1449 cm^{-1}) and skeletal C-C stretching (1375 cm^{-1}) modes are of major concern, as they are sensitive to π-electron delocalization i.e. conjugation length[80, 81]. In literature, Raman spectra of P3HT and P3HT:PCBM films under both non-resonant (e.g. excitations at 785 and 633 nm) and resonant (e.g. excitations at 514, 488 or 496.5 nm) excitations have been reported[79-81]. It has been shown that the peak position of C-C mode at 1380 cm^{-1} is not only insensitive to degree of molecular order, but also to the excitation wavelength i.e. same for the non-resonant and resonant excitation. On the other hand, for C=C mode, its peak position, line-width and intensity is found to strongly dependent on the excitation wavelength (i.e. resonant excitation yield better results as compared to non-resonant excitation) and the molecular ordering. Therefore, Raman shift of P3HT C=C mode can be used as a measure of the conjugation length due to its symmetry with respect to the conjugation direction. The blue shift in this mode, therefore, indicates reduced conjugation length which might arise due to disorder occurring in the P3HT chains or PCBM incorporation as reported by Tsoi and Carach[80, 82]. In the case of PCBM films, the major peak observed at 1566 cm^{-1} corresponds to $A_{1'}$ mode[83].

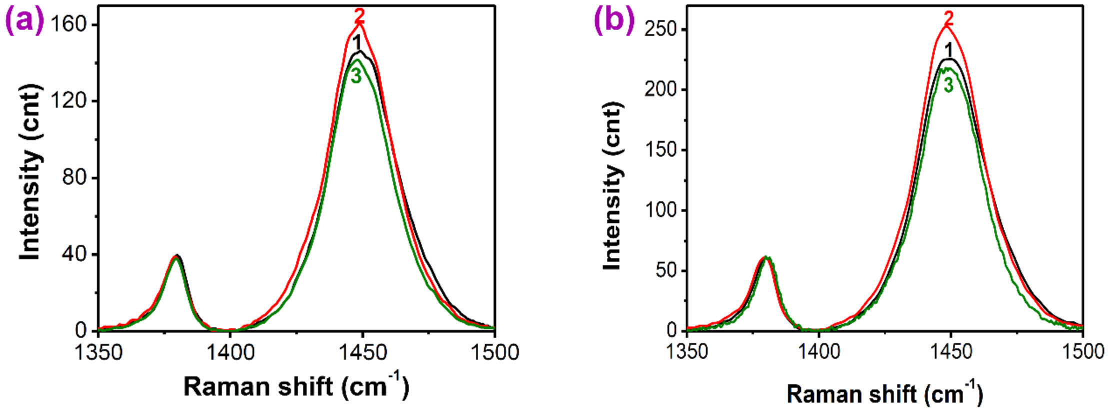

Figure 3.4: Typical normalized Raman spectra with respect to the intensity of the C–C mode for (a) P3HT and (b) P3HT:PCBM films. (1) as-deposited films at room temperature; (2) at 130°C and (3) again at room temperature after cooling from 130°C.

For P3HT:PCBM films, peaks corresponding to both P3HT as well as the predominant peak of PCBM have been observed, indicating presence of both P3HT and PCBM. In order to gain insight into the evolution of P3HT:PCBM structure, the *in-situ* Raman spectra of pristine P3HT and P3HT:PCBM films were recorded during both heating and cooling cycles at an interval of 25-30°C. In different experiments, films were annealed to different temperatures between 75°C and 180°C. Typical Raman spectra normalized with respect to the intensity of C-C stretching mode for P3HT and P3HT:PCBM films during different stages of thermal annealing are shown in Fig. 3.4. It is evident that the symmetric C=C stretching mode ($\nu_{C=C}$) undergoes a slight blue shift on heating to 130°C; while cooling back to room temperature it has a red shift. In the literature it has been reported that the P3HT C=C band consists of contributions from ordered (aggregated) and amorphous (un-aggregated) components which appear at 1450 cm^{-1} and 1470 cm^{-1}, respectively[80]. The relative ratio of these contributions are dependent on the processing conditions as well as regioregularity of the P3HT[81]. Tsoi *et al.* [80] have carried out detailed analysis of regioregular and regiorandom P3HT, and found high degree of ordered components (1450 cm^{-1}) in case of regioregular P3HT having FWHM ~31 cm^{-1}. In our case, both P3HT and P3HT:PCBM blend already have significant ordered structure as indicated by relatively narrow FWHM ~26 cm^{-1} of C=C peak. Such differences in the films may arise because of differences is the sample preparation. In our case, high molecular weight P3HT was used and the cast films were left overnight in the glove box. The slow evaporation of the solvent may lead to slightly high molecular ordering in P3HT films than reported by Gao *et al*[81]. Because of relatively low concentration of amorphous region, the deconvolution of C=C Raman peak does not provide two Lorentzian curve fitting. Therefore, we have extracted FWHM from the fitted single Lorentzian curve to the C=C Raman mode. When the temperature is raised to 180°C, contributions from the amorphous region (1470 cm^{-1} peak) is increased, which intrinsically have broader linewidths.. This lead to broader FWHM~35 cm^{-1} owing to linear dependence of the spontaneous Raman scattering on the concentration of scatterers. As temperature decreases, P3HT chains re-assemble into aggregates causing an increase of the crystalline component. The slight blue shift in C=C Raman mode on heating suggest molecular disorder in P3HT which in present case is induced by thermal annealing. During cooling, a red shift in this mode occurs, suggesting that during cooling the P3HT undergoes molecular ordering.

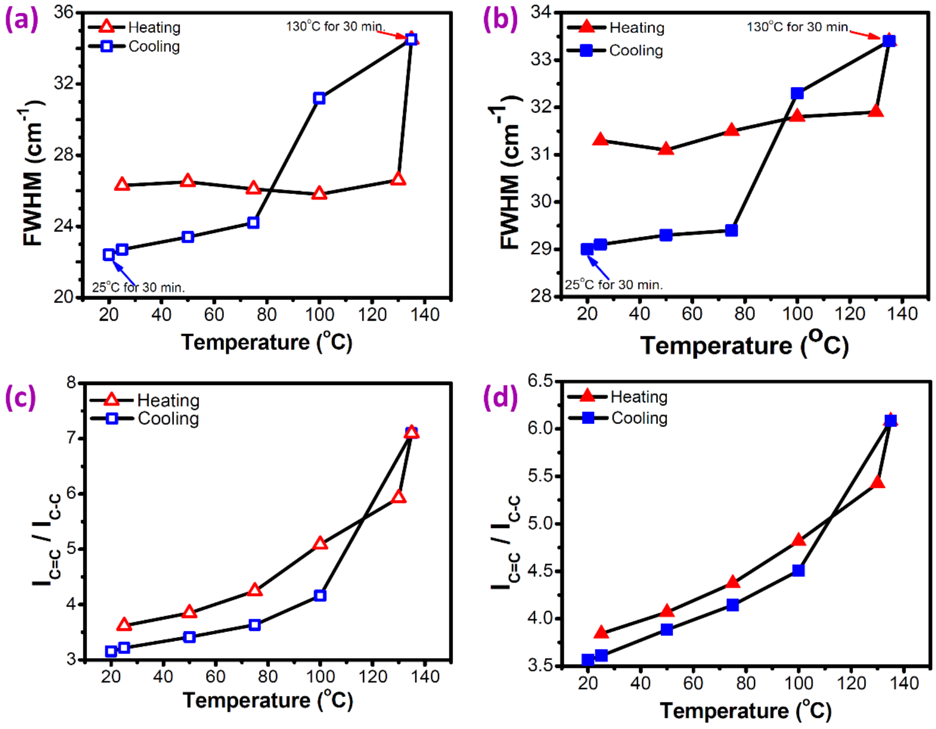

Figure 3.5: (a) and (b) are the variation of full-width-half-maximum (FWHM) of symmetric C=C stretching mode for P3HT and P3HT:PCBM films, respectively during heating and cooling cycles upto annealing temperature of 180°C. (c) and (d) are the variation of the C=C/C–C intensity ratios for P3HT and P3HT:PCBM films, respectively during heating and cooling cycles of annealing temperature upto 130°C.

The molecular ordering of P3HT was further supported by the data on full-width half-maximum (FWHM) of symmetric C=C stretching mode (1449 cm^{-1}) and C=C/C-C intensity ratio ($I_{C=C}/I_{C-C}$). The variation of FWHM and $I_{C=C}/I_{C-C}$ (extracted by fitting the data with Lorentzian) as a function of heating as well cooling cycles for P3HT and P3HT:PCBM films (annealed upto a maximum temperature of 130°C) are plotted in Fig. 3.5. The major inference drawn from these results are as follows.

(i) It is well established that smaller values of FWHM is indicative of improved ordering of P3HT chains. As shown in Fig. 3.5 (a) and (b), the lower FWHM value of as-deposited P3HT film (cm^{-1}) as compared to that of P3HT:PCBM film, suggests that the inclusion of PCBM hampers the ordering of P3HT[84]. In both the case, during heating the FWHM increases, which is expected owing to the thermal induced disordering of P3HT chains. On the other hand, during cooling cycle the FWHM decreases sharply at ~100^{o}C, indicating thermally induced H-aggregation (or π-stacking) of polymer chains. After annealing, the FWHM's at room temperature are lower as compared to pre-annealed films, suggesting that the molecular ordering is frozen in the films.

(ii) The intensity of C-C intra-ring stretch mode relative to C=C Raman mode is sensitive to the conjugate backbone planarity of the P3HT. Based on the simulated C=C and C-C Raman modes in oligothiophene, Tsoi *et al.* [80] have suggested that planarity of the P3HT chains is higher for higher relative intensity of C-C mode and vice versa. This might be because of better electron-phonon coupling of C-C mode and/or increased charge transfer from C=C bonds. More planar backbone conformation favors the π-stacking of the polymer chains and therefore, results in more molecular ordering. Fig. 3.5 (c) & (d) clearly shows that $I_{C=C}/I_{C-C}$ ratio increases with temperature during heating cycles, which indicates an increase in disorder in the films that is in agreement with the FWHM measurements. A lower value of $I_{C=C}/I_{C-C}$ after completion of the cooling cycle also supports the fact that annealing enhances the molecular ordering owing to an increase of π electron density in C-C bonds resulting from an increase in planarity of P3HT chains[81].

In order to find out how the film morphology evolves as a function of annealing temperature, we have carried out in-situ optical imaging during heating as well as cooling cycles of the annealing. Typical optical images for the films subjected to the annealing of 130 and 180°C are shown in Fig. 3.6. As shown in Fig. 3.6 (a1-a3), the morphology of the films remains uniform when heated upto 130°C and subsequently cooled down to room temperature. However, this situation is not the same when the films are annealed upto 180°C, as shown in Fig. 3.6(b1-b3). It is seen that at 180°C large aggregate of size 2-4 µm forms at the surface, which remains there on the surface even after cooling. This result suggests that a phase segregation occurs when films are annealed to temperatures >130°C [85]. Similar results of P3HT:PCBM blends were observed by Yang *et al.* [86] and Hoppe *et al.* [87]. Using transmission electron microscopy (TEM) and SEM results, they have shown that thermal annealing leads to the crystallization of P3HT chains via stacked coplanar conjugated segments and dispersion of PCBM molecules forming large aggregates. A detailed study of the thermal annealing effect on PCBM aggregation was reported by Kiel *et al.* [88]. On the basis of their neutron reflectivity results, they showed that upon annealing the PCBM concentration is increased at the sample-air interface and a little change at the buried interface of substrate and blend.

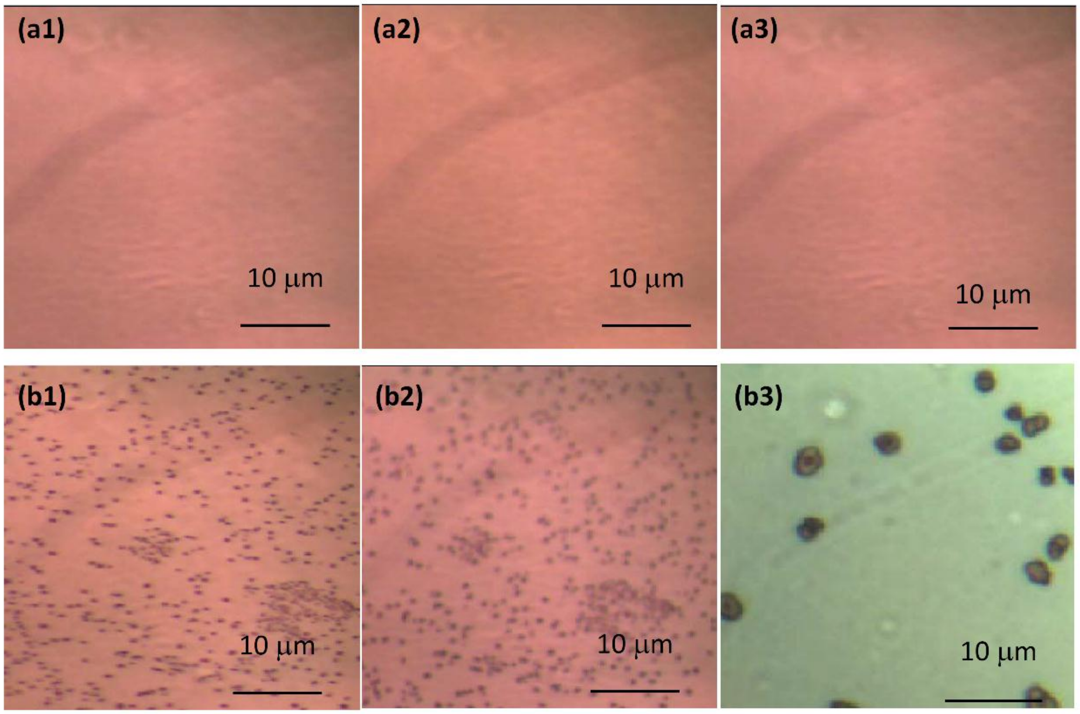

Figure 3.6: Real time optical micrographs of P3HT:PCBM films at different temperatures (a1) room temperature, (a2) at 130°C after 30 min of annealing, and (a3) at 25°C after cooling from 130°C. (b1) morphology at 180°C after 30 min of annealing, (b2) morphology at 25°C after cooling from 180°C, and (b3) magnified version of b2 image.

3.1.3 Ex-situ Raman and UV-Vis spectroscopy

As discussed above, the *in-situ* Raman spectroscopic and optical microscopic studies clearly show that when P3HT and P3HT:PCBM films are annealed to 130°C, the disorder nature increases in the films due to thermal energy, while molecular ordering of P3HT chains takes place during the cooling cycle. In order to investigate the role of maximum annealing temperature, the Raman spectra were recorded at room temperature after subjecting them to various annealing temperatures i.e. 110, 130, 150, and 180°C. Fig. 3.7(a) shows the recorded Raman spectra in the C=C stretching mode region of

P3HT:PCBM films. The calculated FWHM values as a function of annealing temperature are plotted in Fig. 3.7(b). It is seen that the FWHM decreases with increasing annealing temperature and attains a minimum of 28.9 cm^{-1} at 130°C, and beyond that the FWHM starts increasing. This clearly indicates that the maximum molecular ordering of P3HT in P3HT:PCBM is attained when the films are annealed to 130°C.

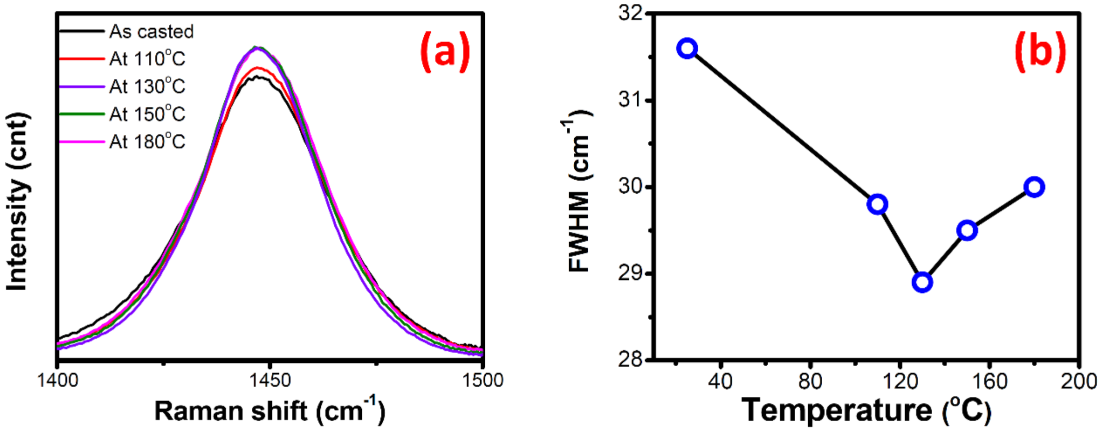

Figure 3.7: (a) Room temperature Raman spectra (in the range of symmetric C=C stretching mode) of P3HT:PCBM films recorded after annealing them at different temperatures. (b) Variation of corresponding FWHM's of symmetric C=C stretching mode as a function of annealing temperature.

In order to further confirm our data, we recorded UV/Vis spectra of the films annealed at different temperatures, which are shown in Fig. 3.8 and also provide a clue on the aggregation of PCBM and crystallization of P3HT. For as-deposited films, the peaks at 485 nm correspond to that of π-π* ($S_0 \rightarrow S_1$) transition of P3HT chains. On the other hand, 551 and 602 nm peaks are indicative of the inter-chain ordering and intra-chain ordering respectively. This may arise because of increase in conjugation within the polymer chains and the π-π stacking. Well-defined peaks for inter-chain ordering and intra-chain ordering in our as-cast films suggest that significant molecular ordering already exist in as-cast films as corroborated by Raman spectrum. In addition to P3HT peaks, a peak at 380 nm corresponding to the PCBM is also observed. As the films are annealed to temperatures ≥130°C, the π-π* transition peak exhibits a strong red-shift from 485 to 517 nm, which has been attributed to the crystallization of P3HT [40, 89]. Similarly, increase in relative intensity of 551 nm peak on annealing suggests that the inter-chain ordering of P3HT has improved [84]. In addition to this, the intensity peak of PCBM decreases at 180°C, which has been attributed to the aggregation of PCBM.

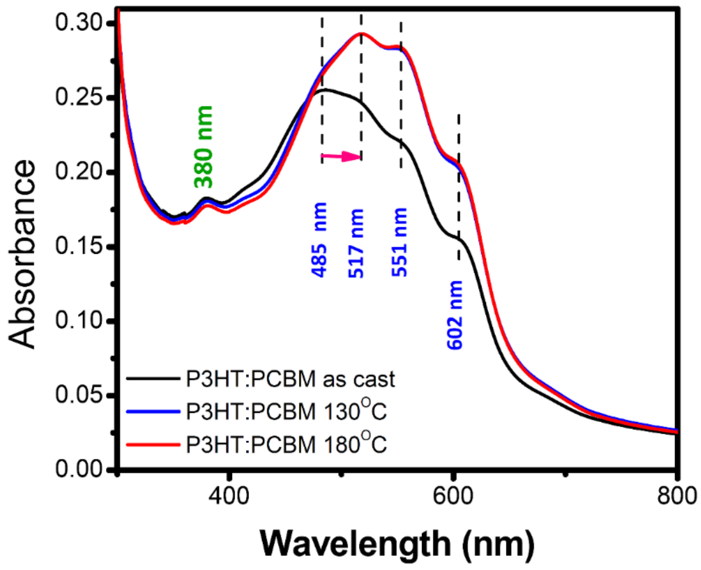

Figure 3.8: UV–Vis spectra of P3HT:PCBM films as-cast, and annealed at 130–180°C for 30min.

In order to further investigate the phase segregation in P3HT:PCBM films, we have carried out AFM and SEM studies on the films annealed at different temperatures. Typical AFM images of the bare ITO substrate, as-deposited P3HT:PCBM film, films annealed to different temperatures are shown in Fig. 3.9 (a-f). The AFM images were analyzed and the rms roughness was measured. The obtained results are plotted in Fig. 3.9(g). It is evident that the bare ITO substrate has an rms roughness of 3nm, whereas the as-deposited

P3HT:PCBM film has a reduced rms value of 0.5 nm, indicating a very high uniformity of the film. The film roughness increases marginally upto 1.3 nm after annealing at 130^{o}C. However for higher annealing temperature, the roughness increases rapidly, which is a consequence of phase segregation (as revealed by AFM image as well as by in-situ optical micrographs. The size of these aggregates is in the range of 2-5 μm with an average height of 250 nm. Similar images were reported in literature by scanning of near-field microscopy (SNOM) and AFM[90].

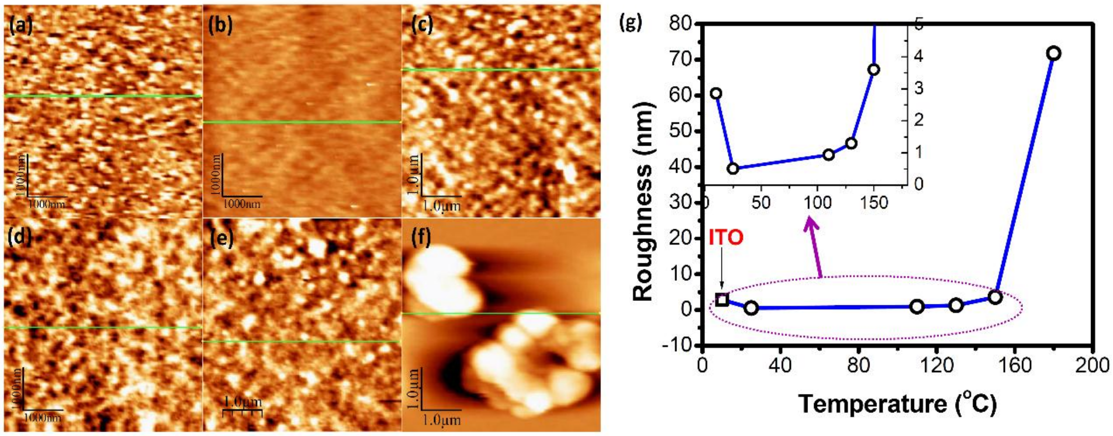

Figure 3.9: 5 µm × 5 µm AFM images of (a) bare ITO substrate, (b) as-cast P3HT:PCBM film, (c)–(f) are after annealing at 110, 130, 150 and 180°C, respectively. (g) RMS roughness of the films as a function of annealing temperature (inset shows the magnified version of the selective area).

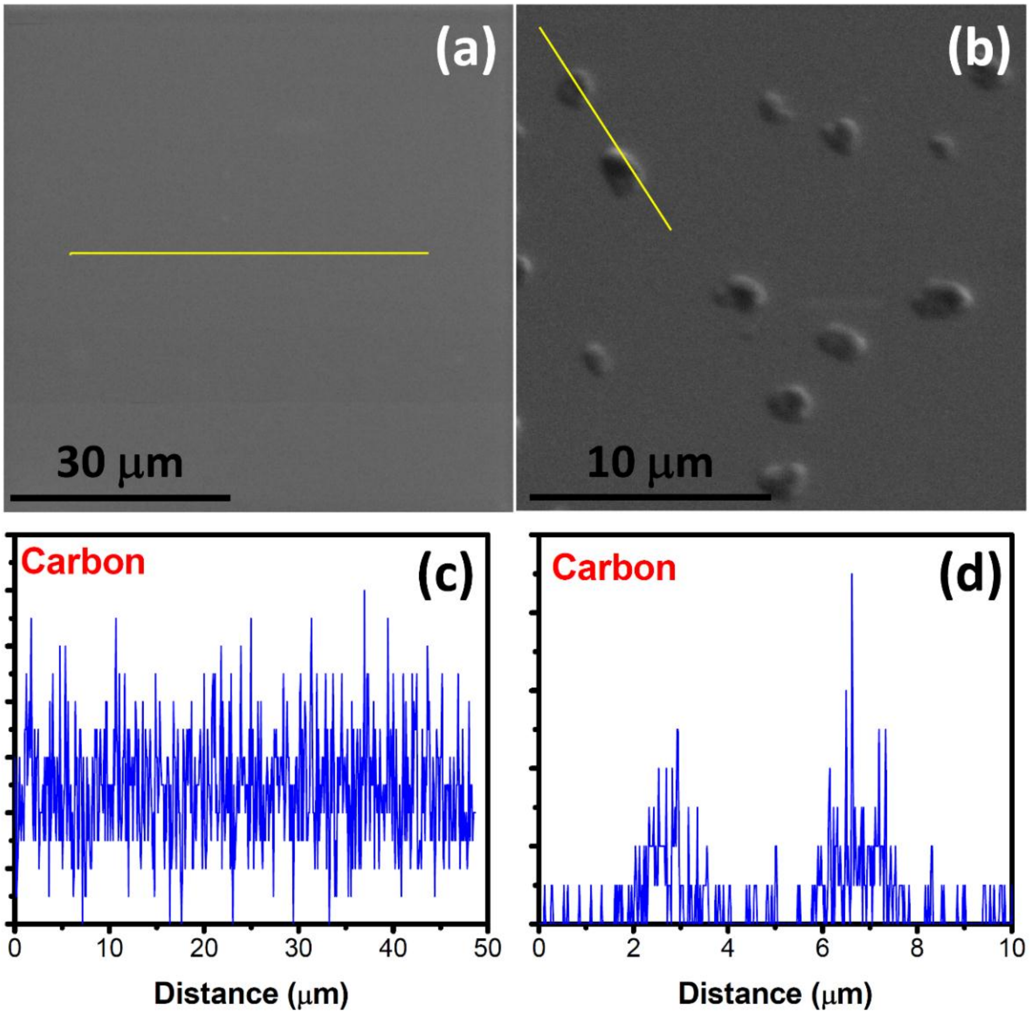

Figure 3.10: (a) and (b) are the SEM images of the P3HT:PCBM films annealed at 130 and180°C, respectively. (c) and (d) are the carbon X-ray counts across the lines drawn in (a) and (b) respectively.

In order to investigate the composition of the aggregates observed in the P3HT:PCBM films, we have carried out the carbon X-ray elemental imaging of the SEM micrographs for the films annealed at 130 and 180°C. The obtained results are shown in Fig. 3.10. The SEM image of the films annealed at 130°C is featureless and the carbon X-ray imaging is very uniform. This result indicates that the P3HT and PCBM are uniformly distributed. However, for films annealed at 180°C, the SEM image shows aggregates (in agreement with AFM image shown in Fig. 3.9). The line profile of carbon X-ray imaging across the two such aggregates indicates that they are rich in carbon, suggesting that the aggregates are composed of PCBM because the intense carbon counts are due to presence of C_{70}.

3.1.4 Correlation between morphology evolution and photovoltaic parameters

Based on the analyses of *in-situ* Raman spectra and optical imaging, *ex-situ* AFM, SEM and UV/Vis results, we envisage a schematic representation of the annealing induced morphological evolution of P3HT:PCBM films, as depicted in Fig. 3.11. In the as-deposited P3HT:PCBM films, both P3HT and PCBM have disordered structure and uniformly distributed across the film. As the temperature is increased to 130°C, P3HT undergoes molecular ordering (i.e. inter-chain and intra-chain ordering) without any phase segregation (i.e. PCBM remains uniformly distributed). Therefore, the Raman intensity corresponding to the PCBM molecules is very low in pristine as well as annealed (~130°C) films. However, as the annealing temperature is raised to 180°C, the segregation of PCBM molecules from the P3HT matrix takes place to form large PCBM aggregates of size 2-4 µm as reflected in our in-situ Raman spectroscopic and optical microscopic images. This induces the phase separation of PCBM from the P3HT matrix and thereby, restrict homogeneous P3HT:PCBM blend. Therefore, in homogeneous region more P3HT chains tend to crystallize (or order), resulting in stronger Raman signals for C=C peaks. The Raman signals, on the other hand, on PCBM aggregates are higher than those observed at the homogeneous part owing to linear relationship between Raman scattering and concentration of scatterers. This aggregation of the PCBM at the active layer surface may have significant effect on the photovoltaic properties.

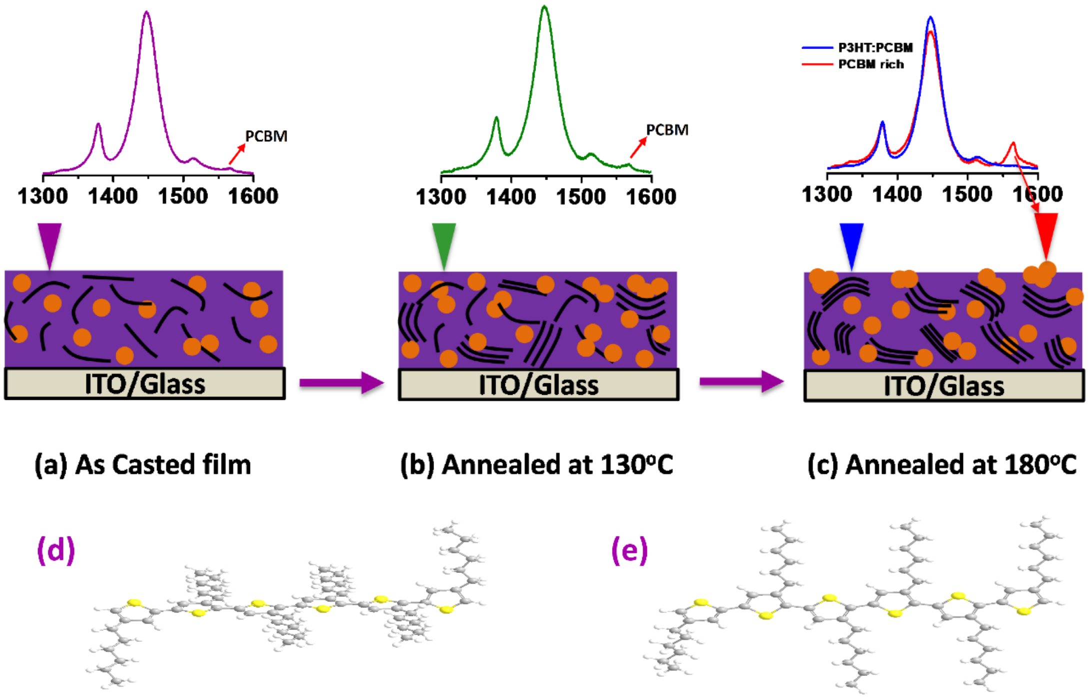

Figure 3.11: (a–c) Schematic depiction of morphology evolution in P3HT:PCBM films as a function of temperature. Typical selective area Raman spectrum in each case is also presented.

Now we discuss the correlation between the photovoltaic parameters (shown in Fig. 3.2) and the morphology of the films, shown in Fig. 3.11 (a-c), which were annealed at different temperatures. The value of V_{oc} (~0.5 V) almost remains independent of the annealing temperature upto 130°C. This is expected because V_{oc} is a measure of the difference between HOMO of donor and LUMO of acceptor, which is not very much affected by the annealing. However, a slight decrease in the V_{oc} is observed, when the annealing temperature is increased beyond 130°C. This is attributed to the significant segregation of PCBM at the sample surface as reflected in the *in-situ* Raman spectroscopy and optical microscopy. The J_{sc} and *FF* on the other hand, increases significantly upto an annealing temperature of 130°C, and then reduce for higher annealing temperature. As schematically presented in Fig. 3.11(d), in as-cast blend films, P3HT can have twisted polymer chains, which can cause a disorder, and as a result, a reduced J_{sc} and *FF*. When the blend films are cooled after annealing at 130°C, during cooling the P3HT chains can get planar, as shown in Fig 3.11(e), which can then induce molecular ordering via π-π stacking (i.e. H-aggregation), which is supported by a decrease in $I_{C=C}/I_{C-C}$ ratio in *in-situ* Raman data. This enhanced molecular ordering is responsible for maximum FF and J_{sc} owing to the reduced transport resistance within the blend film. However, when the temperature is increased beyond 130°C, a decrease in the J_{sc} and FF is observed. This decrease J_{sc} and FF is attributed to following facts:

(i) Increase in the annealing temperature higher than 130°C results in growth of molecular ordered P3HT domains which is bigger than the exciton diffusion length within the blend, as indicated by increase in the C=C Raman intensity and shown schematically in Fig. 3.11(c). This, in turn limits, the transport of free electrons and holes towards electrodes upon exciton dissociation

(ii) The PCBM molecules diffuse out of the blend towards sample-air surface, forming large aggregates, in agreement with increase in surface roughness deduced from AFM images, *in-situ* optical images as well as increased intensity of Raman $A_{1'}$ mode of PCBM. In spite of increased ordering of P3HT molecules beyond 130°C, the interfacial area between P3HT and PCBM in the blend films reduces significantly owing to the diffusion of PCBM molecules towards the sample-air surface. The reduced interfacial area in the blend films then results in the reduction of J_{sc}. The increased aggregation of the PCBM at the sample-air interface also damages the metal electrode as shown by Chirvase *et al*. [91] which leads to poor contact between the active layer (i.e. P3HT:PCBM blend) and the cathode, resulting in decrease in FF.

3.1.5 Correlation between materials parameters and device parameters

As discussed in the previous section the material properties, such as morphology, crystallinity etc. govern the efficiency of the device. Also, as seen from Table 3.1, the device parameters (n, I_0, R_s, R_{sh}, and I_{ph}) are intimately correlated with annealing temperature of the device. It was observed that the values of n, I_0, R_s, initially decreases with annealing temperature upto 130ºC and thereafter increases upon further increase in annealing temperature. On the other hand, I_{ph} increases upto 130ºC, which however decreases upon increasing the annealing temperature. The lowering of n, I_0, R_s values and increase in I_{ph} for device annealed at 130ºC can be attributed to the enhanced ordering or crystallinity of P3HT chains, leading to an improved charge transport. However, at lower and higher annealing temperatures these parameters deteriorate owing to the respectively poor ordering and formation of large PCBM aggregates.

Ideality factor of the device provides an indication on the overall quality of the device, as it describes how closely the *J*-*V* curve follows the theoretical model. Essentially, ideality factor provides an important information on the transport and recombination processes in solar cells. The value of n changes depending on the type of carrier recombination present in the device. A band-to-band or Schottky contact recombination gives $n = 1$ (close to the ideal diode), while $n = 2$ may attribute to Shockley-

Read-Hall (SRH) recombination traps, and an intermediate ideality factor (between 1 and 2) would attribute to the presence of a distribution of localized states (traps) [92]. Hence, the ideality factor may reflect more than one recombination mechanism, and the dominant mechanism may depend on the specific material and device condition. As shown in Table 3.1, n=1.55 has been obtained for the device annealed at 130ºC, whereas for all the other device higher n values have been obtained. As described earlier, device annealed at 130ºC has the best ordering/crystallinity among all the devices, and therefore, are expected to have minimum localized states, leading to minimum recombination. For all other devices, the localized states are higher due to the disorder in the system, and therefore, higher n values are obtained.

3.2 Porphyrin/polyfullerene diffuse bilayer solar cells

In this Section, we present the results on porphyrin/diffuse bilayer solar cells. As discussed in Chapter 1, in diffuse bilayer solar cells, the donor and acceptor layers interpenetrate. The diffused interface results in high interfacial area and improved charge transport, and therefore, are potential candidate for further investigation. The fabrication process of porphyrin-polyfullerene diffuse bilayer solar cells is described in Chapter 2, which is based on a sequential electrodeposition of porphyrin and polyfullerene films. Porphyrin-polyfullerene are selected because porphyrin is strongly light absorbing chromophores and fullerene has high electron affinity. Before we present the photovoltaic characteristics of diffuse bilayer solar cell, we discuss the results on the optimization of the electrodeposition of individual porphyrin and polyfullerene layers.

3.2.1 Electrodeposition of porphyrin films

As discussed in Section 2.2.2, the porphyrin films were deposited on ITO substrates by electrodeposition[93, 94]. Fig. 3.12 shows the typical cyclic voltammograms of first 5 scans recorded between 0 and 1 V at a scan rate of 50 mVs^{-1}. It is evident from the figure that porphyrin undergoes an electrochemical oxidation at a potential (E_{ox}) of ~0.4 V. This peak is irreversible, which indicates that the molecule is covalently grafted to the working ITO electrode. The intensity of this peak decreases monotonically and vanishes after 5 scans, indicating a complete coverage of the molecules onto ITO substrate.

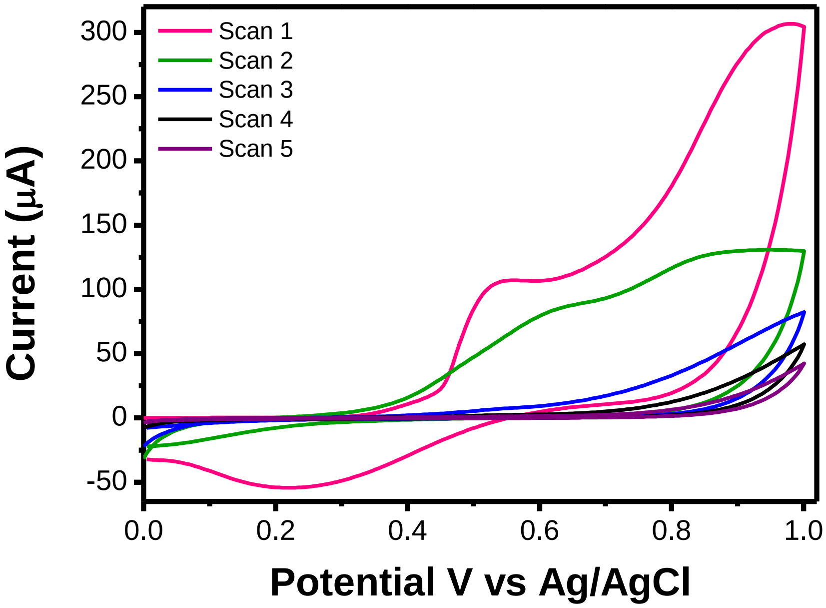

Figure 3.12: First 5 cyclic voltammograms of electrodeposition of porphyrin on ITO substrates.

Characterization of electrodeposited porphyrin films

Typical UV-Vis spectra of the electrodeposited porphyrin films on ITO substrates after different scans (recorded at scan rate 50 mV/s) are shown in Fig. 3.13 (a). In the inset, we show the absorption spectra of porphyrin monomer in methanol. The absorption spectrum of porphyrin monomer in methanol solution has a strong Soret band at 417 nm and four weak Q bands at 515, 553, 592, and 650 nm [95-97]. The absorption spectrum of the porphyrin films is shown in Fig. 3.13 (a), which is broader as compared to that of monomer in solution. This indicates that the porphyrin molecules do not decompose during electrodeposition. The Soret band is broadened and red-shifted from 417 nm (for porphyrin in methanol) to 432 nm (for the electrodeposited film), which is consistent with excitonic interactions between densely packed porphyrins owing to the J-type aggregation. This result suggests that electrodeposited porphyrin films are well packed. The absorbance of the Sorret band increases with increasing number of scans, which indicates that the thickness of the film is increasing. The typical thickness of the films after 10 and 75 scans measured using profilometer was respectively 20±3nm and 75±3nm.

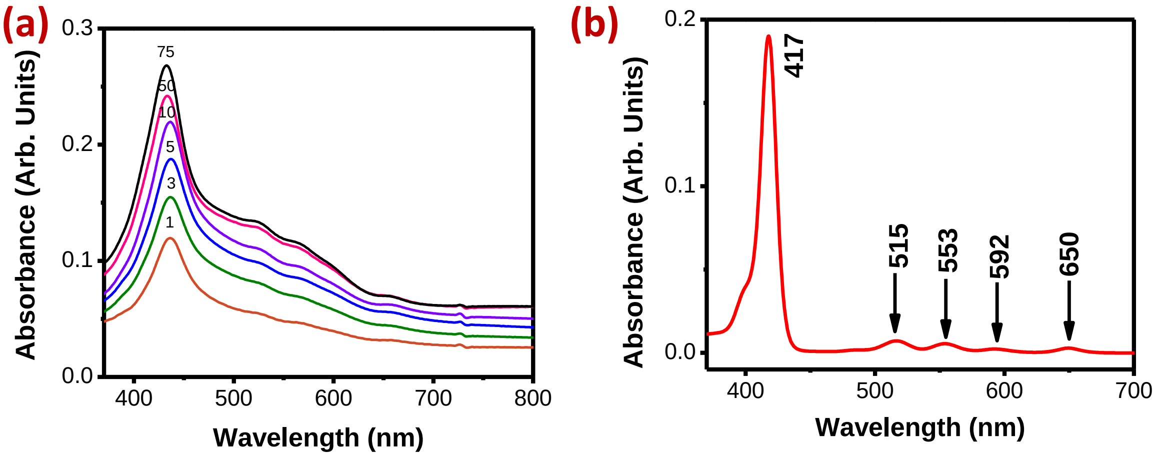

Figure 3.13: UV-Vis spectra of (a) porphyrin films deposited on ITO substrates after different number of scans and (b) porphyrin monomer in methanol.

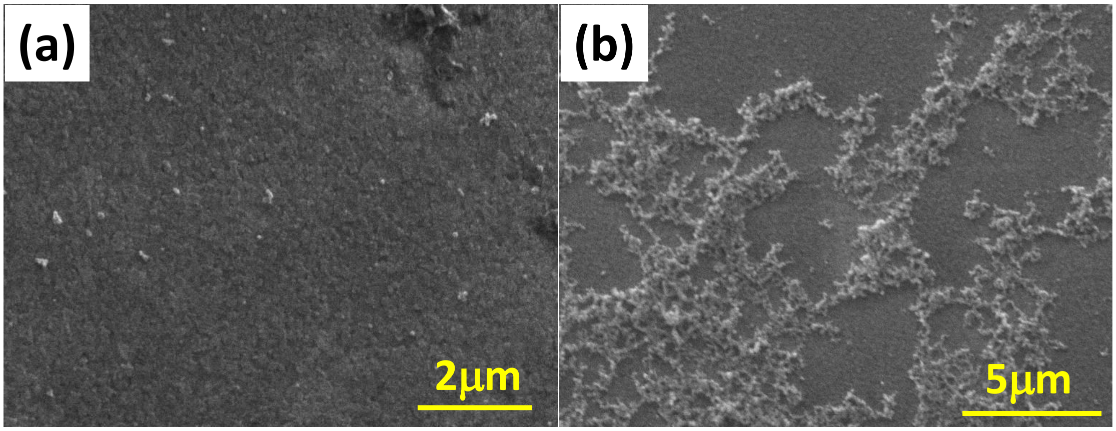

Figure 3.14: SEM images of electrodeposited porphyrin films after (a) 5 scans and (b) 10 scans.

The typical SEM images of the electrodeposited porphyrin films deposited for different number of scans are shown in Fig. 3.14. It is seen that upto 5 scans, a uniform porphyrin film is deposited onto the ITO substrate. However, at higher scans, the multilayers grow that has a random granular interpenetrated network, leading to a morphology similar to gyroid structure. Typical AFM image of porphyrin film electrodeposited for 5 scans is shown in Fig. 3.15. The height profile analysis show that the film has a rms roughness of ~7 nm for 2µm × 2µm area. The morphology consists of elongated grains, which is consistent with UV/Vis data that porphyrin molecules arrange in the form of J-aggregate. This type of morphology is appropriate for the fabrication of diffuse bilayer solar cells.

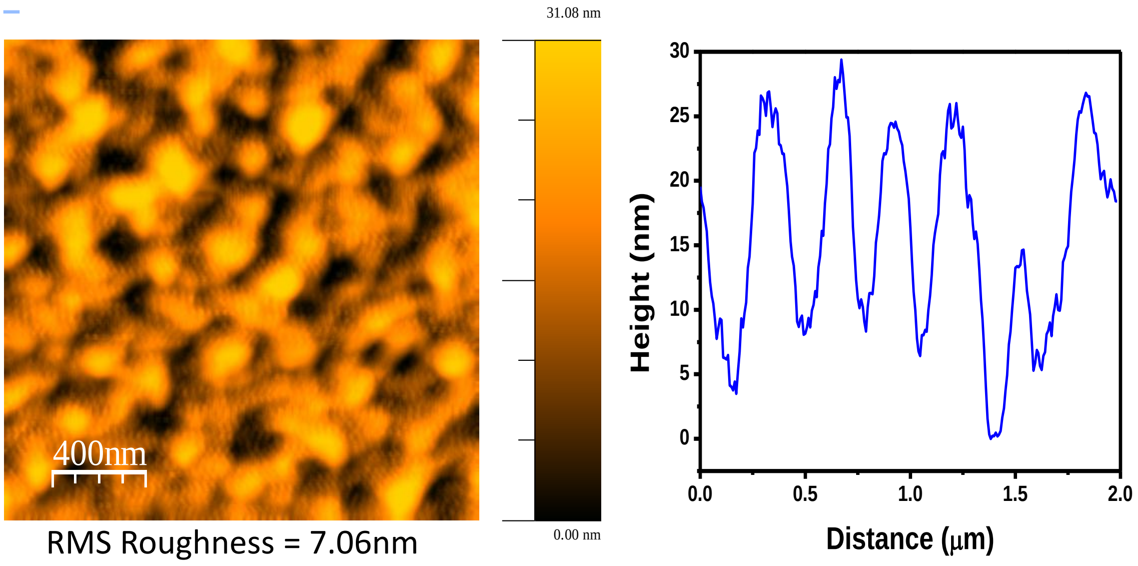

Figure 3.15: AFM image of porphyrin film deposited for 3 CV scans, a height profile showing formation of granular morphology.

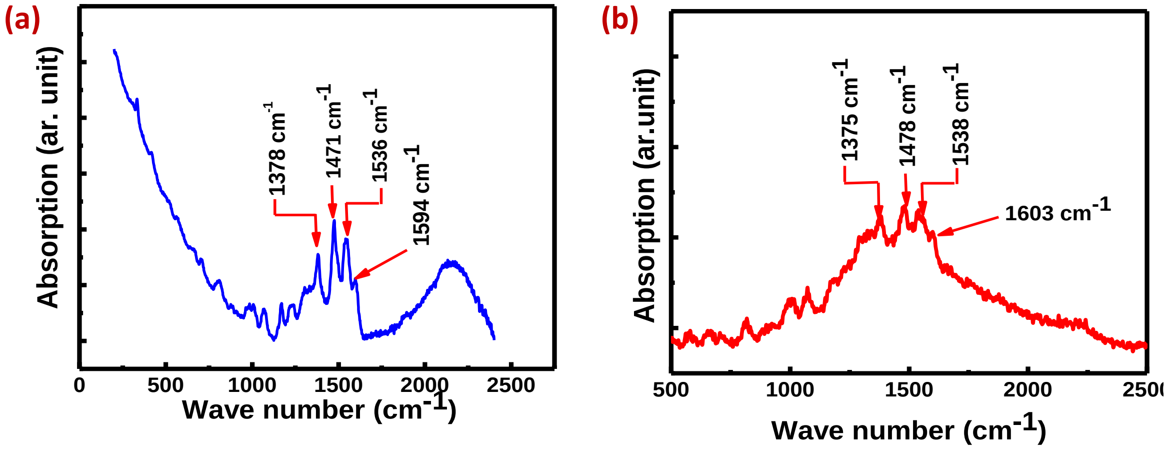

Figure 3.16: The Raman spectra of (a) electrodeposited porphyrin film and (b) drop-casted porphyrin film.

The Raman spectrum of an electrodeposited porphyrin film is shown in Fig. 3.16(a). For comparison the Raman spectrum of the drop-casted film of porphyrin monomer is shown in Fig. 3.16(b). It is seen that the characteristics bands at 1375 cm^{-1}, 1477 cm^{-1}, 1536 cm^{-1}, 1603 cm^{-1} of porphyrin film are similar to that observed for the drop-cast porphyrin film i.e. 1378 cm^{-1}, 1471 cm^{-1}, 1538 cm^{-1}, 1594 cm^{-1}[97]. The shifts in the electrodeposited films can be attributed to the J-aggregation of porphyrin molecules.

3.2.2 Electrodeposition of polyfullerene films

As discussed in Chapter 2, the polyfullerene films were deposited onto ITO in two steps: (i) preparation of C_{60}^{2-} solution in dichloromethane (DCM) by electroreduction method, and (ii) electrodeposition of polyfullerene films on ITO by oxidation of C_{60}^{2-}using linear sweep voltammetry (LSV)[98].

First we describe the method for the preparation of a homogeneous C_{60}^{2-} solution by electroreduction process. It may be noted that the electrochemistry of C_{60} normally exhibits three to six chemically-reversible one-electron reductions corresponding to the $C_{60}^{0/1-}$, $C_{60}^{1-/2-}$, $C_{60}^{2-/3-}$, $C_{60}^{3-/4-}$, $C_{60}^{4-/5-}$, and $C_{60}^{5-/6-}$ couples in which the three-fold degenerate lowest unoccupied molecular orbital (LUMO) of C_{60} is populated[99-101]. By contrast, the oxidation of C_{60} is generally irreversible in most solvents, which is attributed to the C_{60}/solvent interactions i.e. hydrogen bonding and electrostatic interactions[102]. Experimental and theoretical studies show that among various C_{60} species, C_{60}^{2-} is most stable, and therefore, has widely been used in different reactions[100]. Fig. 3.17(a) shows the CV recorded for C_{60} in DCM and TBAP as electrolyte and Pt foil as working electrode. The CV exhibits two reduction peaks at −0.66 and −1.14 V, corresponding to C_{60}^{-} and C_{60}^{2-}, respectively. Similar to the reported literature[102], we do not find the oxidation peaks possibly due to the C_{60}/DCM or TBAP interactions. However, some fraction of oxidized C_{60}^{1-} and C_{60} are inevitable. Therefore, in order to obtain a solution of C_{60}^{2-}, a potential of −1.5 V was applied until the violet colour (characteristic of C_{60} solution) turned into light brown colour (characteristic of dianion C_{60} solution[103]), as shown in the inset of Fig. 3.17(b). The UV-Vis spectra of C_{60} solution recorded before and after electroreduction processes are shown in Fig. 3.17(b). Presence of a characteristics peak at 975 nm confirms the formation of C_{60}^{2-} after electroreduction[104]. It was found that the C_{60}^{2-} solution remains stable for several hours under inert atmosphere. Once a C_{60}^{2-} solution in DCM is formed, which also consists of TBAP electrolyte, the Pt foil working electrode was replaced by ITO substrate.

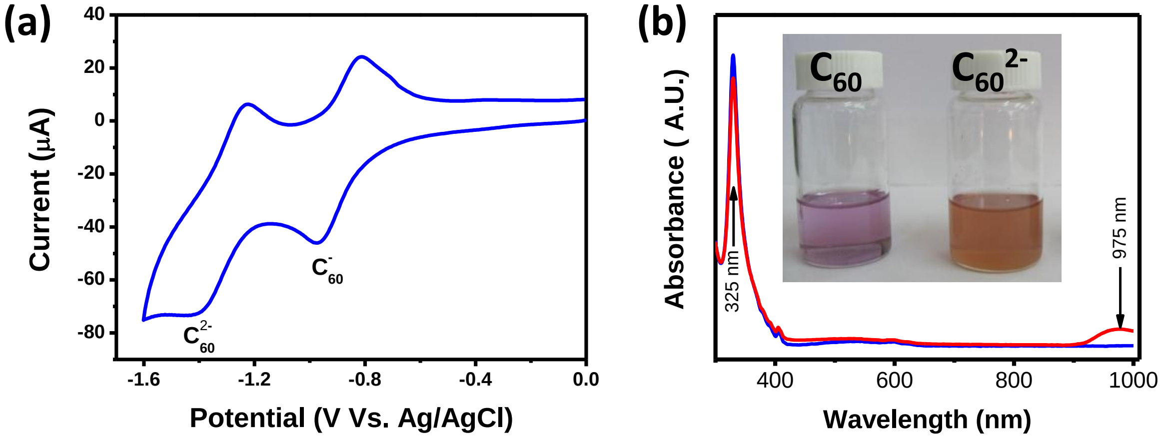

Figure 3.17: (a) Cyclic voltammogram recorded for C_{60} solution prepared in DCM and TBAP as a supporting electrolyte. (b) UV-Vis spectra recorded for C_{60} and C_{60}^{2-} solutions. Inset shows photographs of C_{60} (violet) and C_{60}^{2-} (light brown) solutions.

The electrodeposition of C_{60} on ITO was carried out by oxidizing C_{60}^{2-} in two modes: (i) by applying a constant potential and (ii) by linear sweeping of potential from −1 to 0 V. The first mode did not yield good films, whereas LSV resulted in uniform C_{60} films. Typical LSV curves recorded for different number of scans are shown in the Fig. 3.18(a). In these curves, two peaks at −0.65 (I) and −0.83 (II) are identified. The peak I is identified as the first oxidation peak i.e. conversion of C_{60}^{2-} into C_{60}^{-}, whereas the peak II corresponds to second one electron oxidation i.e. conversion of C_{60}^{-} into neutral C_{60}. As the numbers of LSV scans were increased, an increasing film thickness was visibly observed. The mechanism underlying the growth of C_{60} films on ITO is not very clear. However, as we demonstrate latter that the HRTEM images show formation of a series of 1-dimensional (1D) “pearl-chain” structures, indicating the presence of covalent cross-linking bonds. This prompted speculation that polymerization had occurred between C_{60} molecules via [2+2] cycloaddition reaction, as schematically shown in Fig. 3.18(b). Since the current studies were carried out under inert atmosphere, therefore oxygen anion induced polymerization, as reported in the literature[105], is ruled out. In the present case, oxidation of C_{60}^{2-} takes place at ITO substrate, leading to the formation of C_{60}^{-} and neutral C_{60}. It is therefore anticipated that C_{60}^{-} ions induce [2+2] cycloaddition re-actions at room temperature, leading to the formation of dimers and 1D polymer chain. Such cycloaddition reaction between neutral C_{60} and C_{60}^{-1} has previously been reported for polymerized LiC_{60} film[106]. The mechanism proposed above also explains why good films are not obtained under the constant potential mode. This is because under this mode, it is not possible to obtain both C_{60} and C_{60}^{-1} species required for the cycloaddition reaction.

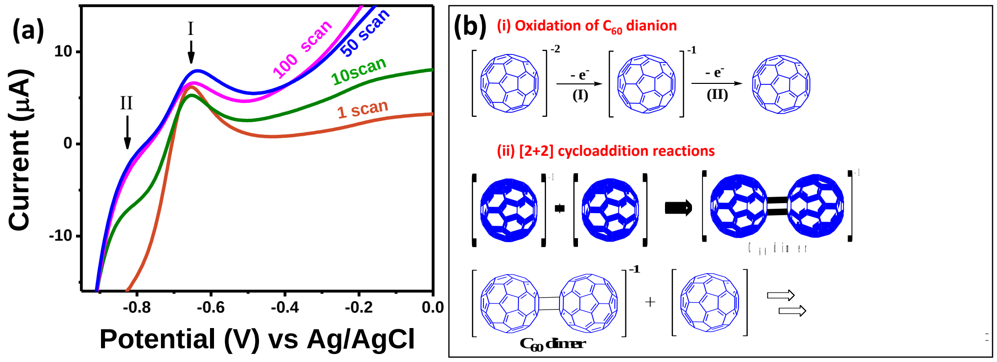

Figure 3.18: (a) Typical linear sweep voltammograms (LSV) recorded using ITO as working electrode and C_{60}^{2-}+ TBAP solution after different numbers of scans. Peaks (I) and (II) correspond to C_{60}^{2-} to C_{60}^{-} and C_{60}^{-} to C_{60} oxidations, respectively, which occur at ITO surface. (b) Schematic of the proposed pathways of polymerization of C_{60}.

Characterization of poly-fullerene films

First we confirm the formation of polyfullerene films on ITO substrates using the results of electrochemical characterization, FTIR and UV/Vis measurements. A unique advantage of electrochemical process is that it can be used for the film deposition as well as its characterization. Typical cyclic voltammetry curve, which was recorded using "films deposited on ITO" (deposited for 200 LSV scans) as working-electrode and pure TBAP as electrolyte, is shown in Fig. 3.19(a). It is apparent that the film undergoes a reduction at −0.55 V, which is slightly lower than that of C_{60} monomer in the solution (see Fig. 3.19(a)). This characteristics reduction peak indicates presence of polymerized C_{60} in the films. Fig. 3.19(b) shows the FTIR spectra recorded for the polyfullerene films deposited for 200 LSV scans. Presence of peaks at 527, 548, 554, 576, 606, 721, 753, 1091, 1122, 1171, 1287, 1336 and 1423 cm^{-1} confirms the presence of polymeric C_{60} [107, 108]. The four IR modes observed for C_{60} monomer at 527, 576, 1182, 1429 cm^{-1} are also observed in the films. However, these peaks were found to be quite broad and their relative intensities were quite different, indicating that vibrational modes found in C_{60} are also active in polyfullerene and that there are different degrees of shifts in the IR peaks upon the cycloaddition of C_{60} cages. The polyfullerene films have many more IR-active modes than C_{60}, which is attributed to the lowering of molecular symmetry upon the polymerization of C_{60}[109].

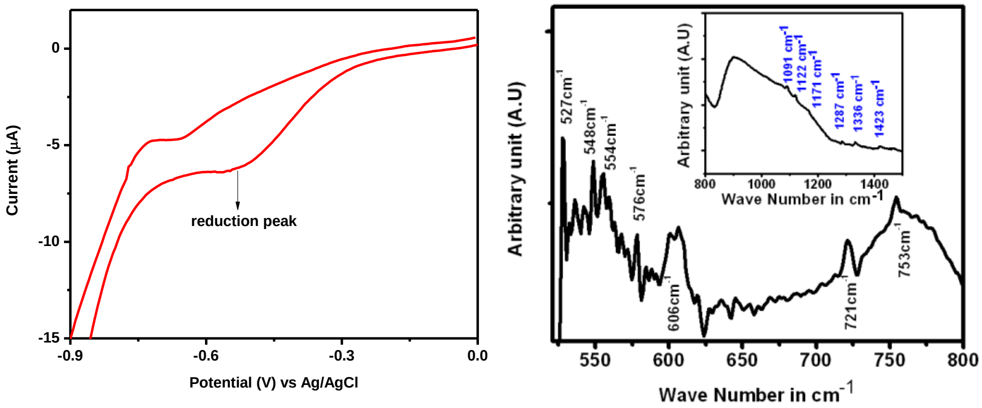

Figure 3.19: (a) Cyclic voltammogram recorded using electrodeposited polyfullerene film as working electrode and 0.1 M TBAP as electrolyte. (b) Typical FTIR spectrum of polyfullerene film in the wavenumber range 500 – 800 cm^{-1}. Inset shows the FTIR spectrum in the range 800–1500 cm^{-1}.

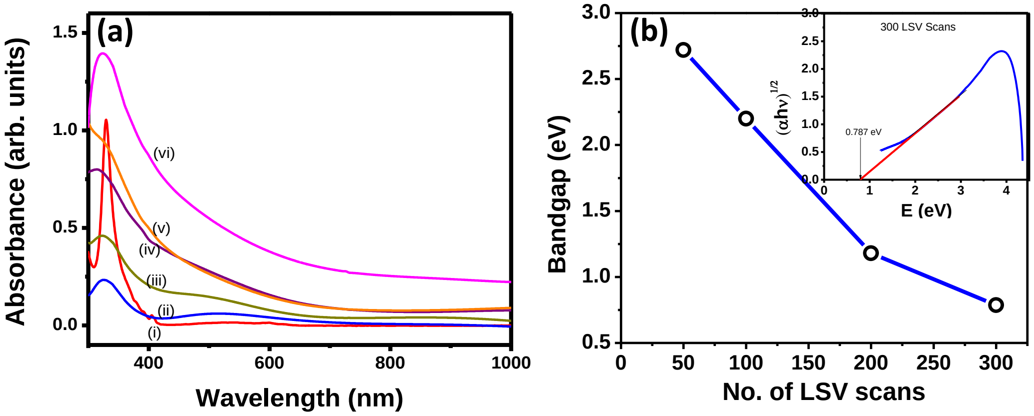

Figure 3.20: (a) Typical UV-Vis spectra recorded for C60 solution (i) and electrodeposited polyfullerene films on ITO after different numbers of LSV scans: (ii) 50, (iii) 100, (iv) 150, (v) 200 and (vi) 300. (b) Energy band gap of polyfullerene films as a function on numbers of LSV scans used for deposition. Inset shows a typical Tauc plot used for determination of band gap.

The UV/Vis spectra recorded for films deposited using different numbers of LSV scans are shown in Fig. 3.20(a). It is seen that for C_{60} solution (prepared in DCM) a sharp absorption peak is observed at 329 nm. However, this peak broadens for polyfullerene films deposited using increasing numbers of LSV scan. In polyfullerene, C_{60} loses it symmetry and consequently degeneracy of energy levels is lifted up, resulting in broadening of the absorption peak[104]. Fig. 3.20(b) shows the optical energy band gap of the films plotted against the number of LSV scans used for their preparation. The energy gap values were deduced as the energy ($h\nu$)-axis intersections of the linear extrapolations of $(\alpha h\nu)^{1/2}$ versus $h\nu$ plots, known as Tauc plot. A typical Tauc plot for polyfullerene film electrodeposited for 300 LSV scans is shown in the inset of Fig. 3.20(b). The value of band gap for films prepared using 50 LSV scans is 2.6 eV, which is similar to that evaluated for vacuum evaporated C_{60} films as well as the values determined for C_{60} single crystals using photoemission and inverse photoemission experiments[110]. The value of band gap monotonically reduced for the films prepared using increased numbers of LSV scans, and a value of 1.78 eV was deduced for the film prepared using 300 scans, indicating polymerization of C_{60} leading to long polyfullerene chains.

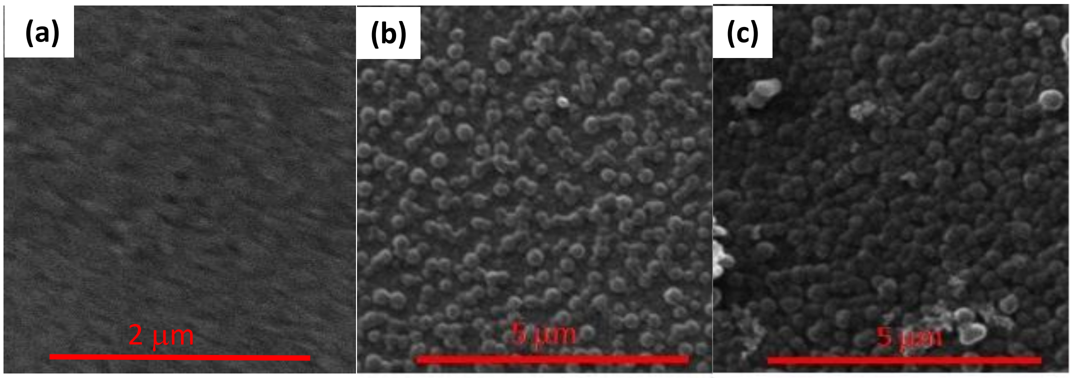

Figure 3.21: SEM images of bare ITO surface (a), and polyfullerene films deposited after 50 (b) and 100 (c) LSV scans.

Finally, we discuss morphology evolution of the polyfullerene films as a function of number of LSV scans. Fig. 3.21 shows typical SEM images of the bare ITO-coated glass substrates, (see Fig. 3.21(a)) and electrodeposited polyfullerene films after different numbers of LSV scans (Figs. 3.21(b) and 3.21(c)). It is evident that as polyfullerene grows on ITO in the form of globular islands. As the numbers of LSV scans are increased, the size as well as density of polyfullerene globular increases and a dense polyfullerene film covering entire ITO substrate is formed after 100 LSV scans. This has been independently confirmed by AFM images, as shown in Fig. 3.22. The analysis of the height profile of the AFM image show that the polyfullerene grain size is ∼0.3 µm dia., whereas the average surface roughness is only ∼56 nm. A very small surface roughness and absence of pinholes confirm deposition of uniform high-quality films. Further confirmation on the uniformity of the films was obtained by Kelvin probe microscopy. The scanning work function plots for bare ITO and polyfullerene films (deposited for 50, 100, and 200 LSV scans), measured in the area of 15 mm × 15 mm, are shown in Fig. 3.23. The 2D work function of ITO has been modified from 5.01 eV to 4.7 eV after deposition of polyfullerene. The 2D work function plots measured for polyfullerene films deposited at various scans 50, 100, and 200 LSV scan show ~ 4.78 eV, indicating a uniform film deposited on ITO substrates. In addition, it was confirmed again by measuring the work function at the interface of the ITO and polyfullerene films (as shown in Fig. 3.24). A clear distinction of work functions from 5.1 eV to 4.7 eV is clearly observed. Also, a 3D work function plot of an interface is shown in Fig. 3.24(b) for reference. In literature, the work function for polymerized C_{60} has been measured using ultra-violet photoelectron spectroscopy and was found to be 4.7 eV[111]. Therefore, the average work function of 4.76 eV measured using Kelvin probe microscopy is in agreement with literature value.

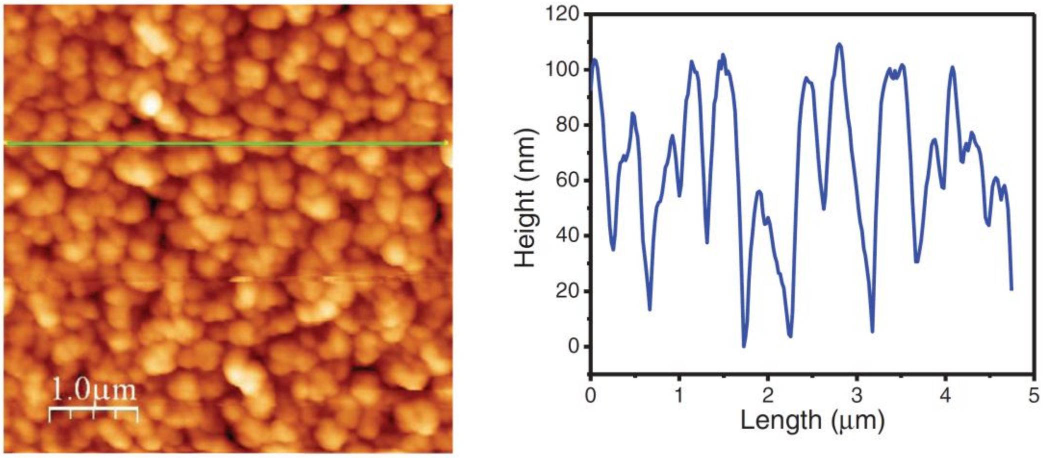

Figure 3.22: AFM image of polyfullerene films deposited after 100 LSV scans.

Interestingly, as shown in Fig. 3.25, as the numbers of LSV scans are further increased, formation of second polyfullerene layer on top of the first layer was found to grow. However, the second layer grows in the form of small chains, which possibly occurs due to the fusion of C_{60} globules; see Fig. 3.25). These small chains grow in the form of long whiskers with increasing numbers of LSV scans. At 300 LSV scans, a network of polyfullerene whiskers was found to grow, see Fig. 3.25(b). The length and diameter of these whiskers were found to be in the ranges of 100–200 µm and 0.1–0.4 µm, respectively. The magnified SEM images shown in Fig. 3.25(c), clearly indicate that the whiskers are continuous and formed due to the fusion of C_{60} globules. These whiskers could be easily transferred (by mechanically scrubbing) onto the carbon grid for HRTEM measurements.

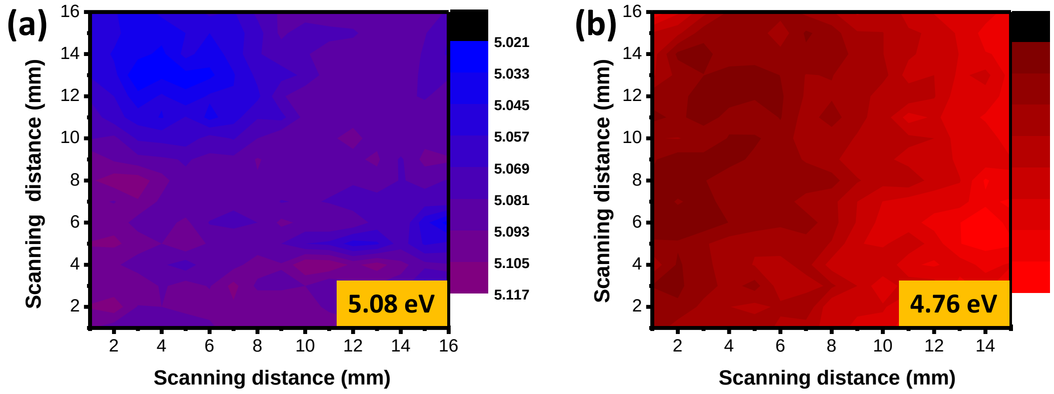

Figure 3.23: Workfunction mappings of (a) ITO substrate; (b) electrodeposited polyfullerene on ITO substrates for 200 LSV scans.

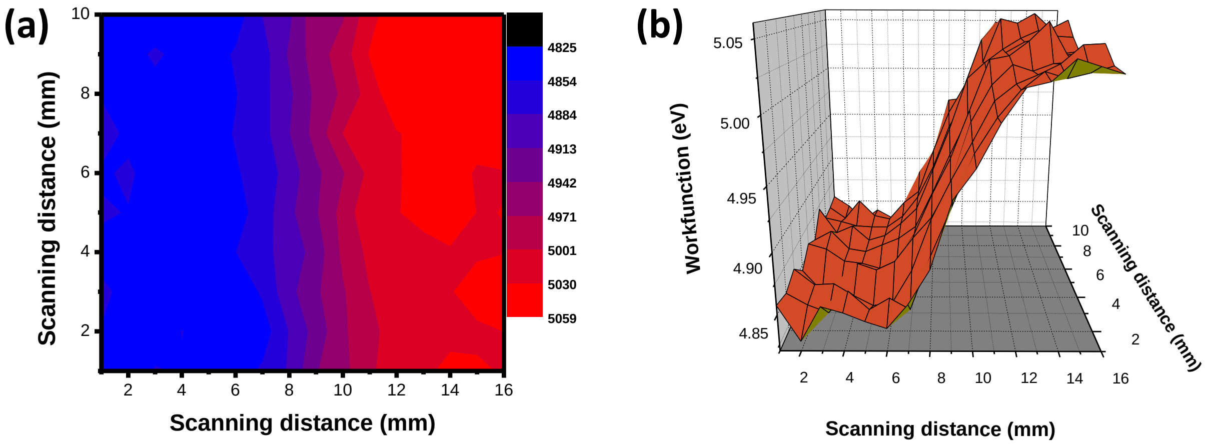

Figure 3.24: (a) Work function mapping of ITO-C_{60} interface (Blue indicates C_{60} region, Red indicates ITO region); (b) 3D work function mapping of ITO-C_{60} interface

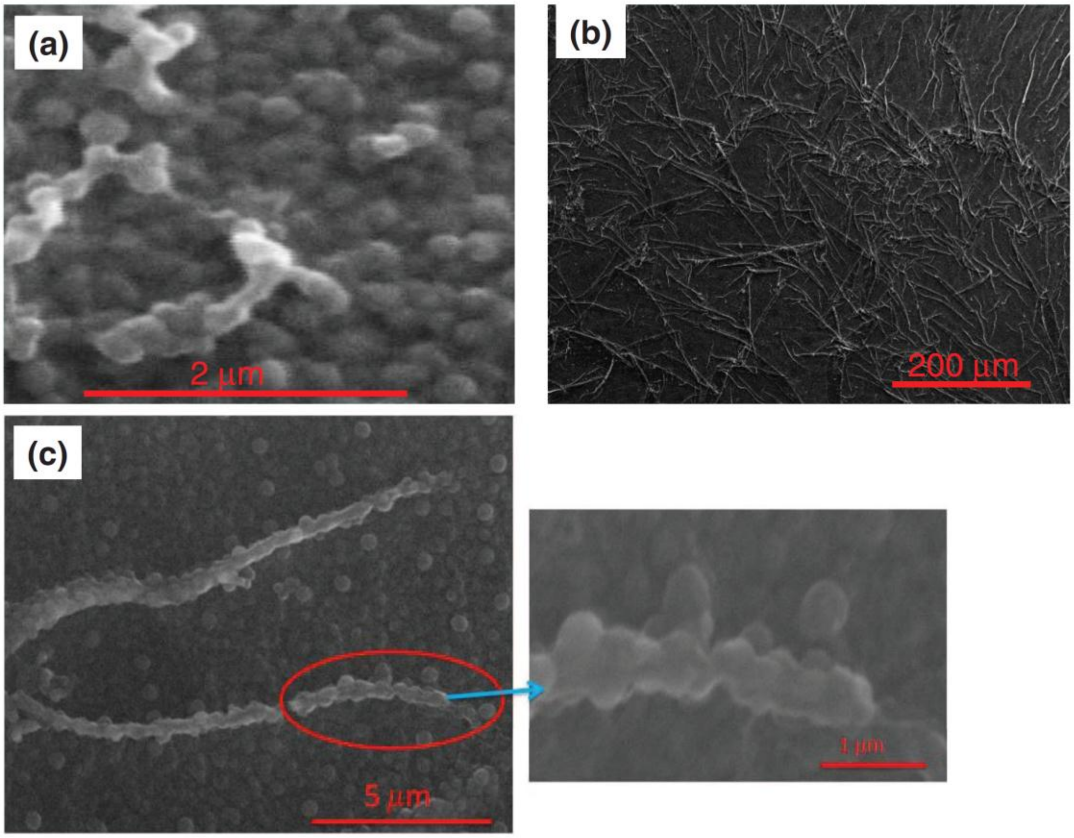

Figure 3.25: SEM images of (a) polyfullerene films deposited on ITO substrate for (a) 200 LSV scans, (b) 300 LSV scans, and (c) magnified view of single polyfullerene nano whisker.

A typical HRTEM image of the polyfullerene whisker, isolated from substrate is shown in Fig. 3.26. It may be noted that identical images were obtained for the first polyfullerene layer, indicating that the nucleation and growth mechanism is identical for first and subsequent layers. It is evident that C_{60} are polymerized in the 1-dimensional “pearl-structure,” which confirms our preposition that polymerization is based on [2+2] cycloaddition mechanism. The C_{60}–C_{60} periodicity along the chain is found to be 1.02 nm, whereas the inter-chain distance was found to be around 0.87 nm. In literature, the theoretical calculations based on total-energy pseudo-potential density functional theory showed that a fully polymerized C_{60} chain is more stable than nonpolymerized C_{60} [112].

Assuming [2+2] cycloaddition as the preferred linking mechanism, in the equilibrium structure of the polymer chain the center to-center distance between two adjacent molecules was predicted to in the range of 0.97–0.84 and the structure is expected to be a cylindrically symmetrical ellipsoid with eccentricity 0.933. The reduction in the number of double bonds following [2+2] cycloaddition reduces the strain energy in the C_{60} structure, allowing molecules to elongate in directions parallel to the new cross-links. However, the lateral bonding between individual 1D pearl-chain is assumed to be through Van der Waals interactions, as no indication of chemical bonding was observed in other directions. It may be noted that there are few reports in literature on the assembly of 1D molecular chains of C_{60} with long-range ordering[113]. However, they were fabricated using α-sexithiophene (6T) monolayer nanostripes on Ag (111) surface. Highly ordered arrays of 1D molecular systems represent prototypes for 2D or 1D quantum confinement of surface electronic states and are of technological importance in the realization of molecular nanodevices[114].

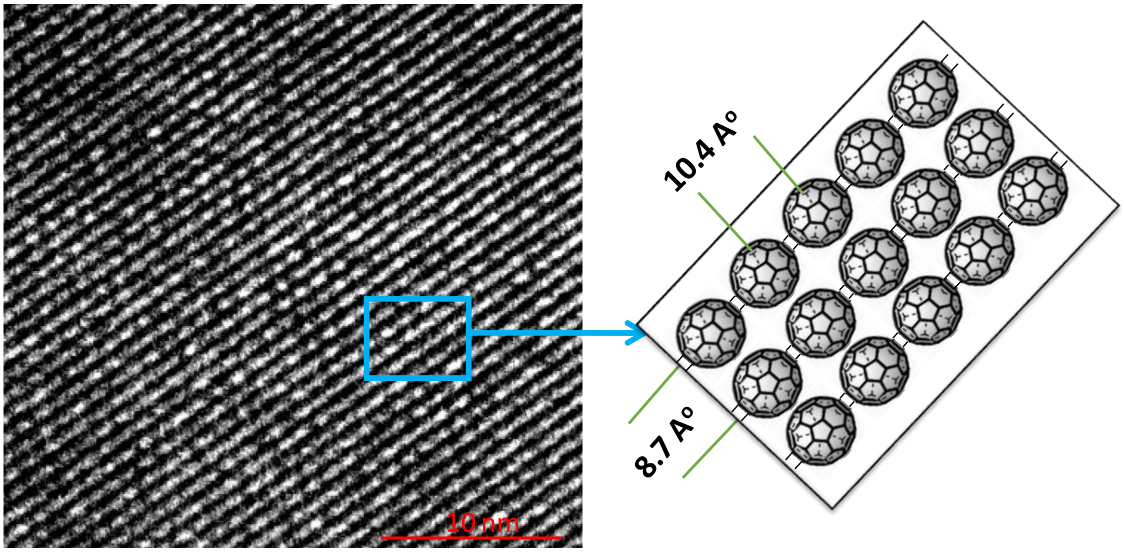

Figure 3.26: HREM micrographs of C_{60} on ITO (300 scan) showing avg. roughness of 30nm, The C_{60} – C_{60} periodicity along the chain is 10A^{o}-11A^{o} and the interchain distance observed is around 8 A^{o} – 9A^{o}.

3.2.3 Photovoltaic characteristics of porphyrin/polyfullerene diffuse bilayer solar cells

The energy level diagram of the bilayer device ITO/PEDOT:PSS/porphyrin/polyfullerene/Al is shown in Fig. 3.27(a). Theoretically a maximum V_{oc} of ~1.5V can be generated using this device. The energetics of porphyrin and polyfullerene clearly indicates a facile charge transport of photogenerated carriers through donor and acceptor materials towards respective electrodes. The fabrication process of such a bilayer solar cells is described in Section 2.2.2, for which first a porphyrin layer was electrodeposited onto PEDOT:PSS coated ITO substrate and followed by electrodeposition of poly-fullerene layer.

The UV-Vis spectra of porphyrin/polyfullerene bilayer films are shown in Fig. 3.27(b), which is typically superimposition of porphyrin (431nm) and polyfullerene (325nm) individual films. The results show that in the bilayer heterojunction porphyrin and polyfullerene do not react.

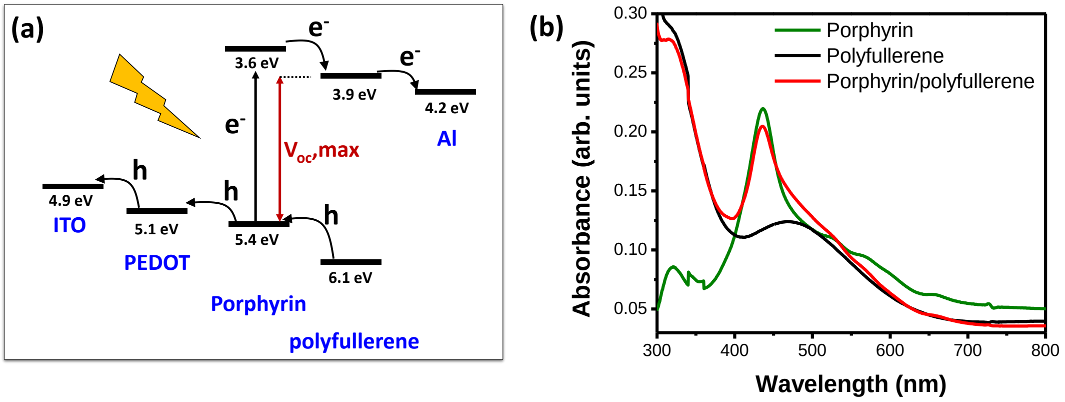

Figure 3.27: (a) Energy level diagram of porphyrin-polyfullerene bilayer solar cell, (b) UV-Vis spectra showing absorbance of porphyrin, polyfullerene, and porphyrin/polyfullerene bilayer.

For photovoltaic characterization, several bilayer devices were fabricated by varying the thicknesses of porphyrin and polyfullerene films. The devices fabricated using thicknesses <25 nm were found to be short-circuited, possibly due to the penetration of top Al electrode. On the other hand, devices fabricated using thicker (>100 nm) porphyrin and/or polyfullerene layer didn't show any photoresponse characteristics, which is attributed to poor charge collection properties as the generated charge carriers may get recombine before reaching to the respective electrodes.

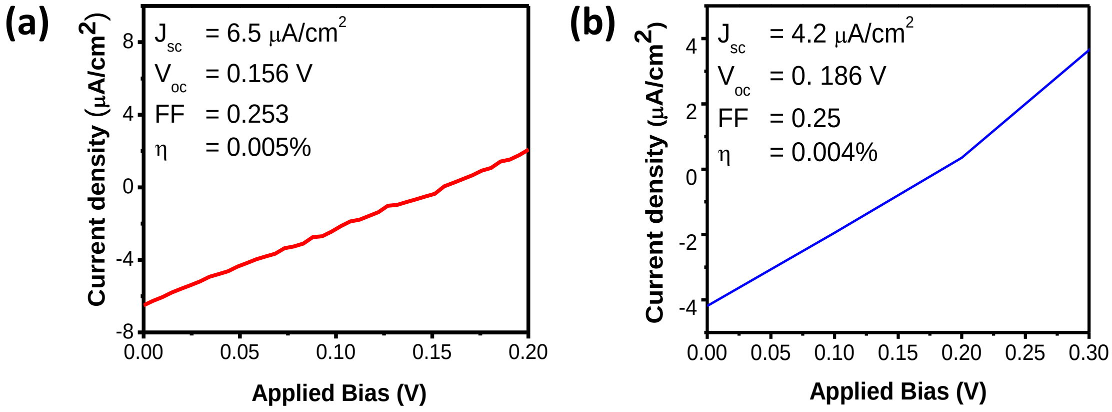

Figure 3.28: *J-V* characteristics of (a) porphyrin/fullerene bilayer solar and (b) porphyrin/PCBM bilayer solar cells under 5 mW/cm^2 white light illumination.

Table 3.2: Solar cell parameters evaluated from current-voltage characteristics presented in Fig. 3.28.

Device	J_{sc} (μA/cm^2)	V_{oc} (V)	*FF* (%)	*η* (%)	*n*	R_s (kΩ–cm^2)	R_{sh} (kΩ–cm^2)	I_0 (nA/cm^2)	I_{ph} (μA/cm^2)
Porphyrin/fullerene	6.5	0.15	0.25	0.005	>3.5	>15	>15	>5000	>10
Porphyrin/PCBM	4.2	0.18	0.25	0.004	>3.5	>15	>15	>5000	>10

Typical *J-V* characteristic of diffuse bilayer solar cells fabricated using porphyrin and polyfullerene layer thickness of ~50 nm each is shown in Fig. 3.28 (a). For comparison, *J-V* characteristic of bilayer solar cells fabricated by spin-coating PCBM solution on electrodeposited porphyrin is shown in Fig. 3.28(b). The diffuse bilayer devices with polyfullerene and PCBM exhibits similar device characteristics, the photovoltaic parameters are shown in Table 3.2. The device exhibited J_{sc} of 2-7 $\mu A/cm^2$ and V_{oc} of ~180-200 mV with power conversion efficiency ~0.002-0.005% under white light illumination of 5 mW/cm^2. The V_{oc} of these solar cell is quite low as compared to the theoretical value of 1.5 V. Despite of low efficiency, our results are quite encouraging from the view point that they are fabricated for the first time. However, there is a good future scope of improving V_{oc} as well as $J_{sc,}$ which can be achieved by an optimization of various device parameters i.e. thicknesses of porphyrin and polyfullerene layers, morphology of the layers by appropriate post annealing, etc. The fitting of *J-V* characteristics using equation 1.6 was not very good, as the device exhibited very high series and shunt resistances, high dark saturation currents, and very low photogenerated currents. The various estimated device parameters are summarized in Table 3.2. Very high value of n (>3.5) indicates that the device consists of high disorder. This is expected as, unlike P3HT, porphyrin does not crystallize. In the absence of large range ordering of porphyrin, the disorder act as traps for the charge carriers and as a result the recombination increases. This leads to overall poor efficiency of the device.

3.3 Porphyrin-modified ZnO-nanowire/ P3HT hybrid solar cells

In hybrid solar cells, the fullerene acceptors are replaced by the inorganic semiconductor nanostructures, such as ZnO nanoparticles (NP), nanowires (NW) etc., as discussed in Chapter 1. Here we describe the results on porphyrin-modified ZnO-nanowire/ P3HT hybrid solar cells. The fabrication of these solar cell is described in Section 2.2).

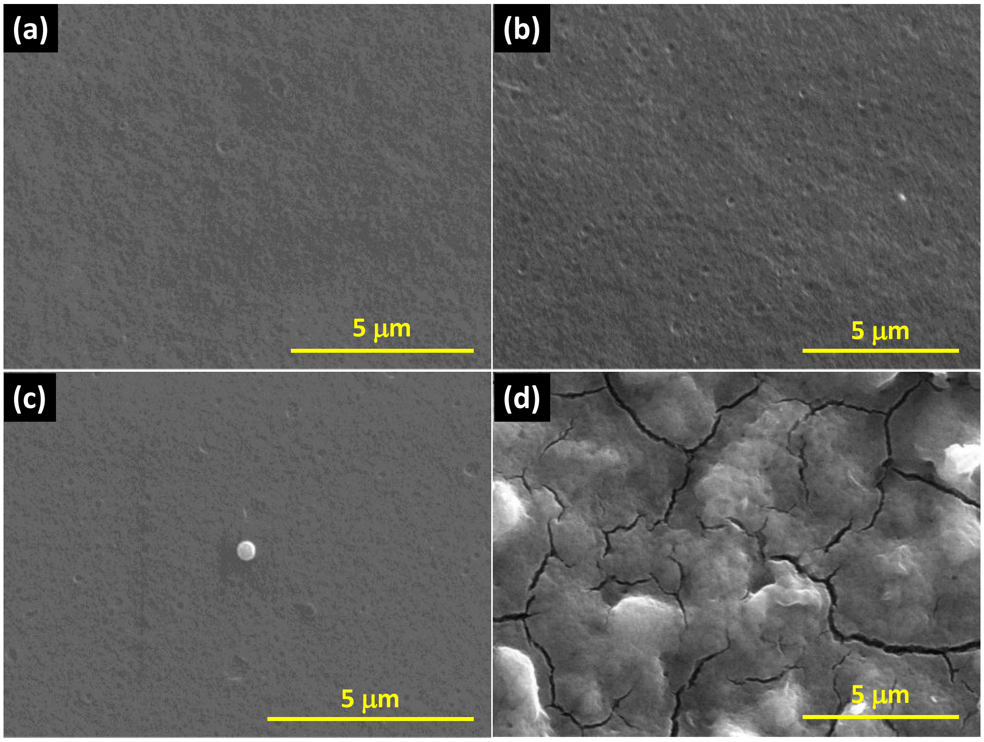

Figure 3.29: SEM Images of ZnO seed layer deposited on ITO substrate by using (a) 5 μl, (b) 10 μl, (c) 15 μl, and (d) 20 μl of ZnO NP solution.

3.3.1 Porphyrin-modified ZnO-nanowire

The growth of vertically aligned one dimensional (1D) ZnO NWs onto ITO substrates is described in Section 2.3.2. Figure 3.29 shows the SEM images of the ZnO NPs seed layers on ITO substrates, which were prepared by drop-casting varied volumes of ZnO NPs solution (i.e. 5, 10, 15, and 20μl). It is clear from this images that the seed layers are uniform and pinhole free until one uses a solution of 15 µl. At higher concentrations, seed layer develop cracks.

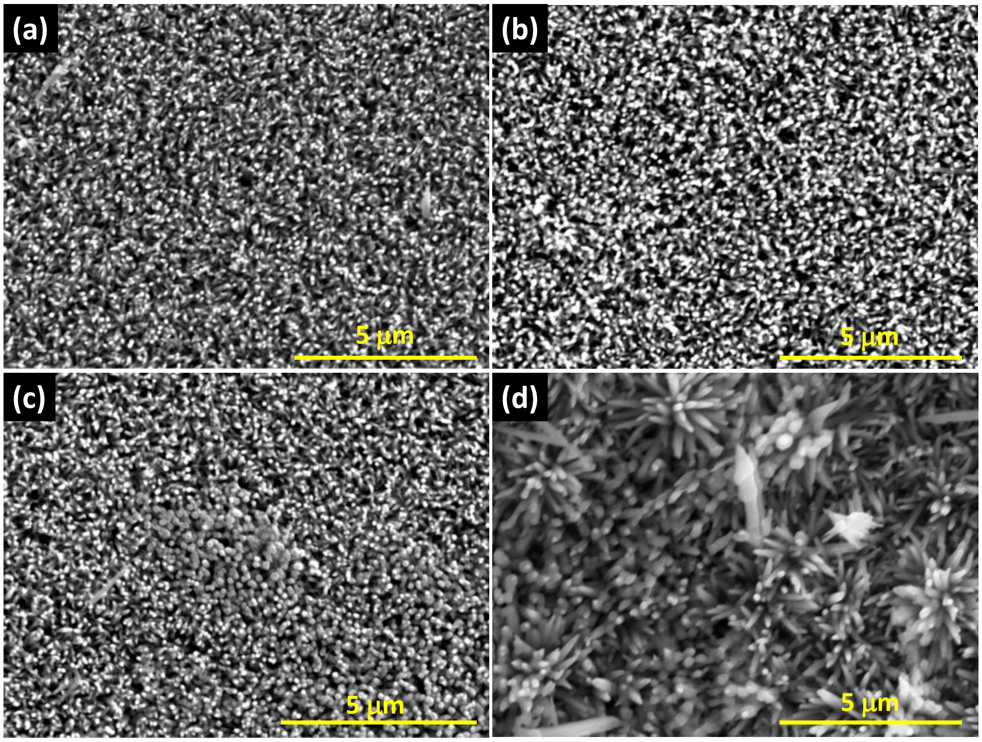

Figure 3.30: SEM Images of ZnO NW grown on ITO substrate by using (a) 5 µl, (b) 10 µl, (c) 15 µl, and (d) 20 µl of ZnO NP solution as seed layers.

Fig. 3.30 shows the SEM images of ZnO NWs array grown on different seed layered substrates (i.e. 5, 10, 15, and 20µl). It is evident from the images that seed layer prepared using 10 µl volume of the ZnO NP solution (i.e. seed layer b) results in highly packed, well aligned and vertically oriented ZnO NWs array among a series of seed layers. For seed layer using 20 µl volume of the ZnO NP solution, nanowires are found to be disoriented and over grown at some places. Therefore, the optimized seed layer (Fig. 3.29 b) was further used for ZnO NW film preparation, and for fabrication of hybrid solar cells.

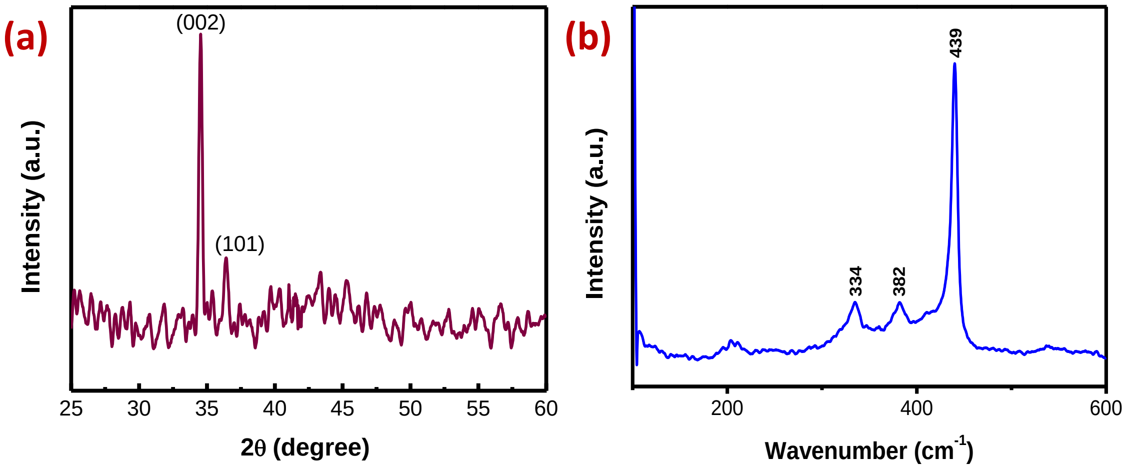

Figure 3.31: (a) X-ray diffraction pattern and (b) Raman spectrum of ZnO NW array grown onto ITO substrate.

The XRD pattern and Raman spectrum of the ZnO NW array is presented in Fig. 3.31. A prominent peak is observed at 2θ = 34.5°, which suggests that ZnO nanowires grow along c-direction (002) perpendicular to the substrate plane. The Raman spectrum of ZnO NW recorded at room temperature show a sharp and dominant E_2 (high) mode at 439cm^{-1}, which corresponds to the intrinsic mode of wurtzite hexagonal ZnO structure associated with oxygen displacement[115]. The two weak peaks at 334 and 382 cm^{-1} may correspond to multi-phonon scattering process of (E_2 (high)-E_2 (low)) and A_1 (TO), respectively[116]. The presence of high intense E_2 (high) mode and suppressed E_1 (LO) mode suggests high crystalline nature of ZnO NWs.

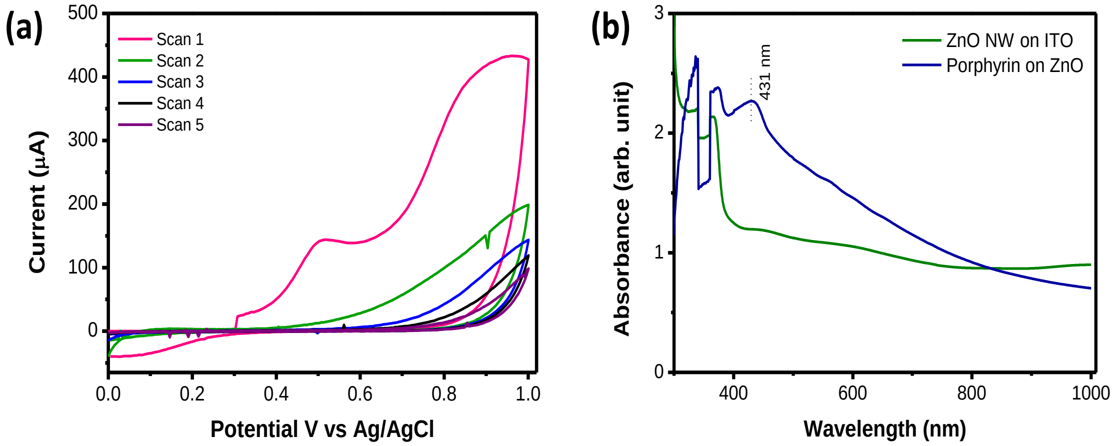

Figure 3.32: (a) First 5 cyclic voltammograms of electrodeposition of porphyrin on ZnO-NW electrodes, (b) UV-Vis spectra of ZnO-NW electrode and porphyrin-modified ZnO-NW electrodes.

As described in Chapter 2, hybrid bilayer heterojunction solar cells were fabricated using ZnO-NW as well as porphyrin-modified ZnO-NW. The porphyrin was electrodeposited onto ZnO-NW and the recorded cyclic voltammograms are shown in Fig. 3.32(a). These cyclic voltammograms are almost identical to that of electrodeposition of porphyrin onto ITO electrodes (see Fig. 3.12), indicating almost identical deposition mechanism. The UV-Vis spectra of porphyrin-modified ZnO-NW as well as ZnO-NW are shown in in Fig. 3.32(b), where the absorption peaks at 350nm and 431 nm correspond to ZnO-NW and porphyrin respectively. The high absorbance in ZnO-NW films clearly reveal high opacity of ZnO films.

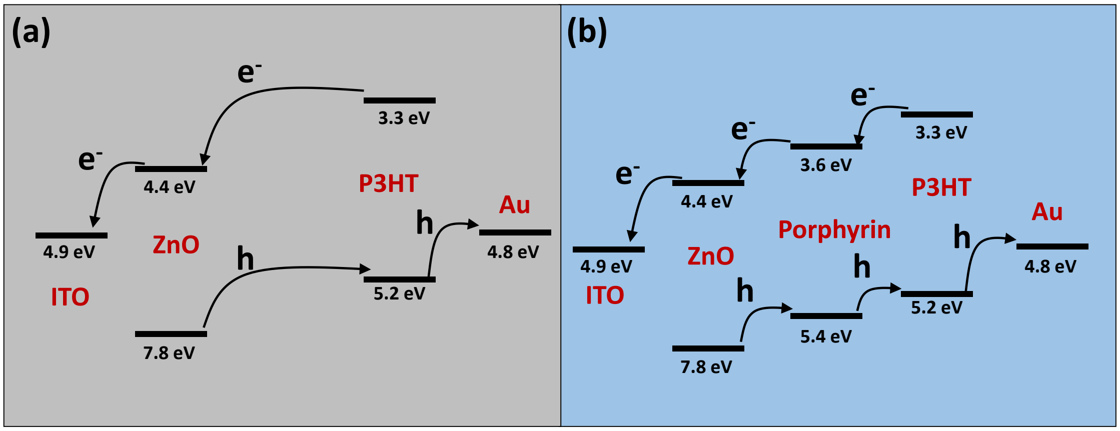

Figure 3.33: Energy level diagram of (a) ITO/ZnO-NW/P3HT/Au and (b) ITO/porphyrin-modified ZnO-NW/P3HT/Au hybrid bilayer solar cells.

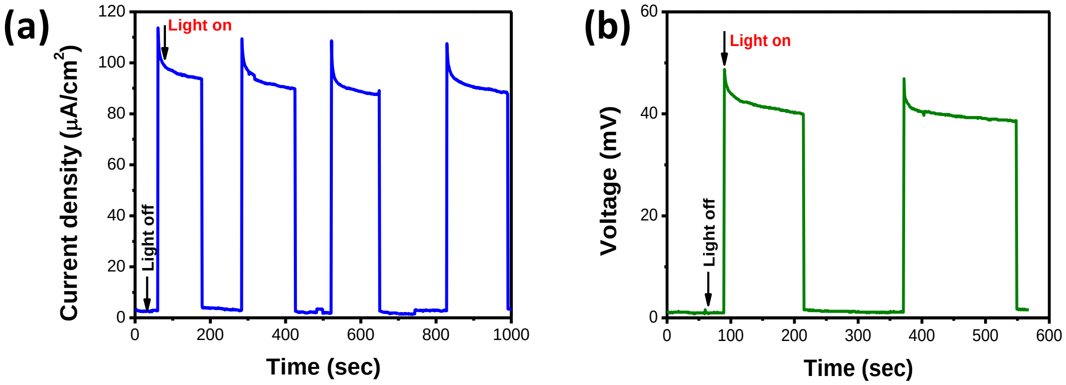

Figure 3.34: Photoresponse of (a) short-circuit current density's (b) open-circuit voltages under dark and white light illumination (5mW/cm^2)

3.3.2 Photovoltaic characteristics of hybrid solar cells

The energy level diagrams of ITO/ZnO-NW/P3HT/Au and ITO/porphyrin-modified ZnO-NW/P3HT/Au solar cells are schematically shown in Fig. 3.33. It is evident that addition of intermittent porphyrin layer is advantageous as it lowers the band-offset for electron/hole dissociation, which facilitates the charge transport. The photoresponse characteristics of these hybrid solar cells were measured under white light (5 mW/cm^2)

illumination. It may be noted that no photoresponse was observed for ITO/ZnO-NW/P3HT/Au solar cells. This can be explained on the basis of large band offset between ZnO and P3HT, which results in recombination of photogenerated carriers. In the case of ITO/porphyrin-modified ZnO-NW/P3HT/Au a good photoresponse was observed. The measured values of I_{sc} and V_{oc} were respectively, ~100μA/cm^2 and ~50mV. The obtained efficiency of the devices was <0.001%. A very low efficiency is attributed to several factors, such as, large phase separation between donor and acceptor (i.e. leading to the poor charge collection), high disorder present at the interfaces (i.e. high recombination) etc. The typical time decay of I_{sc} and V_{oc} is shown in Fig. 3.34. A fast decay of these parameters indicates the presence of localized states at the interface. Clearly there is a need to optimize the device parameters to improve the device efficiency.

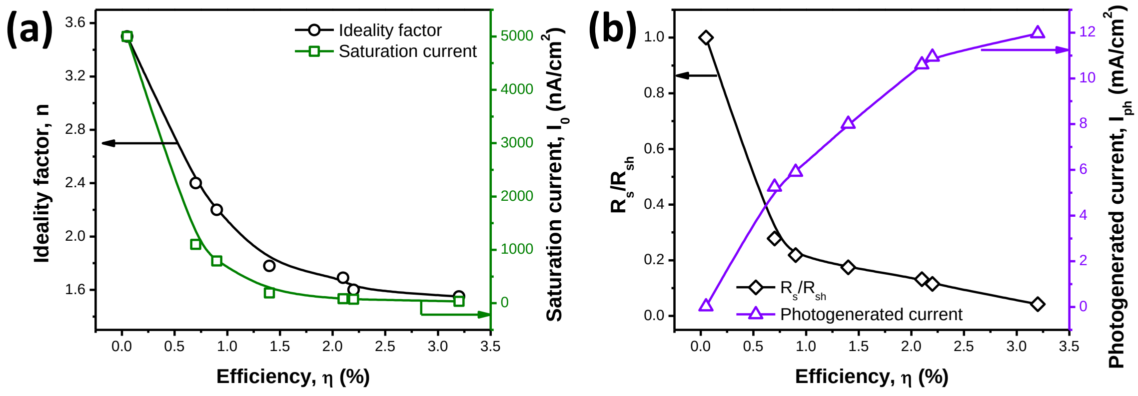

Figure 3.35: A plot of (a) ideality factor, saturation current obtained by fitting *J*-*V* curves vs. efficiency of the respective devices obtained experimentally; (b) R_s/R_{sh}, photogenerated current obtained by fitting *J*-*V* curves vs. experimentally obtained efficiency of bilayer and bulk-heterojunction solar cells.

3.4 Conclusions

We have fabricated three types of polymer solar cells namely, P3HT:PCBM bulk-heterojunction solar cells, porphyrin/polyfullerene diffuse bilayer solar cells and porphyrin-modified ZnO nanowires based hybrid solar cells. Among these, P3HT:PCBM exhibited highest efficiency of 3.2% when annealed at 130°C for 30 min, and the hybrid solar cells exhibted the least effciency. The *J-V* curves of the devices were analyzed using a diode model. Plots of device parameters with experimentally obtained effciencey are plotted in Fig. 3.35. It is clearly seen that as the for devices with higher effciency, the ideality factor and saturation current decreases, while R_{sh}/R_s ratio and photgenerated current increases. In the case of P3HT:PCBM devices, temperature dependent *in-situ* Raman spectroscopy and optical microscopic studies have shown that the highest ordering/crystallinity is obtained at 130°C. Improved ordering implies less recombination (i.e. low n value) and improved charge transport (low R_s and high J_{sc}), and therefore high efficiency. In the case of porphyrin/polyfullerene diffuse bilayer solar cells and porphyrin-modified ZnO nanowires based hybrid solar cells, large phase separation between donor and acceptor and high disorder at the interfaces lead to high n values and low efficiencies.

Chapter -4

Dye-sensitized solar cells: Effect of photoanode, electrolyte and counter electrode on device performance

In Chapter 3, we have demonstrated that the efficiency of polymer solar cells is improved by an appropriate annealing of the active layer that induces an ordering in the active layer, which, in turn, reduces the recombination losses. In this Chapter, we fabricate dye-sensitized solar cells (DSSC) with an aim of minimizing the recombination losses. As described in Chapter 1, the various recombination losses in DSSCs occur at TiO_2/dye, and TiO_2/electrolyte etc. These losses also depend upon the nature of the photoanode, electrolyte and counter-electrode. The effect of these three components on the efficiency of DSSC are investigated.

(i) *Photoanode* i.e. organic or inorganic dye molecules sensitized on ZnO and TiO_2 surface.

(ii) *Redox electrolyte* i.e. I^-/I_3^- redox couple in organic, aqueous solvent, and quasi gel.

(iii) *Counter-electrode* i.e. platinum on FTO or freestanding polypyrrole films.

4.1 Effect of photoanode

4.1.1 ZnO photoanode

As described in Chapter 1, one dimensional (1D) ZnO nanostructures with an advantage of high electron mobility as compared to that of TiO_2 are potential candidates as photoanodes for DSSC. In this section, results on devices made using ZnO-NWs as photoanode have been presented. ZnO-NWs were thermally grown on ITO substrates, as described in Chapter 2, and their morphological and structural properties were presented in Chapter 3.

(a) *Photovoltaic characterization with ZnO Photoanodes*

First we describe the characteristics of ZnO-NW electrodes sensitized using organic (PM567) and inorganic (N3) dyes (as discussed in Chapter 2) [117]. Fig.4.1 depicts the absorption spectra of both PM567 and N3 dye on ZnO surface. The strong peak at 522 nm is attributed to π-π* transition. When the dye was absorbed onto ZnO surface, the absorption peaks broadened slightly and showed negligible red shift (518 nm) in peak position as compared to the dye solution, implying that dye did not aggregate on the TiO_2 surface. In addition, a shoulder at 492 nm is observed for both the cases. The absorption peaks of N3 dye were observed to be 390 nm and 530 nm corresponding to π-π* transition as reported in literature[118].

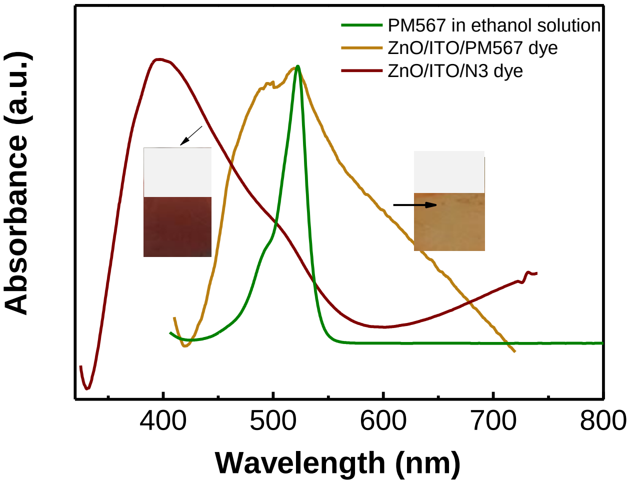

Figure 4.1: UV-Vis spectra of the ZnO NW array sensitized with (a) PM567 and (b) N3 dyes. Inset shows the pictures of the sensitized electrode.

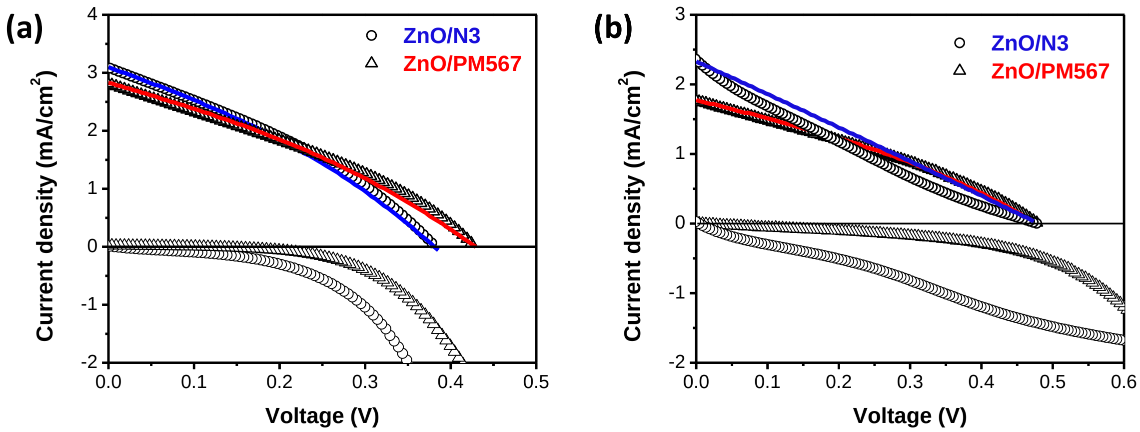

Figure 4.2: Measured (symbol) and fitted (solid line) *J-V* characteristics of the dye sensitized solar cell using PM567 and N3 dye sensitized electrode in (a) I_3^-/I^- electrolyte and (b) Fe^{+++}/Fe^{++} electrolyte

Table 4.1:- Photovoltaic parameters and evaluated solar cell parameters of PM567 dye, N3 dye based DSSCs in Aqueous I_3^-/I^- and Aqueous Fe^{+3}/Fe^{+2} electrolytes

DSSC	J_{sc} (mA/cm^2)	V_{oc} (mV)	*FF*	η (%)	*n*	I_0 (nA/cm^2)	R_s (Ω-cm^2)	R_{sh} (kΩ-cm^2)	I_{ph} (mA/cm^2)
PM567 (I_2)	2.84	0.43	0.33	0.81	3.0	400	520	2.8	3.55
N3 (I_2)	3.1	0.38	0.32	0.76	3.1	900	750	2.4	3.76
PM567 (Fe)	1.77	0.48	0.32	0.53	3.2	170	1200	4.6	2.27
N3 (Fe)	2.33	0.48	0.2	0.45	3.7	600	2350	1.1	8.2

For DSSC fabrication, optimized ZnO-NW electrodes (used for hybrid solar cells) were sensitized using PM567 and N3 dyes as discussed in Chapter 2, platinum coated ITO substrates were used as counter electrodes and 0.5 M LiI and 0.05 M I_2 in deionized water or 0.01 M $FeCl_3$ and 0.1M KCl in de-ionized water were used as electrolyte. The photovoltaic performance of the cells was evaluated under the irradiation of intensity 50 mW/cm^2. Fig. 4.2 represents the photovoltaic characteristics (measured and fitted) of the fabricated DSSCs for both PM567 and N3 dyes in different electrolytes. Various device parameters (n, I_0, R_s, R_{sh}, I_{ph}) were estimated by fitting the J-V characteristics to Shockley one diode model, as described Section 3.1.1, and are summarized in Table 4.1.

In all the cases the ideality factor (n) is >3, indicating very high recombination in the devices. The dark current in case of PM567 dye based cell in I_3^-/I^- electrolyte is lower as compared to that in the case of N3 dye based devices. The decrease in the dark current with the usage of PM567 dye may be attributed to the low recombination rate as a result of hydrophobic nature of the dye. This decrease in the dark current results in the increase of V_{oc} for PM567 dye based cell as compared to N3 dye based cell [119]. The photocurrent for PM567 dye based cell is almost equivalent to that of N3 dye based cell in both electrolytes. Overall, the power conversion efficiency of the PM567 dye sensitized electrode is slightly higher than that of N3 dye based DSSC as shown in Table 4.1. The behavior of the cell is different, when Fe^{++}/Fe^{+++} electrolyte was used for the DSSC fabrication. The V_{oc} of the cell using PM567 dye is same as that of N3 based one, perhaps because of reduced dark current. On the other hand, the photocurrent of the N3 dye based DSSC is higher than that of PM567 based DSSC. Nevertheless, the fill factor of the PM567 based DSSC is better than that of N3, thereby, resulting in efficiency improvement.

In addition, the R_s is slightly lower for PM567 dye than N3 dye in case of I_3^-/I^- electrolyte. This indicates improved charge transport properties of the PM567 dye compared to that of N3 dye. Also the shunt resistance for device using PM567 is higher than that of N3, probably because of reduction in dark current and, therefore, results in an increase in the efficiency of the PM567 dye based cell. On the other hand, the situation becomes different when Fe^{++}/Fe^{+++} is used as electrolyte for DSSC fabrication. It is observed that R_s value is higher for PM567 based cell as compared with that of N3 based cell. Whereas, the shunt resistance is higher in case of PM567 based DSSC vis-a-vis N3 based cell. This suggests though the charge transport properties of the PM567 dye deteriorates in Fe^{++}/Fe^{+++} electrolyte, the reduced dark current compensates this effect and therefore, results in improved efficiency (0.54%) as that of N3 based DSSC (0.47%). The use of PM567 dye in cell fabrication also results in more stable performance as compared with N3 dye and therefore, is suitable for aqueous electrolyte. Our results are consistent with recent study where high water content in electrolytes is not associated with poor efficiency or instability of the cell rather it is due to electrolyte diffusion limitation in porous oxide films[120].

4.1.2 TiO_2 photoanode

Although TiO_2 has less electron mobility as compared to ZnO, it has been studied widely owing to its superior performance with many organic and inorganic dyes. Despite of widely been investigated, the recombination of photo-electrons from TiO_2 to electrolyte is a significant issue, which results in enhanced dark currents.

In this section, we report a relatively simpler methodology for layer-by-layer co-sensitization of TiO_2 surface with two dyes for improving the power conversion efficiency (PCE) of the device [121]. In DSSCs two types of dyes namely (a) metal-free organic dye and (b) ruthenium polypyridyl complexes have normally been used. Among the inorganic dyes, ruthenium polypyridyl complexes are vastly studied because the electron (metal-to-ligand charge transfer) transfer is fast. However their molar absorption coefficients are low and they are quite expensive as compared to metal-free organic dyes. Organic dyes, because of low cost and diversity of molecular structures are gaining importance in DSSCs. In order to combine the advantages of ruthenium complexes (high photoelectric conversion efficiency) and metal-free organic dyes (high molar absorption coefficient), we have focused on the co-sensitization of TiO_2 for the fabrication of DSSCs [121].

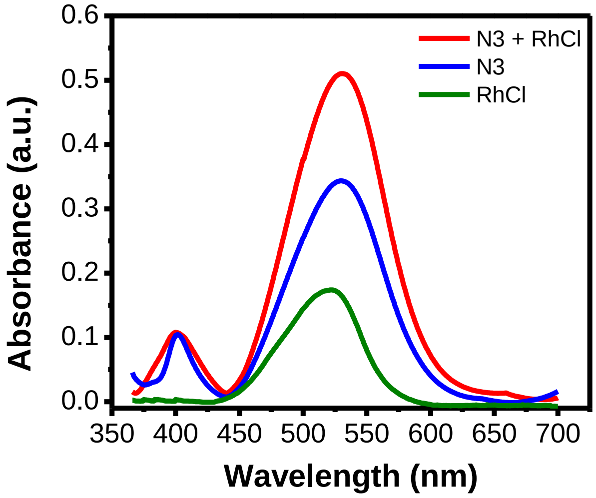

Figure 4.3: UV-Vis spectra of TiO_2 photoanodes sensitized with RhCl, N3 and co-sensitized with RhCl & N3 dyes.

(a) Characterization of co-sensitized TiO_2 photoanode

The fabrication of co-sensitized TiO_2 photoanodes are described in Chapter 2, which are characterized using FTIR and UV/Vis spectroscopy. The results are discussed below.

The normalized UV-Vis spectra (at 400 nm) of TiO_2 photoanodes sensitized with RhCl, N3 and co-sensitized with RhCl and N3 dyes are shown in Fig. 4.3. The RhCl dye sensitized electrode shows a peak at 521 nm corresponding to π-π^* transition; while N3 dye exhibits peaks at 400 nm and 530 nm corresponding to metal-to-ligand charge transfer (MLCT). In the case of co-sensitized TiO_2 electrode, the absorbance intensity corresponding to 530 nm is increased, suggesting the sensitization of both dyes onto single electrode. In addition, the shape of the absorbance curve is not changed significantly, which in turn rules out the possibility of dye aggregation on the TiO_2 surface due to co-existence of both dyes. In order to find the no. of molecules of each dye adsorbed on a TiO_2 photoanode (co-sensitized electrode), we have carried out dye-loading experiments by desorbing the dyes in 0.1M potassium hydroxide (KOH) aqueous solution, detailed calculations are presented in Appendix-I.

It was observed from the calculations that the coverage of TiO_2 surface by RhCl dye is low (1.6×10^{-6}mol/ cm^2) as compared to that by N3 dye (3×10^{-4}mol/cm^2). The low coverage area of RhCl dye on TiO_2 electrode is advantageous as it leaves enough room for the sensitization of other dye (i.e., N3). Despite the low coverage of TiO_2 surface, RhCl works quite efficiently owing to its high molar extinction coefficient. In addition, it was observed that the amount of N3 dye absorbed on RhCl/TiO_2 electrode was 15% higher than that absorbed onto TiO_2 electrode (2.6×10^{-4} mole/cm^2).

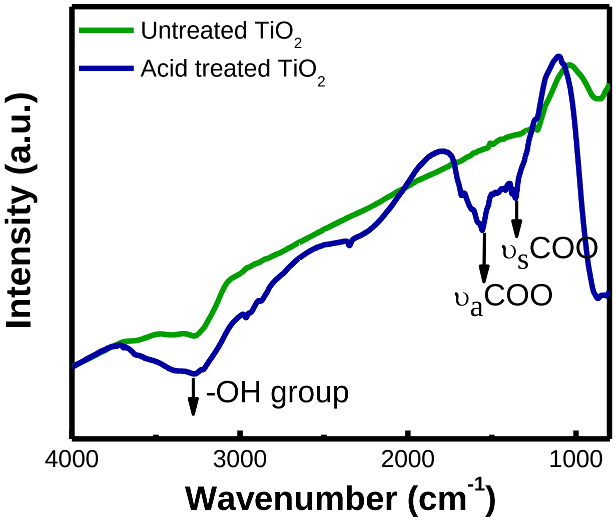

Figure 4.4: FTIR spectra of untreated and formic acid treated TiO_2 surface

To investigate improvement in dye loading on TiO_2, some electrodes were treated with formic acid before dye loading. The FTIR spectra of untreated and formic acid treated TiO_2 photoelectrode are shown in Fig. 4.4. It is seen that untreated TiO_2 exhibits only peak corresponding to OH^-. However, after treating with formic acid, the peaks corresponding to formate ions ($HCOO^-$) are observed and the intensity of the OH^- peak is increased[122].

The FTIR spectra of RhCl dye (in powder from) and RhCl loaded onto formic acid treated TiO_2 electrode are shown in Fig. 4.5. For the sake of clarity of FTIR peaks the data is divided into two wavenumber regimes i.e. 4000-2800 cm^{-1} and 1800-1000cm^{-1}. The inference drawn from these figures are:

(i) The dye as well as TiO_2 photoanode reveal characteristics bands of RhCl at 1370 cm^{-1} (C-N stretching), 1448 cm^{-1} (C-N stretching)and 1715 cm^{-1} (C-O stretching) suggesting the RhCl dye is indeed loaded on to the TiO_2 photoanode.

(ii) The intensity of 1189 cm^{-1} (perchlorate ions) remains nearly remains same in both the cases, indicating that perchlorate ions of RhCl do not participate in its binding to the TiO_2 surface.

(iii) The peak 3376 cm^{-1} (-N-H stretching) vanishes in the case of TiO_2 photoanode, while the intensity of 1648 cm^{-1} (-N-H bending) reduces significantly. This suggests that RhCl binds to the TiO_2 surface through an electrostatic interaction between positively charged dye (N^+) and negatively charged formate ions present at the TiO_2 surface.

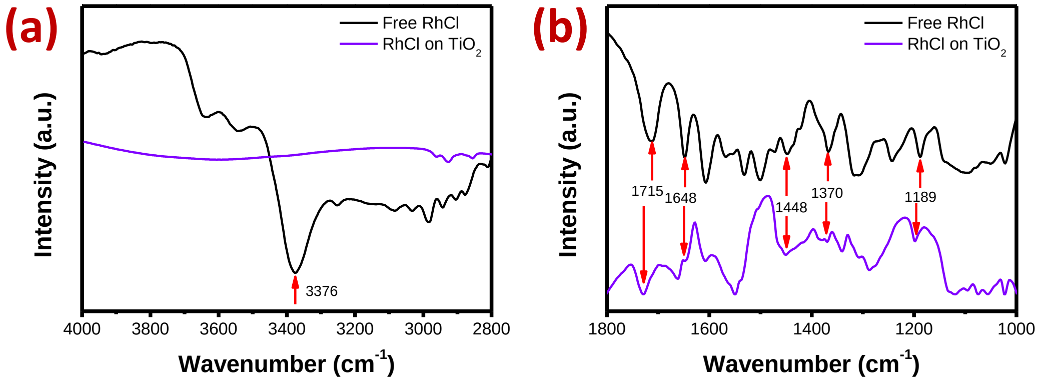

Figure 4.5: FTIR spectra of free RhCl dye and RhCl loaded TiO_2 electrode in two different regions.

From the above studies, it is evident that both dyes (RhCl and N3) are adsorbed on the surface of TiO_2, whereas the absorbed formate ions on TiO_2 surface provide anchoring sites for the RhCl dye absorption; while surface hydroxyl groups of TiO_2 serve as anchoring sites for N3 dye, as schematically depicted in Fig. 4.6. Sensitization of RhCl on TiO_2 electrode takes place through electrostatic interaction between positively charged dye (N^+) and negatively charged TiO_2. The N3 dye, on the other hand, anchors to the hydroxyl group of TiO_2 via hydrogen bond using two carboxylic acid groups in bridging co-ordination.

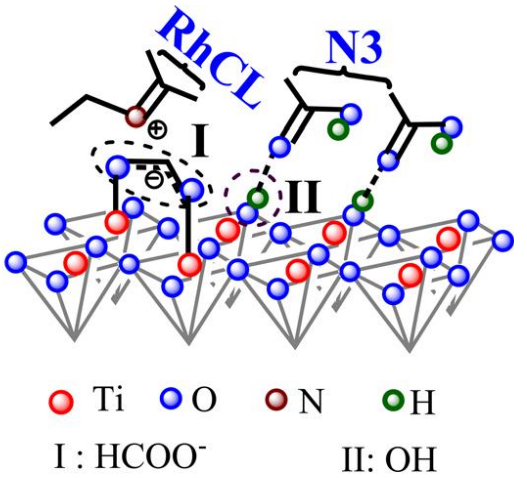

Figure 4.6: Schematic representation of the binding of RhCl and N3 dyes on the formic acid treated TiO_2 surface. Dashed lines represent the hydrogen bonding between OH groups and N3 dye.

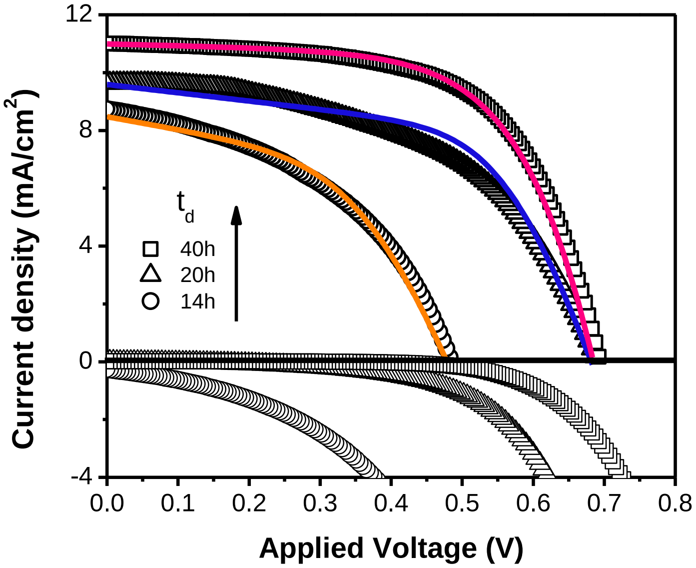

Figure 4.7:- Typical measured (symbol) and fitted (solid line) *J-V* characteristics of co-sensitized DSSC under dark, and AM 1.5, 1Sun condition with different dipping times in N3 dye.

(b) Photovoltaic characteristics of co-sensitized DSSC

The co-sensitization process was optimized by observing the variation in the photovoltaic properties of DSSCs with variation in dipping time in different dye solutions. For this purpose, the TiO_2 electrode was first refluxed in RhCl dye solution for 2h as mentioned above and then dipped in N3 dye solution for different time intervals (t_d). Typical *J-V* characteristics obtained with different dipping times in N3 dye solution are shown in Fig. 4.7. Device parameters (n, I_0, R_s, R_{sh}, I_{ph}) were evaluated by fitting these *J-V* characteristics to Shockley one diode model, as described in Section 3.1.1, and the obtained results are summarized in Table 4.2. It is evident from the plot, the photocurrent of the devices increases with an increase of t_d with simultaneous decrease in the dark currents. This is expected as the area coverage of TiO_2 with N3 dye increases with the increase in dipping time (up to 40 h). The increase of photocurrent and reduction of dark current occurs due to prevention of reverse electron transfer from TiO_2 to the electrolyte. This was also confirmed by low n, I_0, R_s and high R_{sh}, I_{ph} values for the devices sensitized for 40hrs. As a result, V_{oc} and fill factor (FF) also increase. Thus the efficiency of the device increases with the increase in t_d. However, further increase in t_d (i.e., >40 h) leads to dye aggregation, which leads to a decrease in the efficiency.

Table 4.2: Photovoltaic parameters and evaluated solar cell parameters from current-voltage characteristics presented in Fig. 4.7

N3+RhCl (Dipping Time)	J_{sc} (mA/cm^2)	V_{oc} (V)	FF (%)	η (%)	n	R_s (Ω–cm^2)	R_{sh} (kΩ–cm^2)	I_0 (nA/cm^2)	I_{ph} (mA/cm^2)
14h	8.7	0.49	44	1.87	2.0	14	0.22	600.0	8.90
20h	9.8	0.68	51	3.4	1.7	10	0.34	1.4	9.87
40h	11.0	0.69	62	4.74	1.5	8	1.67	0.16	11.01

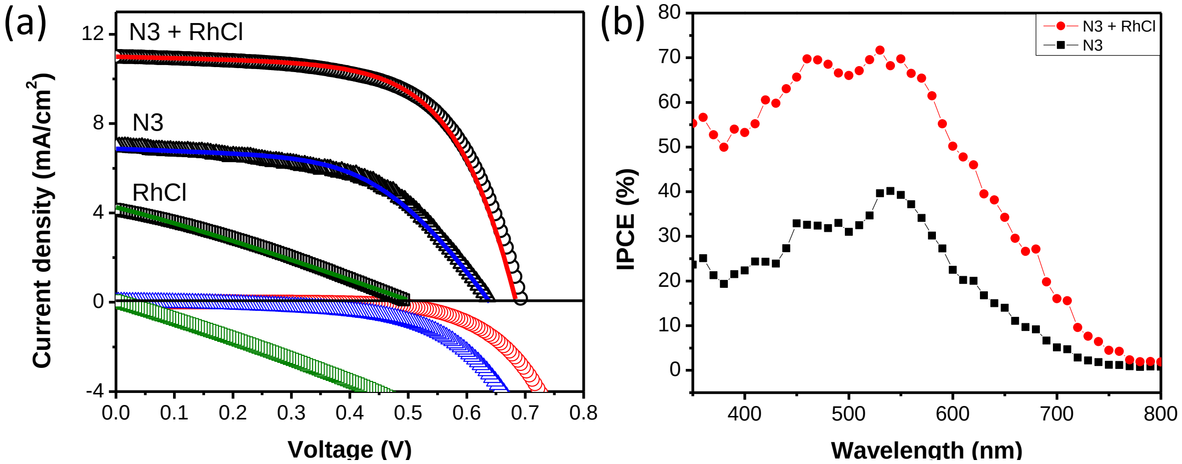

Figure 4.8:- (a) Typical dark and photo (measured (symbol) and fitted (solid line)) *J-V* characteristics of solar cells made using RhCl, N3, and both dyes (b) Typical IPCE spectra of N3 and N3+RhCl dyes

Table 4.3: Solar cell parameters evaluated from current-voltage characteristics presented in Fig. 4.8a

Device	J_{sc} (mA/cm^2)	V_{oc} (V)	FF (%)	η (%)	n	R_s (Ω–cm^2)	R_{sh} (kΩ–cm^2)	I_0 (nA/cm^2)	I_{ph} (mA/cm^2)
RhCl	4.16	0.5	30	0.63	2.46	14	0.22	600.0	8.90
N3	6.97	0.64	53	2.37	2.28	18	1.03	121.0	9.8
N3+RhCl	11.0	0.69	62	4.74	1.5	8	1.67	0.16	11.01

Photoanodes were also prepared using single dyes in order to compare the device performance. The optimized performance of the dye co-sensitized TiO_2 electrodes was compared with the performance of TiO_2 electrodes sensitized with individual dyes (i.e., RhCl or N3). Typical *J-V* characteristics thus obtained and various device parameters evaluated are shown in Fig. 4.8 and Table 4.3, respectively. The efficiency measured for ten devices each fabricated using N3, RhCl or co-sensitized TiO_2 electrodes varied in the range of 2.21-2.43 (2.32), 0.59-0.63 (0.61), and 4.65-4.89 (4.77)%, respectively (the numbers given in the parentheses are the average values). The small variations in efficiency indicate high reproducibility of the fabricated devices. The efficiency of the co-sensitized TiO_2 electrode based devices is significantly higher than that observed for DSSCs based on either RhCl or N3. The efficiency of N3 based dye (2.3%) using ITO substrate is similar to that reported in the literature (1.9%–2.1%) [123, 124]. The efficiency of RhCl based devices is low because of narrow band absorption of the dye as well as low area coverage of TiO_2 surface by the dye. The efficiency of co-sensitized electrode (4.7%) is very high if we take into account the fact that the device was fabricated using 4 μm thick TiO_2 film on ITO substrates. These improvements were expected to result from (i) improved light absorption due to presence of two dyes and (ii) reduced dark current due to dense packing of two dyes on TiO_2 electrode as well as reduced dye aggregation because of different anchoring sites for RhCl and N3 dyes. As presented in Table 4.3, it may be noted that very low values of n, I_0, R_s and high values of R_{sh}, I_{ph} in the case of co-sensitized devices reveal low recombination losses occurring at TiO_2-electrolyte interfaces.

This is further supported by recorded incident photon-to-current conversion efficiency (IPCE) spectrum for the co-sensitized electrode based device. The IPCE spectrum of the co-sensitized TiO_2 electrode show wide absorption across visible spectral range as compared with that of N3 based device, see Fig. 4.8(b). The difference is more pronounced in the 450-550 nm range, where IPCE at plateau region is around 70% for co-sensitized electrode as compared to 40% for N3 based DSSC. Consequently, the photocurrent of the co-sensitized electrode based device is significantly higher than that of N3 dye based DSSC.

To examine the second point on the reduced dark current, we focus on the photovoltaic characteristics represented in Fig. 4.8(a). As shown in the figure, the dark current is suppressed significantly in case of dye co-sensitized electrode. We attribute this to the low recombination rate between TiO_2 CB electron and electrolyte and to the higher coverage of TiO_2 surface due to increased absorption of the two dyes. Though the exact mechanism of the reduced recombination rate is not clear, it is known to be a result of the potential barrier posed by the protonation or absorbed anions on the TiO_2 surface due to acid treatment [58]. This decrease in dark current contributes to an increase in V_{oc} for devices fabricated using N3 &RhCl dyes as compared to those based on single dyes[119]. In order to further analyze the cause of FF improvement, we calculated the series resistance (R_s) of the device from the slope of $(dV/dJ)_{V=0}$ (Table 4.2). It is reported in literature that the FF is dependent on the R_s as well as the method of preparation[125]. As evident from the Table 4.2, the value of R_s for the co-sensitized electrode based device is significantly lower than the R_s value for devices based on single dyes. Reduced R_s, and consequent increment in the FF, improves the charge transport properties of the devices fabricated using N3+RhCl dyes as compared to those of individual dyes. In addition, DSSCs co-sensitized with N719 & RhCl dye show superior performance when TiO_2 photoanode is modified with formic acid [126]. Also, RhCl dye based devices show enhanced efficiencies when TiO_2 photoanode was modified with oxalic acid [127].

4.2 Effect of Electrolyte

Electrolytes typically consist of a redox couple and additives dissolved in a liquid solvent. The main function of the electrolyte is the dye regeneration and charge transport between the TiO_2 photoanode and platinized counter electrodes. The photovoltaic performances of dye-sensitized solar cells mainly depend on the choice of redox couple and on the choice of electrolyte solvent employed. In this section, we investigate the stability of the devices with various different electrolytes. The synthesis (formulation) of these electrolytes were described in Chapter 2.

In order to investigate the effect of electrolyte on the efficiency and stability of DSSC, identical devices were fabricated using N3 dye sensitized on TiO_2 photoanode and Pt/FTO counter-electrode but with different electrolytes: (i) I^-/I_3^- redox couple with acetonitrile (ACN) solvent, (ii) I^-/I_3^- redox couple with 3-methoxypropionitrile (MPN) solvent, (iii) aqueous I^-/I_3^- redox couple, (iv) aqueous Fe^{+3}/Fe^{+2} redox couple, and (v) gel polymer electrolyte (GPE).

The bar chart of the conversion efficiency of DSSCs fabricated using different electrolytes shown in Fig. 4.9. It is observed that: (i) GPE exhibits the highest efficiency among all the electrolyte employed; (ii) I_3^-/ I^- redox couple with 3-methoxypropionitrile as an organic solvent shows superior as compare to that prepared in acetonitrile. The high performance with MPN solvent is attributed to high solubility of redox couple as compared to ACN based electrolyte. (iii) Aqueous electrolytes exhibits poor efficiencies, which is attributed to the poor solubility of the redox couples.

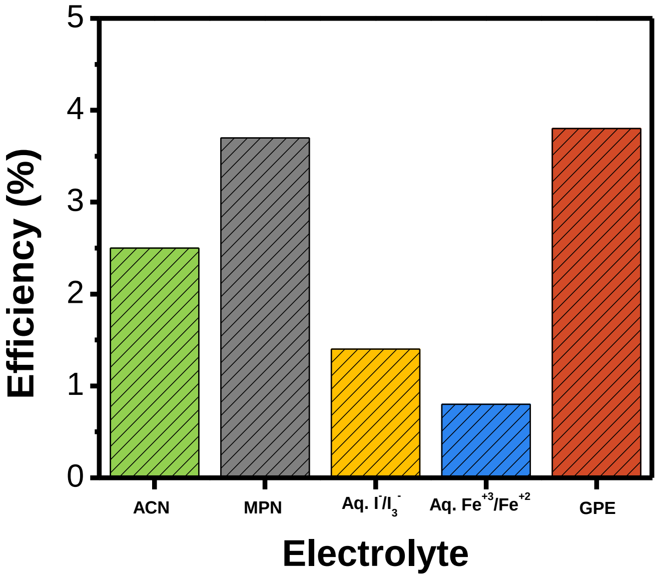

Figure 4.9: Power conversion efficiency of N3 dye-sensitized solar cell with different electrolytes.

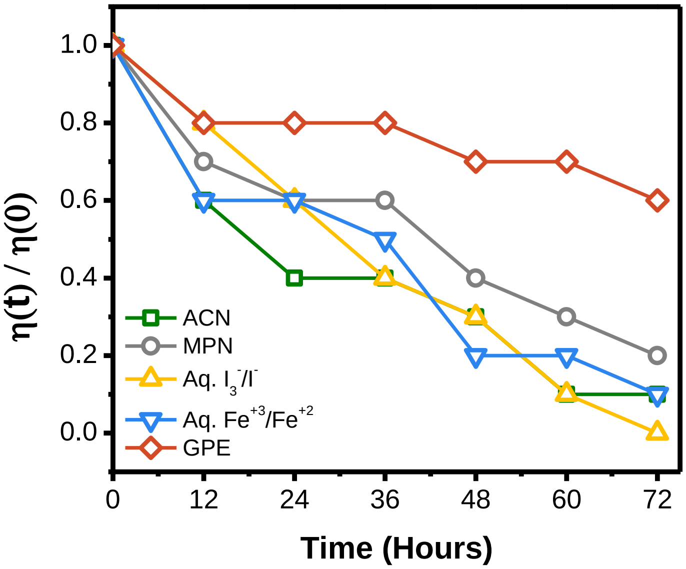

Figure 4.10: Variation of power conversion efficiency (Normalized efficiency = η(t)/η(0)) of N3 dye-sensitized solar cells under illumination with time.

In order to investigate the long term stability of the DSSCs, devices were encapsulated with epoxy, and the efficiency was measured as a function of time. The normalized efficiency i.e. η(t)/η(0) of different devices is plotted in Fig. 4.10. The devices with gel polymer electrolyte show the highest stability with η(t)/ η(0) ~0.6 after 72 hrs. In all of the other cases, the value of η(t)/ η(0) drops to <0.2 after 72 hrs. The poor stability of liquid electrolytes is due to the leakage and evaporation of the solvents. Electrolyte with ACN solvent (boiling point ~80°C) undergoes a rapid degradation of efficiencies as compared to MPN (boiling point ~180°C) because of the lower boiling point of ACN.

4.3 Effect of counter electrode

In this section we present the results on the growth of free-standing polypyrrole films which were also employed as substrate-free, TCO-free counter electrodes for the first time in DSSCs [128].

4.3.1 Growth of free-standing polypyrrole films

The interfacial polymerization of the freestanding polypyrrole film is described in Chapter 2 (see Fig. 2.7). The visual inspection of the film revealed two different textures on either sides of the film, the face formed towards aqueous phase exhibited dense morphology (referred as base or bottom face) while the face towards organic phase appeared porous (referred as top face). This was also confirmed by scanning electron microscopy.

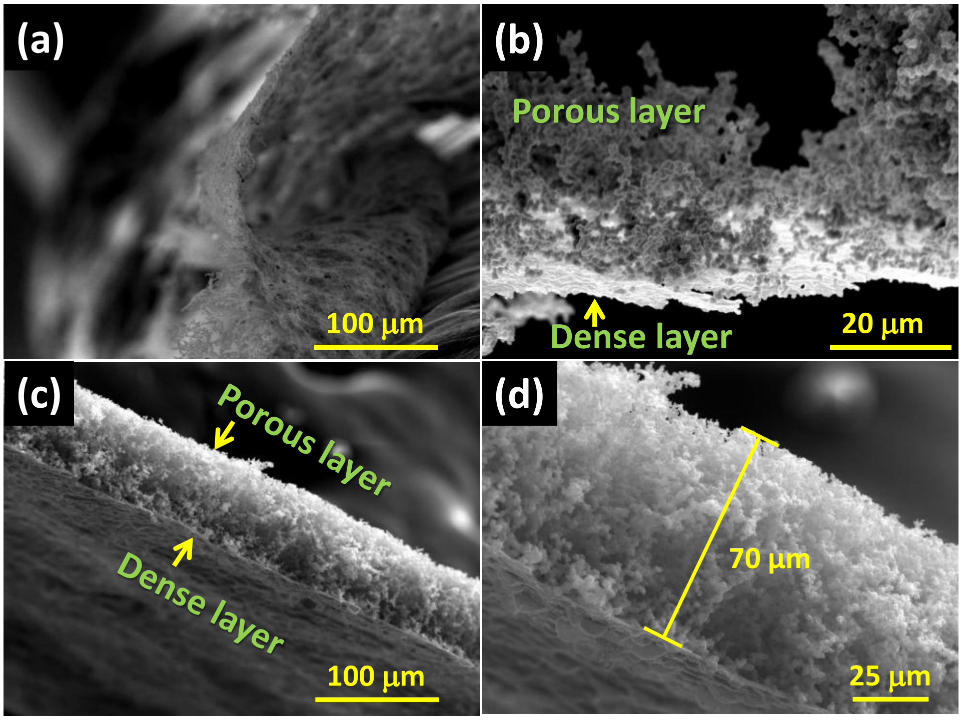

Figure 4.11: Cross-sectional SEM images of the free-standing PPy films polymerized at aqueous/organic interface for: (a) 2h, (b) 4h, (c) 18h, and (d) magnified cross-section of (c)

Fig. 4.11 shows the cross-sectional SEM images of the free-standing PPy films polymerized at aqueous/organic interface for 2h, 4h, and 18h, respectively. From images, it is evident that initially a densely packed polypyrrole film having thickness ~1µm forms (Fig. 4.11 (a), which is followed by a porous and granular film.The thickness of porous structure was observed to increase with polymerization time while the thickness of the compact film remained constant (i.e. ~1 µm). When the polymerization time was kept 4 hrs, the film thickness was of ~25µm. These films were found to be very fragile upon drying and difficult to handle with tweezers. On the other hand, when polymerization time was increased to 18 hrs, thicker films (thickness~70µm) were obtained which were mechanically strong enough to handle as shown in Fig. 4.11 (d).

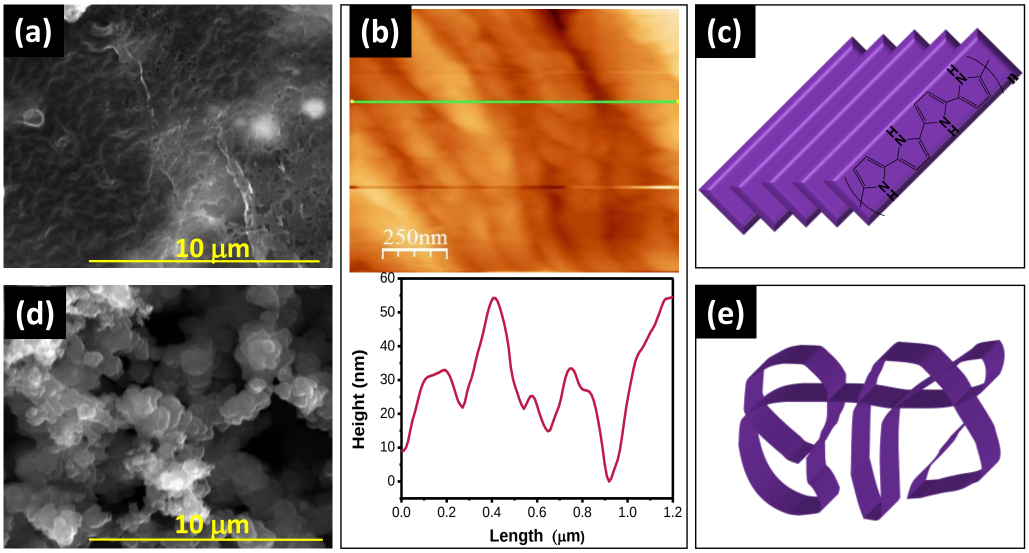

Figure 4.12: SEM and AFM images of the denser and porous surfaces of the PPy films polymerized for 18 h. (a) and (b) are respectively the SEM and AFM images of the denser surface. (c) Schematic showing the oriented polymerized pyrrole chains forming a dense layer at the aqueous/organic interface due to enhanced p–p interactions. (d) Magnified SEM image of the porous surface. (e) Schematic showing the formation of coil-like structure away from the aqueous/organic interface that leads to the formation of porous structure.

In order to further investigate the nature of dense and porous surfaces, we have recorded magnified SEM and AFM images for a PPy films obtained after 18 h of interfacial polymerization. Typical obtained results shown in Fig. 4.12. It is evident from Fig. 4.12(a) and (b) that the dense face of the PPy film is composed of plate-like structures with an rms roughness of 15 nm. The formation of plate-like structure, as schematically depicted in Fig. 4.12(c), is attributed to the fact that the pyrrole molecules are oriented preferentially at the aqueous/organic interface due to H-bonding of pyrrole monomer with water phase[129], and therefore, forming oriented and long polypyrrole chains as the polymerization takes place at 2 and 5 carbon position of the pyrrole ring. The strong π-π interactions among the oriented polypyrrole chains lead to the formation of plate-like structures. On the other hand, the magnified SEM image of the porous surface revealed that PPy has granular (size: ~1μm) structure with deep pores. Due to the deep pores (several microns) the AFM image could not be recorded. In the bulk organic phase (i.e. away from the interface) the pyrrole monomers are randomly oriented, which results in the formation of coil-like polypyrrole chains, as schematically depicted in Fig. 4.12(e). This coil-like polypyrrole chains eventually lead to the formation of granular and porous structure.

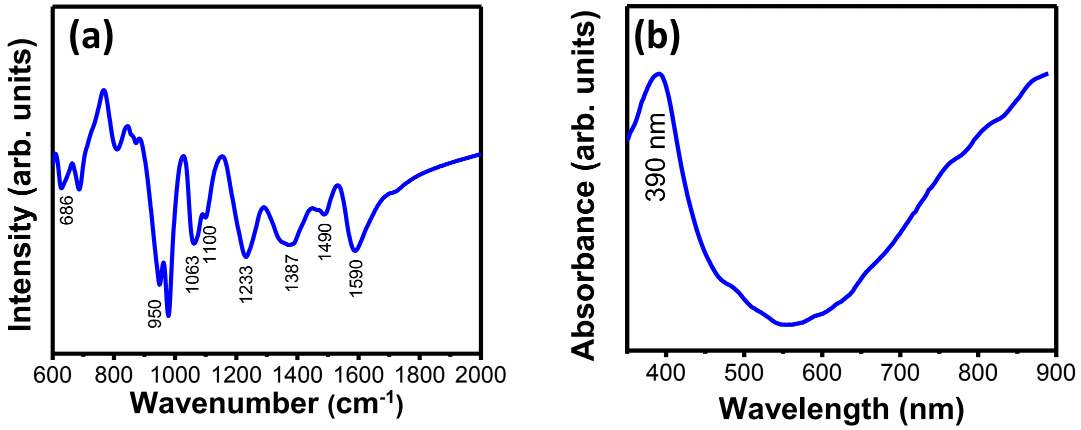

Figure 4.13: (a) FTIR and (b) UV–Vis spectra of free-standing PPy films.

The free-standing polypyrrole films were characterized by FTIR and UV-Vis spectroscopy techniques. As shown in Fig. 4.13 (a), the baseline corrected FTIR spectra of PPy film exhibits all characteristic vibrations of polypyrrole. The peaks observed at 1490 cm^{-1} and 1590 cm^{-1}, and 686 cm^{-1} are attributed to symmetric and anti-symmetric ring stretching modes and C-H out of plane bending of pyrrole, respectively[130]. The bands observed at 1063 cm^{-1} and 1387 cm^{-1} correspond to C–H and N–H deformation vibrations, respectively. The absorption bands at 950 cm^{-1}, 1100 cm^{-1}, and 1233 cm^{-1} correspond to stretching vibrations of doped polypyrrole [131]. The doped form of the polypyrrole is also confirmed by UV–Vis spectra (see Fig. 4.13(b)), which shows a low energy tail extending into the near IR region. The high intensity of tail is attributed to the electronic transitions between the valence band and bipolaran band. The doped form of PPy is beneficial as this helps in facilitating charge transport in DSSC. In addition, a band is observed in absorption spectra at 390 nm which is attributed to the π–π* transitions [132].

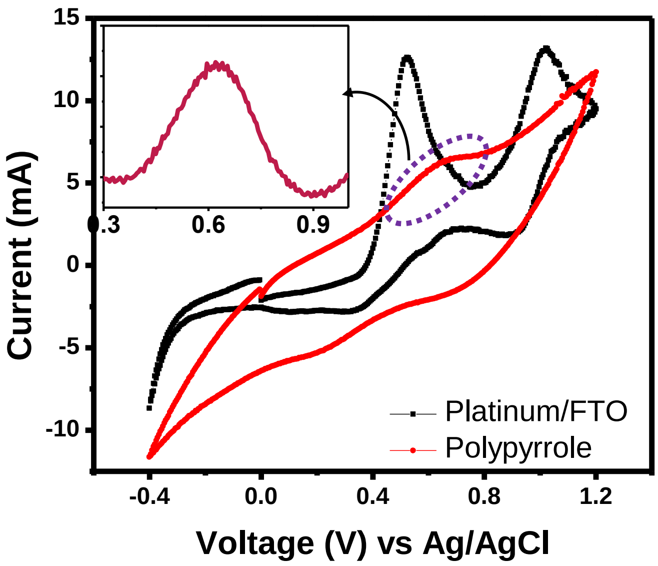

Figure 4.14: Cyclic voltammograms of free-standing PPy films and Pt/FTO in 10 mM LiI, 1 mM I_2, and 0.1 M TBAP in acetonitrile solution at 50 mV/s scan rate. The inset shows the magnified peak after background subtraction for free-standing PPy film.

The electro-catalytic activity of free-standing films was examined for I^-/I_3^- redox couple by recording the cyclic voltammograms (CV). Cyclic voltammetry (CV) measurements for the I_3^-/I^- redox couple were carried out in a three electrode electrochemical cell with pristine free-standing film as working electrode, platinum foil as counter electrode, and an Ag/AgCl reference electrode in 10mM LiI, 1mM I_2, and 0.1M TBAP in acetonitrile solution at a scan rate of 50mV/s. The electrochemical reaction at the counter electrode surface is described by equation 4.2 and 4.3.

$$I_3^- + 2\,e^- \leftrightarrow 3I^- \qquad (4.2)$$

$$3I_2 + 2\,e^- \leftrightarrow 2I_3^- \qquad (4.3)$$

Fig. 4.14 shows the typical cyclic voltammograms of both Pt and free-standing PPy counter electrodes in 10 mM LiI, 1mM I_2, and 0.1 M TBAP in acetonitrile solution at 50 mV/s scan rate. For Pt, the anodic/cathodic peaks corresponding to oxidation/reduction of I_3^-/I^- and I_3^-/I_2 are clearly seen at 0.52 V and 1.02 V, respectively. Of these two redox reactions, the one corresponding to Eq. (4.2) i.e. oxidation/reduction of I_3^-/I^- is important from device point of view. However, in the case of PPy, a weak peak at 0.62 V corresponding to the oxidation potential of I_3^-/I^- is observed (magnified version of the peak is shown in the inset of Fig. 4.14) [130]. The magnitude of cathodic/anodic current density is quite smaller for PPy as compared to Pt, and this is expected, as the PPy has relatively poor conductivity. In addition, the porous structure of PPy hinders pathways for the transfer of the electrons. Another point of concern in the CV data of Fig. 6 is a slight positive shift (~0.1 V) of oxidation/ reduction of I_3^-/I^- peak. The redox potential (EF) of the I_3^-/I^- redox couple is governed by the Nernst equation [133]:

$$E_F = E_o + (0.059/n)\ln(I_3^-/I^-) \qquad (4.3)$$

Where n is the number of electron transferred in half reaction. The slightly poor catalytic behavior of PPy film, leads to an increase in I_3^- ions relative to I^- at the PPy surface. This eventually results in the positive shift in the redox potential.

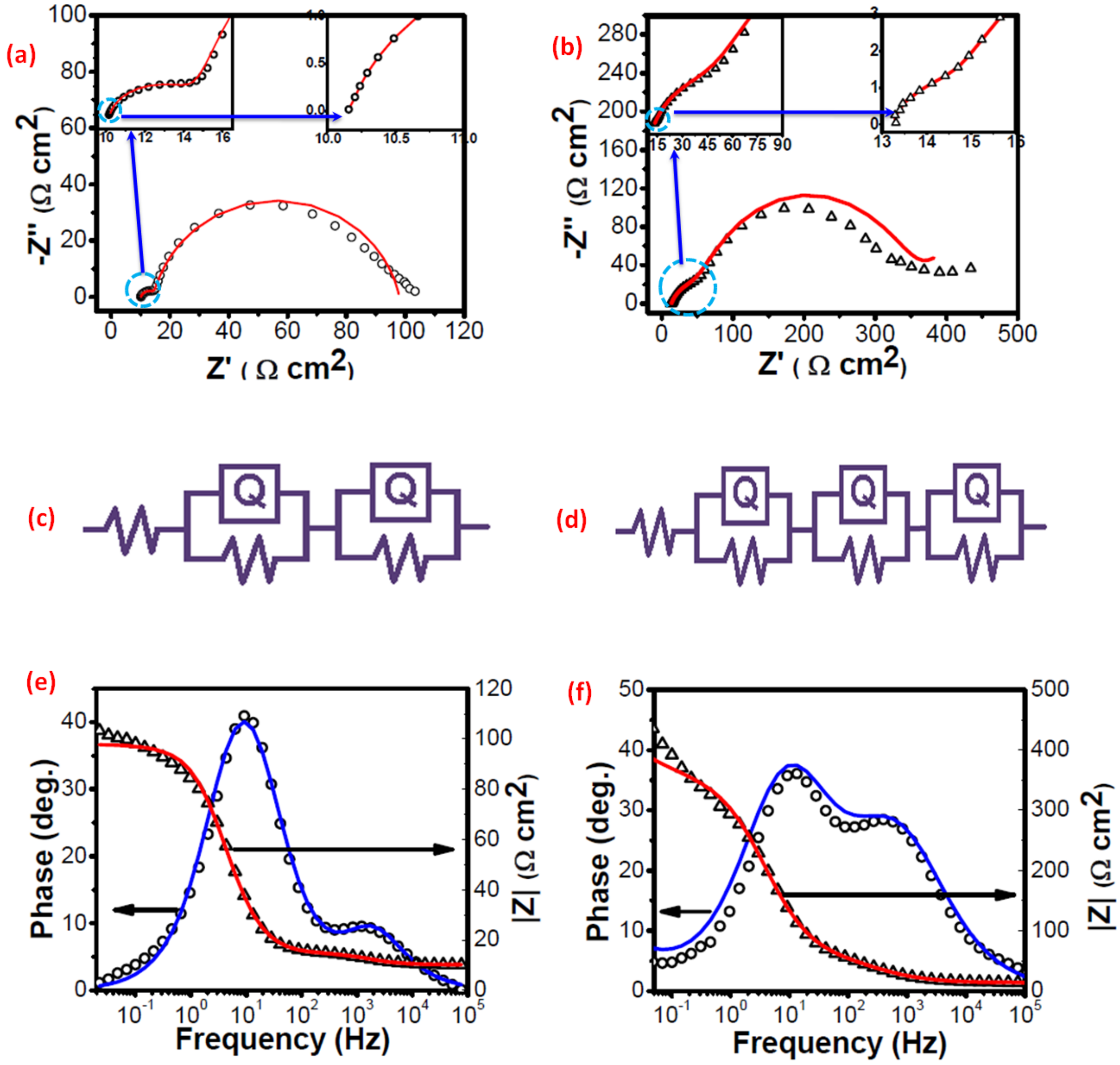

Figure 4.15: Nyquist plots of DSSCs with (a) Pt/FTO, (b) free-standing PPy counter electrodes. Insets on left show the magnified version of charge transfer resistances at counter electrode interfaces and on right shows the porous behaviour of counter electrodes. (c) and (d) are the equivalent circuits employed for fitting the experimentally measured data. (e) and (f) show Bode plots of DSSCs with Pt/FTO, and free-standing PPy counter electrodes.

In order to further gain an insight into the catalytic behavior of free-standing PPy films, electrochemical impedance spectroscopy measurements were carried out. Typical Nyquist plots recorded in the frequency range 500 kHz–0.05 Hz for Pt/FTO CE and PPy CE based DSSCs (with N3 sensitized TiO_2 photoanodes) are shown in Fig. 4.15(a) and (b), respectively. In both the cases, two arcs, one small and another large, are clearly seen.

The inference drawn from these figures are as follows:

i. The smaller arc correspond to high frequency range (500 kHz–500 Hz) and represents charge transfer resistance at CE/electrolyte interface (R_1). The magnified version of the smaller arc is shown in the left insets of the Fig. 4.15(a) and (b), and their further magnified versions of high frequency end are shown in the right insets. It is evident that PPy CE exhibits a smaller arc at very high frequency, which is attributed to the porous morphology of the PPy. A similar observation was reported for porous graphite nanofibres earlier [134]. Absence of this arc for Pt CE is evident as it does not have a porous surface.

ii. The larger arc (corresponding to mid frequency range 500–0.1 Hz) represent the charge transfer resistances at TiO_2/dye/electrolyte interface (R_2).

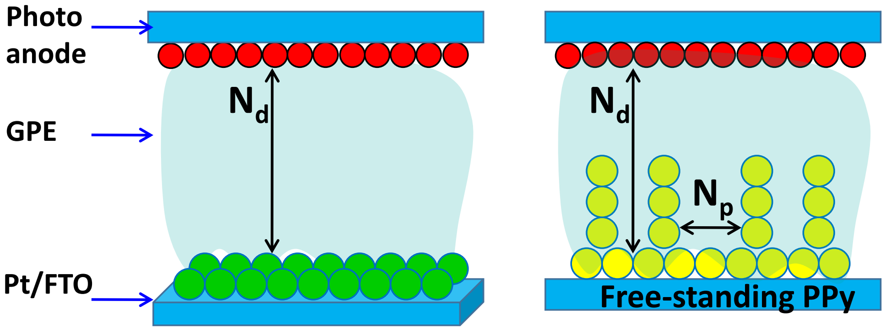

Figure 4.16: Schematic depiction of (a) Nernst diffusion in Pt/FTO based DSSC and (b) Nernst and pore diffusions in free-standing PPy based DSSC.

Based on the above results we infer that Pt/FTO CE has two-dimensional planar structure (i.e. without any porosity), and PPy CE has three-dimensional porous structure. Thus the schematic of DSSC fabricated using Pt and PPy CEs are shown in Fig. 4.16. In the case of Pt based DSSC, the diffusion of ions (I_3^-/I^-) between photoanode and Pt CE can be described by Nernst diffusion (N_d). Therefore, the Nyquist plots can be fitted using an equivalent circuit comprising of a contact resistance (R_s) in series with two RQ elements (R: resistance and Q: constant phase element), see Fig. 4.15(c). Whereas for PPy based DSSC, use of only Nernst diffusion is not sufficient and pore diffusion (i.e. short-distance diffusion within the free-standing PPy film, N_p) need to be considered. Therefore, for PPy CE based DSSCs an equivalent circuits, see Fig. 4.15(d), comprising of 1Rs and 3 RQ elements are used. Using these equivalent circuits, a very good fitting of experimental data is observed with chi-squared value (χ^2, sum of the squares of the residual) $<10^{-3}$. The various estimated parameters for the equivalents circuits are summarized in Table 4.4. It is evident that the values of R_s, R_1 and R_2 are higher for the PPy CE as compared to the Pt CE, which may be attributed to low conductivity and porosity of PPy films. However, the value of R_1 (38.4 Ω cm^2) obtained in our case is lower than that obtained (i.e. 46 Ω cm^2) using electropolymerized PPy films[135].

In order to estimate the electron lifetime (τ_e) in TiO_2 films, the Bode phase plots (phase vs frequency) were recorded for both the DSSCs fabricated using Pt CE and PPy CE, and the results are shown in Fig. 4.15 (e) and (f), respectively. The value of τ_e was estimated from the mid frequency peak (ω_{mid}) of Bode phase plots using the following equation[136]:

$$\boldsymbol{\tau_e = 1/\omega_{mid} = 1/2\pi f_{mid}} \qquad (4.5)$$

The obtained τ_e values are shown in Table 4.3. It is seen that PPy (11.9 ms) and Pt (17.3 ms) CEs have comparable recombination lifetimes. Above results clearly show that freestanding PPy films have reasonable electro-catalytic activity as well as recombination lifetimes. These features along with higher surface area of free-standing PPy films which make them suitable candidate as counter electrode in DSSCs.

Table 4.4: Fitted impedance parameters of Pt/FTO and PPy CE based DSSCs using equivalent circuits, as shown in Fig. 4.15

	R_s (Ω cm^2)	R_o (Ω cm^2)	R_1 (Ω cm^2)	R_2 (Ω cm^2)	τ_e(ms)
Pt/FTO	9.55	-	4.14	76.7	17.3
PPy	13.3	2.7	38.4	302.4	11.9

4.3.2 Photovoltaic characteristics

Free-standing PPy films synthesized by interfacial polymerization for 18h were employed as counter electrodes for the fabrication of DSSCs. In this regard, an electrical contact was taken on top surface (denser face) of the film by thermally evaporating the gold in a vacuum chamber at 10^{-6} bar, later contact was taken through a silver wire to the gold electrode using silver paste as depicted schematically in Fig. 4.17. TiO_2 photoanodes were typically made by doctor blading of TiO_2 paste (Solaronix Inc.) on $TiCl_4$ treated FTO substrates. Later this substrates are sensitized with N3 dye.

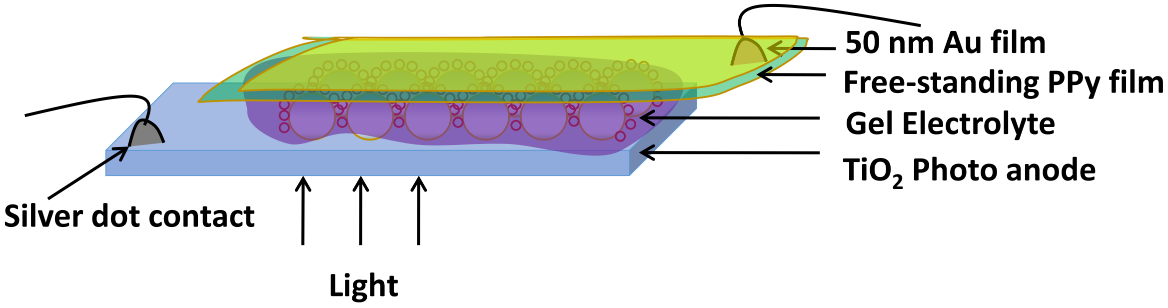

Figure 4.17: Schematic of the DSSC assembly using free-standing PPy film as counter electrode

The photovoltaic performance of the N3 sensitized solar cells using free-standing PPy and Pt/FTO counter electrode were evaluated under AM 1.5 (100 mW/cm^2) light illumination. The recorded current–voltage characteristics are shown in Fig. 4.18. The obtained photovoltaic parameters and evaluated solar cell parameters (n, I_0, R_s, R_{sh}, I_{ph}) for both the DSSC's are summarized in Table 4.5.

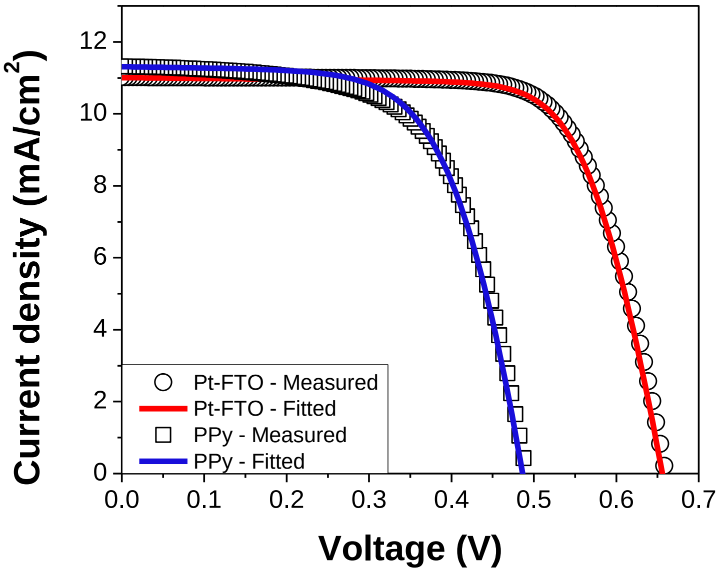

Figure 4.18: Measured (symbol) and fitted (solid line) current–voltage characteristics of DSSCs with Pt/FTO and freestanding PPy counter electrodes under one sun illumination.

Table 4.5: Photovoltaic parameters, and evaluated parameters of Pt/FTO and free-standing PPy CE based DSSCs.

Counter Electrode	J_{sc} (mA/cm^2)	V_{oc} (V)	FF (%)	η (%)	n	R_s (Ω–cm^2)	R_{sh} (kΩ–cm^2)	I_0 (nA/cm^2)	I_{ph} (mA/cm^2)
Pt/FTO	11.01	0.66	73	5.3	1.29	4.98	4.20	0.027	11.02
PPy	11.31	0.49	63	3.5	1.68	5.2	3.18	145	11.31

The main inferences drawn from Table 4.5 are as follows:

i. The open-circuit voltage (V_{oc}) of the DSSC fabricated using PPy CE is slightly lower as compared to that of Pt CE. In general, the V_{oc} of DSSC depends on the difference between quasi-Fermi level of the electrons in the TiO_2 and the redox potential of the electrolyte. In the present case, DSSC's were fabricated using identical photoanode (N3 dye coated TiO_2) and electrolyte (polymer gel) but with different counter electrodes i.e. Pt/FTO or free-standing PPy film. Therefore, the difference in V_{oc} can be attributed to the change in the redox potential of I_3^-/I^-. As discussed earlier, due to the slightly poor catalytic activity of PPy, the redox potential is increased by ~0.1 V, which is reflected in the reduced V_{oc}. Further, V_{oc} is related to I_3^-concentration using the following equation[137]:

$$\mathbf{V_{oc}} = \left[\boldsymbol{KT}/\boldsymbol{e}\right] \ln\left\{\boldsymbol{I_{inj}}/\boldsymbol{n_{cb}k_{et}}[\mathbf{I_3}^-]\right\} \qquad (4.6)$$

where k is the Boltzmann constant, T is absolute temperature, e is an electronic charge, I_{inj} is the flux of charge resulting from sensitized injection, n_{cb} is the concentration of electrons on the surface of TiO_2, k_{et} is the reaction rate constant of I_3^- dark reaction on TiO_2, $[I_3^-]$ is the concentration of I_3^- in electrolyte.

The high concentration of I_3^- ions at PPy surface clearly implies the low V_{oc}. In addition, a high n, I_0 and low R_{sh} values (shown in Table 4.5), clearly suggests increased recombination at PPy-electrolyte interface, leading to low V_{oc}.

ii. On a positive note, the short circuit current density, J_{sc} (11.31 mA/cm^2), of PPy based DSSC is slightly higher than that of Pt based DSSC (11.01 mA/cm^2). J_{sc} in DSSC depends on electron-injection, charge transfer, and charge-recombination processes. Slightly higher J_{sc} in this particular case is attributed to the large surface area of the freestanding PPy CE owing to its porous structure.

iii. In addition to J_{sc} and V_{oc}, the fill factor (*FF*) is another important parameter that determines the performance of the DSSCs. FF is defined as the ratio of the actual maximum obtainable power (P_{max}) to the theoretical power ($P_t = J_{sc} \times V_{oc}$). The *FF* (0.63) of PPy based DSSC is lower than that of Pt based DSSC (0.73). The reduced *FF* of PPy based DSSC is attributed to their enhanced series resistance, which includes contributions from R_s, R_o, R_1 and R_2, as shown in Table 4.5.

iv. The power conversion efficiency (PCE) of PPy and Pt based DSSCs are respectively 3.5% and 5.3%. Apart from the low V_{oc} and *FF*, the adsorbed oxygen on porous PPy (known to be a serious impurity for the organic materials) can reduce the efficiency. Nevertheless, considering the first set of experiments on employing freestanding conducting polypyrrole as counter electrode for the fabrication of DSSCs, the measured efficiency is respectable. The efficiency can be further enhanced by taking appropriate steps, such as, improving the conductivity of the PPy films, optimizing the thickness, reducing the adsorbed oxygen content etc.

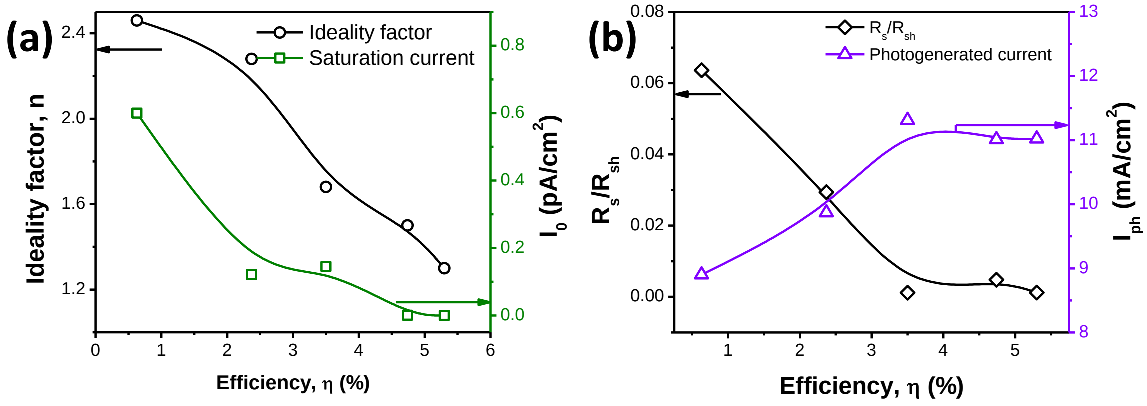

Figure 4.19: A plot of (a) ideality factor, saturation current obtained by fitting *J*-*V* curves vs. efficiency of the respective devices obtained experimentally; (b) R_s/R_{sh}, photogenerated current obtained by fitting *J*-*V* curves vs. experimentally obtained efficiency of dye-sensitized solar cells.

4.4 Conclusions

In order to find a correlation between the experimentally measured efficiency of various DSSCs and fitted device parameters (i.e. n, I_0, R_s/R_{sh}, I_{ph}), we have plotted them in Fig. 4.19. It is observed that, similar to the polymer solar cells, the values of n *and* I_0 decreases as the efficiency of the DSSC increases, indicating that recombination at various interface are reduced for efficient devices. On the other hand, R_{sh}/R_s and I_{ph} increases with efficiency, indicated reduced shunt current and improvement in the charge transport.

We have investigated the effects of photoanode, electrolyte and counter-electrodes on the efficiency of the DSSCs. It has been demonstrated that:

(i) ZnO nanowires based photoanodes yielded better results using organic dye (PM 567) as compared to ruthenium dye (N3). The N3 dye was found to leach out in the electrolyte. TiO_2 photoanode co-sensitized with an organic dye (RhCl), and an inorganic dye (N3), exhited higher efficiency (4.74%) as compared to the induvidual RhCl (0.63%) and N3 (2.37%). The co-sensitization of two dyes resulted in relatively larger coverage of TiO_2 electrode, thereby enhancing the photocurrent and reducing the recombination from electrolyte to the TiO_2 surface, which in turn, improved the efficiency of the device.

(ii) Typical I_3^-/I^- redox electrolyte show better stable device performance for long durations with quasi-gel polymer electrolyte compared to ACN, MPN based electrolytes.

(iii) Free-standing PPy films synthesized by liquid/liquid interfacial polymerization were employed as substrate-free and TCO-free counter electrodes for the very first time in DSSC. The devices with free-standing PPy films as counter electrodes exhibited 3.5% efficiency in comparison to 5.1% obtained for Pt/FTO counter electrodes. The lower efficiency for PPy counter-electrodes is attributed to recombination at PPy/electrolyte interface.

Chapter -5

Summary and Conclusions

At present a huge amount of research is being carried out worldwide in the field of solar cells. This research is aimed at meeting energy requirements by tapping the sunlight, which is estimated to be 120000 TW. Harvesting a small part of this energy using solar cells with efficiency of 10% could easily meet world energy needs. The past research has led to the development of various photovoltaic technologies, such as, (i) crystalline Si cells (single crystal and multi-crystalline), (ii) single-junction GaAs, (iii) thin film photovotaics e.g. Cu(In,Ga)Se_2, CIGS, CdTe, amorphous Si etc., and (iv) organic photovoltaics. Among these, organic solar cells are gaining importance because of low material costs, ease of fabrication, high throughput and flexibility, etc. In addition, organic solar cells (polymer and dye sensitized solar cells) do not require very high purity materials and/or toxic materials, as employed in other solar cell technologies. However, the key limitation of organic solar cells as of now is their lower efficiencies (0.01-15%) arising due to the various recombination losses. In both polymer and dye-sensitized solar cells, several factors, such as, molar extinction coefficient of active material, energy gap, energy level alignment at various interfaces, selectivity of transport layers, and active molecules, and charge dissociation, injection, transport and recombination are the common key issues which strongly influence the efficiency of the devices. In polymer solar cells geminate and bimolecular recombinations are predominant, whereas in dye-sensitized solar cells recombinations take place at TiO_2-electrolyte, and TiO_2-dye interface are significant. Therefore, in both the cases, recombination is a major factor that governs their efficiency. In both devices, presence of disorders at the interfaces trap the charge carries, which enhances the charge recombination. In order to enhance the efficiency it is therefore essential to minimize the disorders, which can be done by optimizing the materials parameters (i.e. morphology, structure, interfaces etc.). In this thesis, we have fabricated both polymer and dye sensitized solar cells under different processing conditions. The photovoltaic characteristics of the devices were measured and various device parameters (i.e. n, I_0, I_{ph}, R_s *and* R_{sh}) were estimated by fitting to an equivalent circuit model. The main results obtained during the thesis work are summarized below.

(i) Polymer solar cells:

- The efficiency of P3HT:PCBM bulk-heterojunction polymer solar cells was found maximum (3.2%) when annealed at 130°C. Annealing temperatures lower or higher than 130°C resulted in lower efficiency.
- The results of *in-situ* temperature dependent Raman spectroscopy and optical microscopy show that the optimum morphology is obtained at 130°C as at this temperature ordering of P3HT molecules is the best while the segregation of PCBM is minimum. This result explained why the maximum efficiency is obtained when devices are annealed at 130°C. At temperatures lower than 130°C, P3HT ordering is poor, while for temperature higher than 130°C aggregation of PCMB takes place. Therefore, we could establish a correlation between the morphology of P3HT/PCBM blend and the efficiency of the solar cells. In addition, the device parameters estimated show that, high efficiency in 130°C annealed devices is mainly due to low n, I_0, R_s, and high I_{ph} values.
- The electrodeposition of polyfullerene films on ITO substrates were investigated for the first time, and the high resolution transmission microscopy results showed that formation of polyfullerene takes via [2+2] cyclo-addition.

- The polyfullerene films were utilized in the fabrication of porphyrin/polyfullerene diffuse bilayer solar cells for the first time. These solar cells exhibited J_{sc} of 2-7 μA/cm^2, V_{oc} of 180-200 mV, and η of 0.002 - 0.005% under 5 mW/cm^2 white light illumination.
- Porphyrin-modified ZnO-NWs were grown by electrodeposition of porphyrin onto hydrothermally grown ZnO-NW electrodes.
- Porphyrin-modified ZnO-NWs/P3HT hybrid solar cells were fabricated which exhibited J_{sc} of ~100μA/cm^2 and V_{oc} of 0.04V under 5 mW/cm^2 white light illumination. It was found that addition of intermittent porphyrin layer is advantageous as it lowers the band-offset for electron/hole dissociation, which facilitates the charge transport.

(ii) Dye sensitized solar cells:

- The DSSC fabricated using ZnO nanowires based photoanodes yield efficiency of ~0.8% for organic dye (PM567) as well as ruthenium dye (N3). However, the stability of N3 dye is poor as it leaches out in the electrolyte. From estimated device parameters, the high efficiency in PM567 based devices is due to low series resistance, saturation current and high shunt resistances.
- The DSSC fabricated using TiO_2 photoanode co-sensitized with organic dye (RhCl) and inorganic dye (N3) exhited higher efficiency (4.74%) as compared to the induvidual RhCl (0.63%) and N3 (2.37%) dye loading. The co-sensitization of two dyes resulted in relatively larger coverage of TiO_2 electrode, thereby enhancing the photocurrent and reducing the back electron transfer from electrolyte to the TiO_2

surface, which in turn, improved the device efficiency. A low n, I_0, R_s and high R_{sh}, I_{ph} also suggests that recombination is greatly reduced by employing two dyes.

- The stability of DSSC devices was highest when I^-/I_3^- gel polymer electrolyte was used. The liquid electrolytes based on aqueous and organic solvents yielded poor stability due to evaporation/leakage or poor solubility of the I^-/I_3^- redox couple in the solvent.
- Free-standing polypyrrole films were synthesized by liquid/liquid interfacial polymerization. They had unique morphology i.e. dense morphology on one side while porous morphology on the other side. These free-standing polypyrrole films exhibited excellent catalytic activity, indicating that their suitability as substrate-free and TCO-free counter electrodes in DSSCs.
- DSSCs were fabricated using free-standing polypyrrole films as counter-electrodes for the first time. The efficiency of the devices was found to be ~3.5%, which is comparable to those fabricated using Pt/FTO counter-electrodes, which was also supported by similar values of R_s, and I_{ph}.

Correlation between efficiency and ideality factor

As discussed in Chapter 1, the ideality factor of the solar cell is a measure of the charge recombination in the device. In order to find a correlation between the ideality factor and the experimentally measured efficiency of polymer as well as dye-sensitized solar cells, we have plotted them in Fig. 5.1. The ideality factor in both the cases decreases as the efficiency of the device increases, indicating that recombination present at various interface are greatly reduced. In the case of polymer solar cells, the annealing of the active layer induced the ordering, which reduced the charge traps. In the case of DSSC, the acid treatment of TiO_2 photoanode along with co-sensitization of two dyes were responsible for the reduction in the surface states [138]. In summary, if the charge traps in polymer and dye-sensitized solar cells are reduced by an appropriate materials processing/treatments, the efficiency of the device will improve.

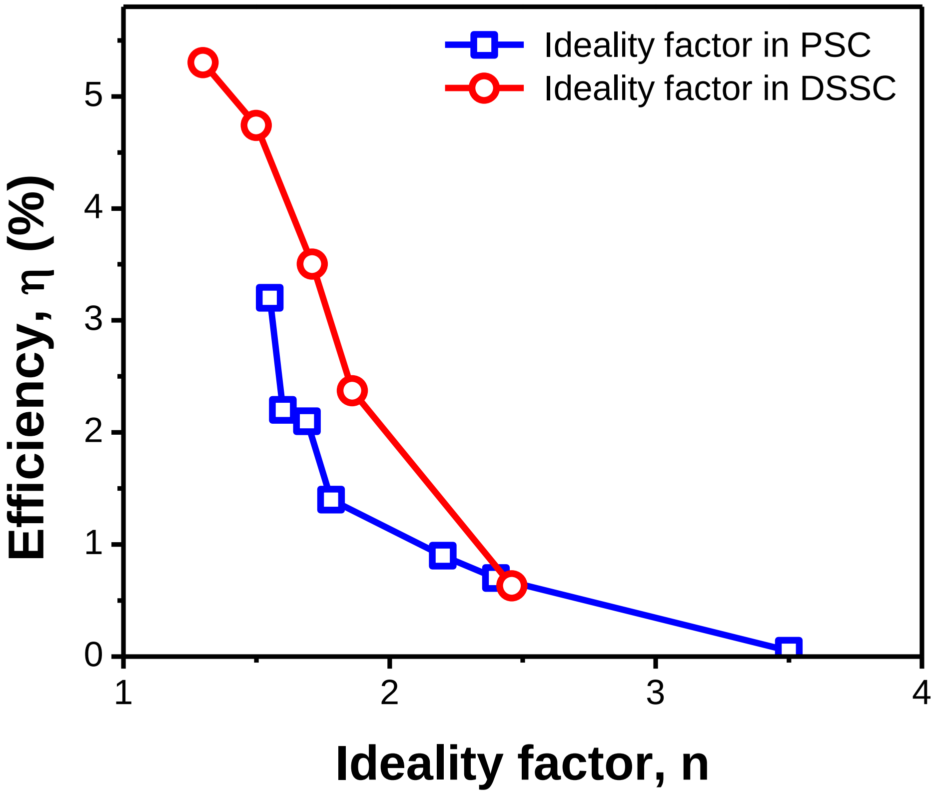

Figure 5.1: A plot of ideality factor obtained by fitting *J*-*V* curves vs. experimentally obtained efficiency of the polymer (square) and dye-sensitized solar cells (open-circle).

Future scope of the work

In this thesis work, several experiments were carried out on polymer and dye-sensitized solar cells and several new insights were obtained. This thesis work opens the following future course of work.

- To improve the BHJ polymer solar cells, PCBM can be replaced by another n-type conducting polymer, such as CNPPV that does not aggregate at high temperatures.
- Improvement of J_{sc}, V_{oc} in porphyrin/polyfullerene diffuse bilayer solar cells, by optimization of various device parameters such as thickness of porphyrin and polyfullerene layers, tuning the morphology of porphyrin layer by anodic alumina template assisted electrodeposition to improve the interfacial area etc.
- In porphyrin-modified ZnO-NW hybrid solar cells, the performance of the devices can be improved further by optimizing the thickness of porphyrin inter layer, optimizing the length of the nanowires, tuning the energy levels by inserting a hole/electron transport layers etc.
- Co-sensitization of two dyes with complementary absorption, by modifying the TiO_2 surface with different co-adsorbents (formic acid, oxalic acid, citric acid).
- Investigation of various other conducting polymer based counter electrodes to replace Pt/FTO electrodes.

Appendix

Molecular Structures

Molecular structures of conducting polymers and fullerene molecules employed in the fabrication of polymer solar cells are depicted in Fig. A1

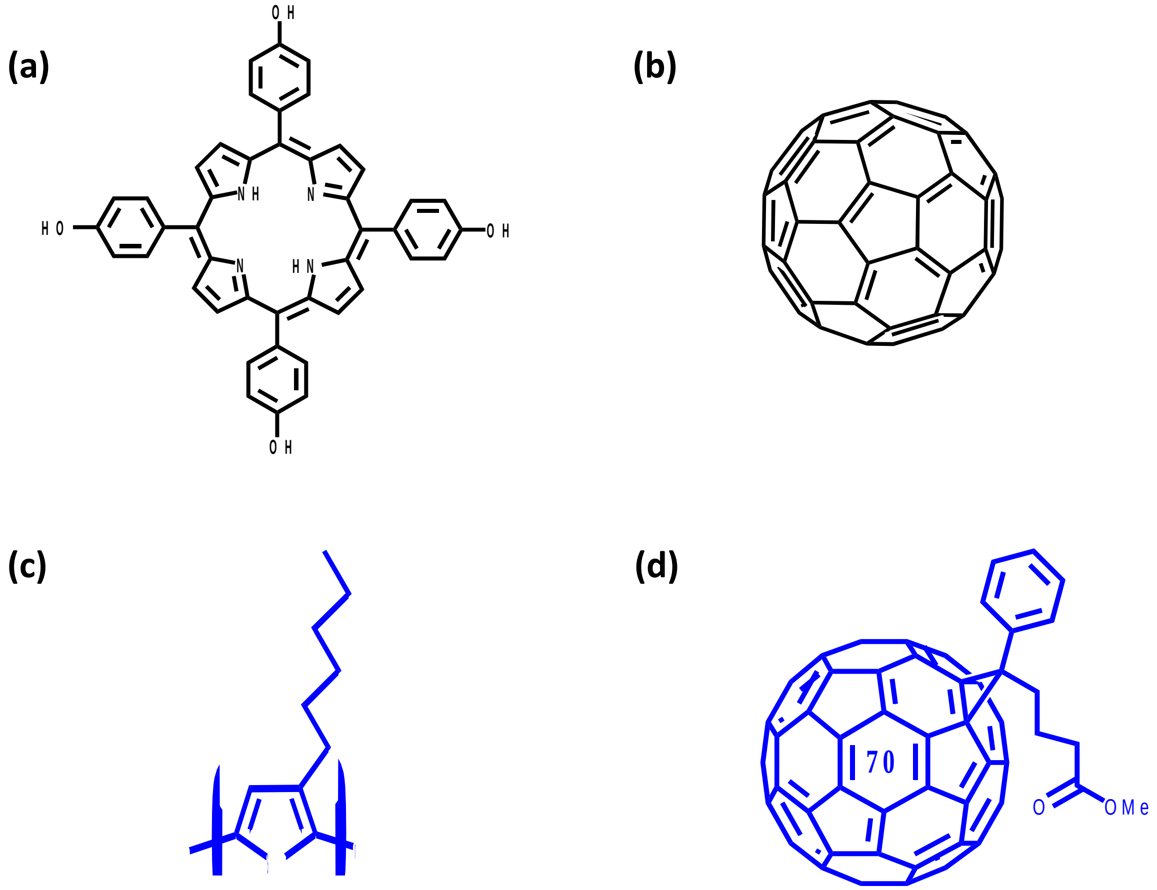

Figure A1: Molecular structures of (a) porphyrin (THPP), (b) fullerene, (c) P3HT, (d) PCBM materials employed in the fabrication of polymer solar cells

(a) **Porphyrin (THPP) -** 5,10,15,20-tetrakis(4-hydroxyphenyl)porphyrin

(b) **Fullerene** – C_{60}

(c) **P3HT** – Poly(3-hexylthiophene-2,5-diyl)

(d) **PCBM -** [6,6]-Phenyl C_{71} butyric acid methyl ester

Molecular structures of dye molecules (organic and Inorganic), Pyrrole applied as counter electrode employed in the fabrication of dye-sensitized solar cells are depicted in Fig. A2

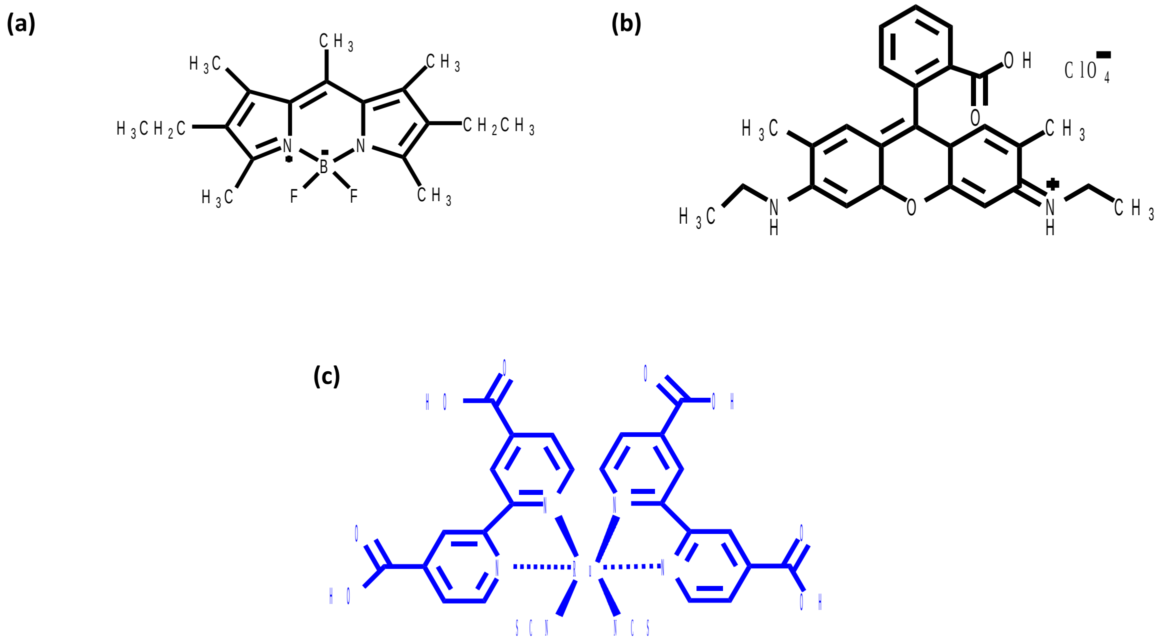

Figure A2: Molecular structures of (a) Bodipy, (b) RhCl, (c) N3 dyes employed in the present thesis work

(a) **BODIPY (PM567 dye) -** 4,4-difluoro-1,3,5,7,8-pentamethyl-2,6-diethyl-4-bora-3a,4adiaza- s-indecene

(b) **RhCl dye** – Rhodamine 19 Perchlorate

(c) **N3 dye** – cis-bis(isothiocyanato)bis(2,2'-bipyridyl-4,4'-dicarboxylato)-ruthenium(II)

A.2 Dye-loading of co-sensitized electrode

Dye loading of RhCl dye and N3 dye on TiO_2 photoanode

In order to find the no. of molecules of each dye adsorbed on a TiO_2 photoanode (co-sensitized electrode), we have carried out dye-loading experiments by desorbing the dyes in 0.1M potassium hydroxide (KOH) aqueous solution. UV-Vis spectra of N3 and RhCl dyes were recorded in 0.1 M KOH aqueous solution at different concentrations. The RhCl dye shows absorption peak at 510 nm while N3 dye shows peaks at 307 nm and 507 nm. The individual dye loading on co-sensitized TiO_2 surface was calculated using the fact that RhCl has negligible absorbance at lower wavelength (370nm), this absorbance was used to calculate the concentration of N3 dye.

N3 dye concentration = $A_{\text{Co-sensitized (370)}}/\epsilon_{(370, \text{N3})} = C_{\text{N3}}$

As $\epsilon_{(370, \text{N3})} = 0.42\times10^4\ M^{-1}cm^{-1}$, $C_{\text{N3}} = 100.4\ \mu M$

This provides the absorbance value at 504 nm from N3 alone.

$A_{\text{N3 (504)}} = C_{\text{N3}}\times\epsilon_{(504, \text{N3})} = 0.57$ as $\epsilon_{(504, \text{N3})} = 0.57\times10^4\ M^{-1}cm^{-1}$

The residual dye absorbance at 504 nm is now for RhCl alone:

$A_{\text{RhCl (504)}} = A_{\text{Co-sensitized (370)}} - A_{\text{N3 (504)}} = 0.69-0.57= 0.12$

Therefore, $C_{\text{RhCl}} = A_{\text{RhCl (504)}}/\epsilon_{(504, \text{RhCl})} = 0.53\mu M$

As $\epsilon_{(504, \text{RhCl})} = 2.28\times 10^5\ M^{-1}cm^{-1}$

In case of single N3 dye, the dye loading was calculated directly from absorbance at 504 nm.

The dye loading in case of co-sensitized as well as N3 dye sensitized TiO_2 electrode was then calculated as follows:

Dye Loading (mole/cm^2) = [Dye Concentration (in M) × Volume (ml)] / Electrode Area (cm^2)

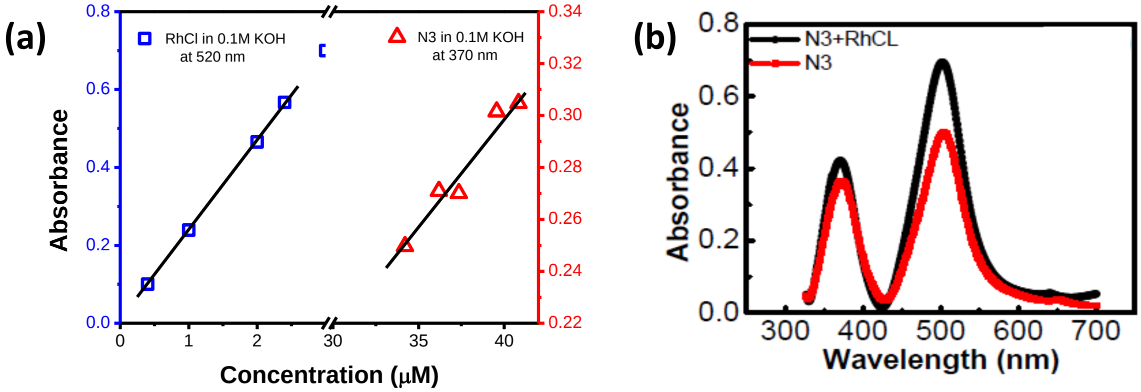

Figure A3: (a) Absorbance versus concentration of N3, and RhCl dye in 0.1 M KOH aqueous solution and (b) UV-Visible spectra of desorbed (i) co-sensitized electrode and (ii) N3 dye electrode of area 1 cm^2 in 3ml of 0.1 M KOH aqueous solution.

It was observed from the above calculations that the coverage of TiO_2 surface by RhCl dye is low (1.6×10^{-6}mol/ cm^2) as compared to that by N3 dye (3×10^{-4}mol/cm^2). The low coverage area of RhCl dye on TiO_2 electrode is advantageous as it leaves enough room for the sensitization of other dye (i.e., N3). Despite the low coverage of TiO_2 surface, RhCl works quite efficiently owing to its high molar extinction coefficient. In addition, it was observed that the amount of N3 dye absorbed on RhCl/TiO_2 electrode was 15% higher than that absorbed onto TiO_2 electrode (2.6×10^{-4} mole/cm^2).

References

[1] K. Kalyanasundaram, Dye-sensitized Solar Cells, EFPL Press2010.

[2] D.R. Myers, Solar Radiation: Practical Modeling for Renewable Energy Applications, Taylor & Francis2013.

[3] J.D. Servaites, M.A. Ratner, T.J. Marks, Organic solar cells: A new look at traditional models, Energy & Environmental Science, 4 (2011) 4410-4422.

[4] A. Goetzberger, J. Knobloch, B. Voss, Crystalline Silicon Solar Cells, Wiley1998.

[5] L.M. Fraas, L.D. Partain, Solar Cells and Their Applications, Wiley2010.

[6] I.M. Dharmadasa, Advances in Thin-Film Solar Cells, Pan Stanford2012.

[7] Y. Hamakawa, Thin-Film Solar Cells: Next Generation Photovoltaics and Its Applications, Springer2004.

[8] J. Poortmans, V. Arkhipov, Thin Film Solar Cells: Fabrication, Characterization and Applications, Wiley2006.

[9] C.W. Tang, Two-layer organic photovoltaic cell, Applied Physics Letters, 48 (1986) 183.

[10] B. O'regan, M. Grfitzeli, A low-cost, high-efficiency solar cell based on dye-sensitized, nature, 353 (1991) 24.

[11] A. Yella, H.-W. Lee, H.N. Tsao, C. Yi, A.K. Chandiran, M.K. Nazeeruddin, E.W.-G. Diau, C.-Y. Yeh, S.M. Zakeeruddin, M. Grätzel, Porphyrin-sensitized solar cells with cobalt (II/III)–based redox electrolyte exceed 12 percent efficiency, Science, 334 (2011) 629-634.

[12] H.S. Kim, S.H. Im, N.-G. Park, Organolead Halide Perovskite: New Horizons in Solar Cell Research, The Journal of Physical Chemistry C, (2014).

[13] C. Brabec, V. Dyakonov, U. Scherf, Organic Photovoltaics: Materials, Device Physics, and Manufacturing Technologies, Wiley2008.

[14] S. Günes, H. Neugebauer, N.S. Sariciftci, Conjugated polymer-based organic solar cells, Chemical Reviews, 107 (2007) 1324-1338.

[15] J.A. Hauch, P. Schilinsky, S.A. Choulis, R. Childers, M. Biele, C.J. Brabec, Flexible organic P3HT:PCBM bulk-heterojunction modules with more than 1 year outdoor lifetime, Solar Energy Materials and Solar Cells, 92 (2008) 727-731.

[16] M. Helgesen, R. Søndergaard, F.C. Krebs, Advanced materials and processes for polymer solar cell devices, Journal of Materials Chemistry, 20 (2010) 36-60.

[17] F.C. Krebs, Fabrication and processing of polymer solar cells: A review of printing and coating techniques, Solar Energy Materials and Solar Cells, 93 (2009) 394-412.

[18] F.C. Krebs, T. Tromholt, M. Jørgensen, Upscaling of polymer solar cell fabrication using full roll-to-roll processing, Nanoscale, 2 (2010) 873-886.

[19] P.W. Blom, V.D. Mihailetchi, L.J.A. Koster, D.E. Markov, Device physics of polymer: fullerene bulk heterojunction solar cells, Advanced Materials, 19 (2007) 1551-1566.

[20] S.E. Shaheen, C.J. Brabec, N.S. Sariciftci, F. Padinger, T. Fromherz, J.C. Hummelen, 2.5% efficient organic plastic solar cells, Applied Physics Letters, 78 (2001) 841-843.

[21] C.J. Brabec, S.E. Shaheen, C. Winder, N.S. Sariciftci, P. Denk, Effect of LiF/metal electrodes on the performance of plastic solar cells, Applied Physics Letters, 80 (2002) 1288-1290.

[22] G. Dennler, M.C. Scharber, C.J. Brabec, Polymer-Fullerene Bulk-Heterojunction Solar Cells, Advanced Materials, 21 (2009) 1323-1338.

[23] Y. Kim, S. Cook, S.M. Tuladhar, S.A. Choulis, J. Nelson, J.R. Durrant, D.D. Bradley, M. Giles, I. McCulloch, C.-S. Ha, A strong regioregularity effect in self-organizing conjugated polymer films and high-efficiency polythiophene: fullerene solar cells, Nature Materials, 5 (2006) 197-203.

[24] A. Gadisa, W.D. Oosterbaan, K. Vandewal, J.-C. Bolsée, S. Bertho, J. D'Haen, L. Lutsen, D. Vanderzande, J.V. Manca, Effect of Alkyl Side-Chain Length on Photovoltaic Properties of Poly(3-alkylthiophene)/PCBM Bulk Heterojunctions, Advanced Functional Materials, 19 (2009) 3300-3306.

[25] M. Svensson, F. Zhang, S.C. Veenstra, W.J.H. Verhees, J.C. Hummelen, J.M. Kroon, O. Inganäs, M.R. Andersson, High-Performance Polymer Solar Cells of an Alternating Polyfluorene Copolymer and a Fullerene Derivative, Advanced Materials, 15 (2003) 988-991.

[26] S.H. Park, A. Roy, S. Beaupré, S. Cho, N. Coates, J.S. Moon, D. Moses, M. Leclerc, K. Lee, A.J. Heeger, Bulk heterojunction solar cells with internal quantum efficiency approaching 100&percnt, Nature Photonics, 3 (2009) 297-302.

[27] J. Peet, J. Kim, N.E. Coates, W.L. Ma, D. Moses, A.J. Heeger, G.C. Bazan, Efficiency enhancement in low-bandgap polymer solar cells by processing with alkane dithiols, Nature materials, 6 (2007) 497-500.

[28] R.C. Coffin, J. Peet, J. Rogers, G.C. Bazan, Streamlined microwave-assisted preparation of narrow-bandgap conjugated polymers for high-performance bulk heterojunction solar cells, Nature chemistry, 1 (2009) 657-661.

[29] H. Zhou, L. Yang, A.C. Stuart, S.C. Price, S. Liu, W. You, Development of Fluorinated Benzothiadiazole as a Structural Unit for a Polymer Solar Cell of 7 % Efficiency, Angewandte Chemie International Edition, 50 (2011) 2995-2998.

[30] A. Breeze, A. Salomon, D. Ginley, B. Gregg, H. Tillmann, H.-H. Horhold, Polymer—perylene diimide heterojunction solar cells, Applied physics letters, 81 (2002) 3085-3087.

[31] S.A. Jenekhe, S. Yi, Efficient photovoltaic cells from semiconducting polymer heterojunctions, Applied Physics Letters, 77 (2000) 2635-2637.

[32] J. Halls, R. Friend, The photovoltaic effect in a poly (p-phenylenevinylene)/perylene heterojunction, Synthetic metals, 85 (1997) 1307-1308.

[33] G. Yu, J. Gao, J.C. Hummelen, F. Wudl, A.J. Heeger, Polymer Photovoltaic Cells: Enhanced Efficiencies via a Network of Internal Donor-Acceptor Heterojunctions, Science, 270 (1995) 1789-1791.

[34] C. Yang, A. Heeger, Morphology of composites of semiconducting polymers mixed with C< sub> 60</sub>, Synthetic metals, 83 (1996) 85-88.

[35] W. Ma, C. Yang, X. Gong, K. Lee, A.J. Heeger, Thermally stable, efficient polymer solar cells with nanoscale control of the interpenetrating network morphology, Advanced Functional Materials, 15 (2005) 1617-1622.

[36] D.R. Kozub, K. Vakhshouri, L.M. Orme, C. Wang, A. Hexemer, E.D. Gomez, Polymer crystallization of partially miscible polythiophene/fullerene mixtures controls morphology, Macromolecules, 44 (2011) 5722-5726.

[37] R.A.J. Janssen, J. Nelson, Factors Limiting Device Efficiency in Organic Photovoltaics, Advanced Materials, 25 (2013) 1847-1858.

[38] L.J.A. Koster, V.D. Mihailetchi, P.W.M. Blom, Ultimate efficiency of polymer/fullerene bulk heterojunction solar cells, Applied Physics Letters, 88 (2006).

[39] D. Chirvase, Z. Chiguvare, M. Knipper, J. Parisi, V. Dyakonov, J.C. Hummelen, Temperature dependent characteristics of poly(3 hexylthiophene)-fullerene based heterojunction organic solar cells, Journal of Applied Physics, 93 (2003) 3376-3383.

[40] G. Li, V. Shrotriya, J. Huang, Y. Yao, T. Moriarty, K. Emery, Y. Yang, High-efficiency solution processable polymer photovoltaic cells by self-organization of polymer blends, Nature Materials, 4 (2005) 864-868.

[41] G. Li, Y. Yao, H. Yang, V. Shrotriya, G. Yang, Y. Yang, “Solvent Annealing” Effect in Polymer Solar Cells Based on Poly(3-hexylthiophene) and Methanofullerenes, Advanced Functional Materials, 17 (2007) 1636-1644.

[42] C.C. Lin, Y.Y. Lin, S.S. Li, C.C. Yu, C.L. Huang, S.H. Lee, C.H. Du, J.J. Lee, H.L. Chen, C.W. Chen, Electric field-assisted self-organization of polymer: Fullerene hybrids on the photovoltaic performance, Energy and Environmental Science, 4 (2011) 2134-2139.

[43] J.S. Kim, Y. Park, D.Y. Lee, J.H. Lee, J.H. Park, J.K. Kim, K. Cho, Poly(3-hexylthiophene) nanorods with aligned chain orientation for organic photovoltaics, Advanced Functional Materials, 20 (2010) 540-545.

[44] M. Reyes-Reyes, K. Kim, D.L. Carroll, High-efficiency photovoltaic devices based on annealed poly(3-hexylthiophene) and 1-(3-methoxycarbonyl)-propyl-1- phenyl-(6,6)C61 blends, Applied Physics Letters, 87 (2005) -.

[45] F. Gao, S. Ren, J. Wang, The renaissance of hybrid solar cells: progresses, challenges, and perspectives, Energy & Environmental Science, 6 (2013) 2020-2040.

[46] M. Granström, K. Petritsch, A. Arias, A. Lux, M. Andersson, R. Friend, Laminated fabrication of polymeric photovoltaic diodes, Nature, 395 (1998) 257-260.

[47] L. Chen, D. Godovsky, O. Inganäs, J.C. Hummelen, R. Janssens, M. Svensson, M.R. Andersson, Polymer photovoltaic devices from stratified multilayers of donor–acceptor blends, Advanced Materials, 12 (2000) 1367-1370.

[48] C. Brabec, A. Cravino, D. Meissner, N. Sariciftci, M. Rispens, L. Sanchez, J. Hummelen, T. Fromherz, The influence of materials work function on the open circuit voltage of plastic solar cells, Thin Solid Films, 403 (2002) 368-372.

[49] M. Drees, K. Premaratne, W. Graupner, J. Heflin, R. Davis, D. Marciu, M. Miller, Creation of a gradient polymer-fullerene interface in photovoltaic devices by thermally controlled interdiffusion, Applied physics letters, 81 (2002) 4607-4609.

[50] F.J. Knorr, D. Zhang, J.L. McHale, Influence of TiCl4 treatment on surface defect photoluminescence in pure and mixed-phase nanocrystalline TiO2, Langmuir, 23 (2007) 8686-8690.

[51] S. Ito, T.N. Murakami, P. Comte, P. Liska, C. Grätzel, M.K. Nazeeruddin, M. Grätzel, Fabrication of thin film dye sensitized solar cells with solar to electric power conversion efficiency over 10%, Thin Solid Films, 516 (2008) 4613-4619.

[52] U. Ozgur, Y.I. Alivov, C. Liu, A. Teke, M. Reshchikov, S. Dogan, V. Avrutin, S.-J. Cho, H. Morkoc, A comprehensive review of ZnO materials and devices, Journal of applied physics, 98 (2005) 041301-041301-041103.

[53] K. Keis, J. Lindgren, S.-E. Lindquist, A. Hagfeldt, Studies of the adsorption process of Ru complexes in nanoporous ZnO electrodes, Langmuir, 16 (2000) 4688-4694.

[54] M. Durr, A. Bamedi, A. Yasuda, G. Nelles, Tandem dye-sensitized solar cell for improved power conversion efficiencies, Applied Physics Letters, 84 (2004) 3397-3399.

[55] L. Li, Y. Hao, X. Yang, J. Zhao, H. Tian, C. Teng, A. Hagfeldt , L. Sun A Double-Band Tandem Organic Dye-sensitized Solar Cell with an Efficiency of 11.5 %, ChemSusChem, 4 (2011) 609-612.

[56] K. Sayama, S. Tsukagoshi, T. Mori, K. Hara, Y. Ohga, A. Shinpou, Y. Abe, S. Suga, H. Arakawa, Efficient sensitization of nanocrystalline TiO2 films with cyanine and merocyanine organic dyes, Solar Energy Materials and Solar Cells, 80 (2003) 47-71.

[57] A. Ehret, L. Stuhl, M.T. Spitler, Spectral Sensitization of TiO2 Nanocrystalline Electrodes with Aggregated Cyanine Dyes, The Journal of Physical Chemistry B, 105 (2001) 9960-9965.

[58] Z.-S. Wang, T. Yamaguchi, H. Sugihara, H. Arakawa, Significant Efficiency Improvement of the Black Dye-Sensitized Solar Cell through Protonation of TiO2 Films, Langmuir, 21 (2005) 4272-4276.

[59] F. Inakazu, Y. Noma, Y. Ogomi, S. Hayase, Dye-sensitized solar cells consisting of dye-bilayer structure stained with two dyes for harvesting light of wide range of wavelength, Applied Physics Letters, 93 (2008) 093304-093303.

[60] E. Palomares, J.N. Clifford, S.A. Haque, T. Lutz, J.R. Durrant, Slow charge recombination in dye-sensitised solar cells (DSSC) using Al2O3 coated nanoporous TiO2 films, Chemical Communications, (2002) 1464-1465.

[61] D. Shi, N. Pootrakulchote, R. Li, J. Guo, Y. Wang, S.M. Zakeeruddin, M. Grätzel, P. Wang, New Efficiency Records for Stable Dye-Sensitized Solar Cells with Low-Volatility and Ionic Liquid Electrolytes, The Journal of Physical Chemistry C, 112 (2008) 17046-17050.

[62] E. Olsen, G. Hagen, S. Eric Lindquist, Dissolution of platinum in methoxy propionitrile containing LiI/I2, Solar Energy Materials and Solar Cells, 63 (2000) 267-273.

[63] S. Ahmad, J.-H. Yum, Z. Xianxi, M. Gratzel, H.-J. Butt, M.K. Nazeeruddin, Dye-sensitized solar cells based on poly (3,4-ethylenedioxythiophene) counter electrode derived from ionic liquids, Journal of Materials Chemistry, 20 (2010) 1654-1658.

[64] K.M. Lee, C.Y. Hsu, P.Y. Chen, M. Ikegami, T. Miyasaka, K.C. Ho, Highly porous PProDOT-Et2 film as counter electrode for plastic dye-sensitized solar cells, Physical chemistry chemical physics : PCCP, 11 (2009) 3375-3379.

[65] S. Cho, S.H. Hwang, C. Kim, J. Jang, Polyaniline porous counter-electrodes for high performance dye-sensitized solar cells, Journal of Materials Chemistry, 22 (2012) 12164-12171.

[66] J. Wu, Q. Li, L. Fan, Z. Lan, P. Li, J. Lin, S. Hao, High-performance polypyrrole nanoparticles counter electrode for dye-sensitized solar cells, Journal of Power Sources, 181 (2008) 172-176.

[67] J. Xia, L. Chen, S. Yanagida, Application of polypyrrole as a counter electrode for a dye-sensitized solar cell, Journal of Materials Chemistry, 21 (2011) 4644-4649.

[68] Z. Li, B. Ye, X. Hu, X. Ma, X. Zhang, Y. Deng, Facile electropolymerized-PANI as counter electrode for low cost dye-sensitized solar cell, Electrochemistry Communications, 11 (2009) 1768-1771.

[69] J.M. Kroon, N.J. Bakker, H.J.P. Smit, P. Liska, K.R. Thampi, P. Wang, S.M. Zakeeruddin, M. Grätzel, A. Hinsch, S. Hore, U. Würfel, R. Sastrawan, J.R. Durrant, E. Palomares, H. Pettersson, T. Gruszecki, J. Walter, K. Skupien, G.E. Tulloch, Nanocrystalline dye-sensitized solar cells having maximum performance, Progress in Photovoltaics: Research and Applications, 15 (2007) 1-18.

[70] M. Ghosh, R. Bhattacharyya, A. Raychaudhuri, Growth of compact arrays of optical quality single crystalline ZnO nanorods by low temperature method, Bulletin of Materials Science, 31 (2008) 283-289.

[71] N. Ramgir, M. Ghosh, P. Veerender, N. Datta, M. Kaur, D. Aswal, S. Gupta, Growth and gas sensing characteristics of p-and n-type ZnO nanostructures, Sensors and Actuators B: Chemical, 156 (2011) 875-880.

[72] A. Sugunan, H. Warad, M. Boman, J. Dutta, Zinc oxide nanowires in chemical bath on seeded substrates: Role of hexamine, J Sol-Gel Sci Technol, 39 (2006) 49-56.

[73] P. Veerender, V. Saxena, A. Chauhan, S. Koiry, P. Jha, A. Gusain, S. Choudhury, D. Aswal, S. Gupta, Probing the annealing induced molecular ordering in bulk heterojunction polymer solar cells using in-situ Raman spectroscopy, Solar Energy Materials and Solar Cells, 120 (2014) 526-535.

[74] M.O. Reese, M.S. White, G. Rumbles, D.S. Ginley, S.E. Shaheen, Optimal negative electrodes for poly(3-hexylthiophene): [6,6]-phenyl C61-butyric acid methyl ester bulk heterojunction photovoltaic devices, Applied Physics Letters, 92 (2008).

[75] C. Zhang, J. Zhang, Y. Hao, Z. Lin, C. Zhu, A simple and efficient solar cell parameter extraction method from a single current-voltage curve, Journal of Applied Physics, 110 (2011) 064504-064511.

[76] P. Boland, S.S. Sunkavalli, S. Chennuri, K. Foe, T. Abdel-Fattah, G. Namkoong, Investigation of structural, optical, and electrical properties of regioregular poly(3-hexylthiophene)/fullerene blend nanocomposites for organic solar cells, Thin Solid Films, 518 (2010) 1728-1731.

[77] A.J. Pearson, T. Wang, R.A.L. Jones, D.G. Lidzey, P.A. Staniec, P.E. Hopkinson, A.M. Donald, Rationalizing phase transitions with thermal annealing temperatures for P3HT:PCBM organic photovoltaic devices, Macromolecules, 45 (2012) 1499-1508.

[78] F. Zhang, Z. Zhuo, J. Zhang, X. Wang, X. Xu, Z. Wang, Y. Xin, J. Wang, J. Wang, W. Tang, Z. Xu, Y. Wang, Influence of PC60BM or PC70BM as electron acceptor on the

performance of polymer solar cells, Solar Energy Materials and Solar Cells, 97 (2012) 71-77.

[79] A.M. Ballantyne, T.A.M. Ferenczi, M. Campoy-Quiles, T.M. Clarke, A. Maurano, K.H. Wong, W. Zhang, N. Stingelin-Stutzmann, J.S. Kim, D.D.C. Bradley, J.R. Durrant, I. McCulloch, M. Heeney, J. Nelson, S. Tierney, W. Duffy, C. Mueller, P. Smith, Understanding the influence of morphology on poly(3-hexylselenothiophene): PCBM solar cells, Macromolecules, 43 (2010) 1169-1174.

[80] W.C. Tsoi, D.T. James, J.S. Kim, P.G. Nicholson, C.E. Murphy, D.D.C. Bradley, J. Nelson, J.S. Kim, The nature of in-plane skeleton Raman modes of P3HT and their correlation to the degree of molecular order in P3HT:PCBM blend thin films, Journal of the American Chemical Society, 133 (2011) 9834-9843.

[81] Y. Gao, J.K. Grey, Resonance chemical imaging of polythiophene/fullerene photovoltaic thin films: Mapping morphology-dependent aggregated and unaggregated C=C species, Journal of the American Chemical Society, 131 (2009) 9654-9662.

[82] C. Carach, I. Riisness, M.J. Gordon, Raman and low temperature photoluminescence spectroscopy of polymer disorder in bulk heterojunction solar cell films, Applied Physics Letters, 101 (2012) 083302-083307.

[83] G. Sun, M. Kertesz, Vibrational Raman spectra of C70 and C70 6- studied by density functional theory, Journal of Physical Chemistry A, 106 (2002) 6381-6386.

[84] S. Miller, G. Fanchini, Y.Y. Lin, C. Li, C.W. Chen, W.F. Su, M. Chhowalla, Investigation of nanoscale morphological changes in organic photovoltaics during solvent vapor annealing, Journal of Materials Chemistry, 18 (2008) 306-312.

[85] M. Campoy-Quiles, T. Ferenczi, T. Agostinelli, P.G. Etchegoin, Y. Kim, T.D. Anthopoulos, P.N. Stavrinou, D.D.C. Bradley, J. Nelson, Morphology evolution via self-organization and lateral and vertical diffusion in polymer:fullerene solar cell blends, Nature Materials, 7 (2008) 158-164.

[86] X. Yang, J. Loos, S.C. Veenstra, W.J.H. Verhees, M.M. Wienk, J.M. Kroon, M.A.J. Michels, R.A.J. Janssen, Nanoscale morphology of high-performance polymer solar cells, Nano Letters, 5 (2005) 579-583.

[87] H. Hoppe, M. Niggemann, C. Winder, J. Kraut, R. Hiesgen, A. Hinsch, D. Meissner, N.S. Sariciftci, Nanoscale morphology of conjugated polymer/fullerene-based bulk-heterojunction solar cells, Advanced Functional Materials, 14 (2004) 1005-1011.

[88] J.W. Kiel, B.J. Kirby, C.F. Majkrzak, B.B. Maranville, M.E. MacKay, Nanoparticle concentration profile in polymer-based solar cells, Soft Matter, 6 (2010) 641-646.

[89] V. Shrotriya, J. Ouyang, R.J. Tseng, G. Li, Y. Yang, Absorption spectra modification in poly(3-hexylthiophene):methanofullerene blend thin films, Chemical Physics Letters, 411 (2005) 138-143.

[90] Y.C. Huang, Y.C. Liao, S.S. Li, M.C. Wu, C.W. Chen, W.F. Su, Study of the effect of annealing process on the performance of P3HT/PCBM photovoltaic devices using scanning-probe microscopy, Solar Energy Materials and Solar Cells, 93 (2009) 888-892.

[91] D. Chirvase, J. Parisi, J.C. Hummelen, V. Dyakonov, Influence of nanomorphology on the photovoltaic action of polymer-fullerene composites, Nanotechnology, 15 (2004) 1317-1323.

[92] S.A. Hawks, G. Li, Y. Yang, R.A. Street, Band tail recombination in polymer:fullerene organic solar cells, Journal of Applied Physics, 116 (2014) 074503-074514.

[93] S. Koiry, M. Celestin, R. Ratnadurai, P. Veerender, C. Majumder, S. Krishnan, E. Stefanakos, Y. Goswami, D. Aswal, S. Bhansali, Ferroeletric like characteristics in redox active polymer of 5, 10, 15, 20 tetra (4-hydroxyphenyl)-porphyrin at room temperature, Applied Physics Letters, 103 (2013) 033302-033305.

[94] P. Veerender, S. Koiry, V. Saxena, P. Jha, A. Chauhan, D. Aswal, S. Gupta, Electrochemical polymerization of tetra-(4-hydroxyphenyl) porphyrin for organic solar cells, AIP Conference Proceedings, 1447 (2012) 727.

[95] N.C. Maiti, S. Mazumdar, N. Periasamy, J- and H-Aggregates of Porphyrin−Surfactant Complexes: Time-Resolved Fluorescence and Other Spectroscopic Studies†, The Journal of Physical Chemistry B, 102 (1998) 1528-1538.

[96] T.J. Savenije, R.B.M. Koehorst, T.J. Schaafsma, Spectroelectrochemical Measurement of Charge Transport Properties of Electropolymerized Tetrakis(hydroxyphenyl)porphyrins, The Journal of Physical Chemistry B, 101 (1997) 720-725.

[97] J. Humphrey, D. Kuciauskas, Charge-Transfer States Determine Iron Porphyrin Film Third-Order Nonlinear Optical Properties in the near-IR Spectral Region, The Journal of Physical Chemistry B, 108 (2004) 12016-12023.

[98] P. Veerender, S. Koiry, P. Jha, V. Saxena, A. Chauhan, S. Bhattacharya, R. Tewari, D. Aswal, S. Gupta, An Electrochemical Approach for Deposition of Polyfullerene Films on ITO Substrates, Journal of The Electrochemical Society, 159 (2011) D13-D18.

[99] C. Caron, R. Subramanian, F. D'Souza, J. Kim, W. Kutner, M.T. Jones, K.M. Kadish, Selective electrosynthesis of dimethylfullerene [(CH3)2C60]: a novel method for the controlled functionalization of fullerenes, Journal of the American Chemical Society, 115 (1993) 8505-8506.

[100] D. Dubois, K.M. Kadish, S. Flanagan, L.J. Wilson, Electrochemical detection of fulleronium and highly reduced fulleride (C605-) ions in solution, Journal of the American Chemical Society, 113 (1991) 7773-7774.

[101] D. Dubois, G. Moninot, W. Kutner, M.T. Jones, K.M. Kadish, Electroreduction of Buckminsterfullerene, C60, in aprotic solvents. Solvent, supporting electrolyte, and temperature effects, The Journal of Physical Chemistry, 96 (1992) 7137-7145.

[102] I. Noviandri, R.D. Bolskar, P.A. Lay, C.A. Reed, Solvent Effects on the Electrochemistry of C60. Thermodynamics of Solvation of C60 and Fullerides, The Journal of Physical Chemistry B, 101 (1997) 6350-6358.

[103] D.R. Lawson, D.L. Feldheim, C.A. Foss, P.K. Dorhout, C.M. Elliott, C.R. Martin, B. Parkinson, Near-IR Absorption Spectra for the Buckminsterfullerene Anions: an Experimental and Theoretical Study, Journal of The Electrochemical Society, 139 (1992) L68-L71.

[104] M.S. Dresselhaus, G. Dresselhaus, A.M. Rao, P.C. Eklund, Optical properties of C60 and related materials, Synthetic Metals, 78 (1996) 313-325.

[105] K. Winkler, D.A. Costa, W.R. Fawcett, A.L. Balch, Alteration of the electrochemistry of fullerene C60 in the presence of dioxygen: Formation of a redox-active polymeric film, Advanced Materials, 9 (1997) 153-156.

[106] P. Strasser, M. Ata, Electrochemical Synthesis of Polymerized LiC60 Films, The Journal of Physical Chemistry B, 102 (1998) 4131-4134.

[107] B. Ma, A.M. Milton, Y.-P. Sun, Infrared spectroscopy of all-carbon poly[60]fullerene polymer and [60]fullerene dimer model, Chemical Physics Letters, 288 (1998) 854-860.

[108] J. Onoe, K. Takeuchi, In situ high-resolution infrared spectroscopy of a photopolymerized C_{60} film, Physical Review B, 54 (1996) 6167-6171.

[109] A.M. Rao, P.C. Eklund, J.L. Hodeau, L. Marques, M. Nunez-Regueiro, Infrared and Raman studies of pressure-polymerized C_{60}s, Physical Review B, 55 (1997) 4766-4773.

[110] T. Takahashi, S. Suzuki, T. Morikawa, H. Katayama-Yoshida, S. Hasegawa, H. Inokuchi, K. Seki, K. Kikuchi, S. Suzuki, K. Ikemoto, Y. Achiba, Pseudo-gap at the Fermi level in K_{3}C_{60} observed by photoemission and inverse photoemission, Physical Review Letters, 68 (1992) 1232-1235.

[111] G. Gensterblum, K. Hevesi, B.Y. Han, L.M. Yu, J.J. Pireaux, P.A. Thiry, R. Caudano, A.A. Lucas, D. Bernaerts, S. Amelinckx, G. Van Tendeloo, G. Bendele, T. Buslaps, R.L. Johnson, M. Foss, R. Feidenhans'l, G. Le Lay, Growth mode and electronic structure of the epitaxial C_{60}(111)/GeS(001) interface, Physical Review B, 50 (1994) 11981-11995.

[112] A. Trave, F.J. Ribeiro, S.G. Louie, M.L. Cohen, Energetics and structural characterization of C_{60} polymerization in BN and carbon nanopeapods, Physical Review B, 70 (2004) 205418.

[113] H.L. Zhang, W. Chen, L. Chen, H. Huang, X.S. Wang, J. Yuhara, A.T.S. Wee, C60 Molecular Chains on α-Sexithiophene Nanostripes, Small, 3 (2007) 2015-2018.

[114] Y. Pennec, W. Auwärter, A. Schiffrin, A. Weber-Bargioni, A. Riemann, J. Barth, Supramolecular gratings for tuneable confinement of electrons on metal surfaces, Nature nanotechnology, 2 (2007) 99-103.

[115] M. Rajalakshmi, A.K. Arora, B.S. Bendre, S. Mahamuni, Optical phonon confinement in zinc oxide nanoparticles, Journal of Applied Physics, 87 (2000) 2445-2448.

[116] C.F. Klingshirn, A. Waag, A. Hoffmann, J. Geurts, Zinc Oxide: From Fundamental Properties Towards Novel Applications, Springer2010.

[117] P. Veerender, A. Jain, A. Gusain, V. Saxena, D. Aswal, S. Gupta, Dye Sensitized Solar Cells Based On Metal-Free Organic Dyes and Aqueous Electrolytes, Fuelling the Future: Advances in Science and Technologies for Energy Generation, Transmission and Storage, (2012) 168.

[118] M.K. Nazeeruddin, A. Kay, I. Rodicio, R. Humphry-Baker, E. Mueller, P. Liska, N. Vlachopoulos, M. Graetzel, Conversion of light to electricity by cis-X2bis(2,2'-bipyridyl-4,4'-dicarboxylate)ruthenium(II) charge-transfer sensitizers (X = Cl-, Br-, I-, CN-, and SCN-) on nanocrystalline titanium dioxide electrodes, Journal of the American Chemical Society, 115 (1993) 6382-6390.

[119] P.J. Cameron, L.M. Peter, How Does Back-Reaction at the Conducting Glass Substrate Influence the Dynamic Photovoltage Response of Nanocrystalline Dye-Sensitized Solar Cells?, The Journal of Physical Chemistry B, 109 (2005) 7392-7398.

[120] C. Law, S.C. Pathirana, X. Li, A.Y. Anderson, P.R.F. Barnes, A. Listorti, T.H. Ghaddar, B.C. O′Regan, Water-Based Electrolytes for Dye-Sensitized Solar Cells, Advanced Materials, 22 (2010) 4505-4509.

[121] V. Saxena, P. Veerender, A. Chauhan, P. Jha, D. Aswal, S. Gupta, Efficiency enhancement in dye sensitized solar cells through co-sensitization of TiO< inf> 2</inf> nanocrystalline electrodes, Applied Physics Letters, 100 (2012) 133303-133303-133304.

[122] J.R.S. Brownson, M.I. Tejedor-Tejedor, M.A. Anderson, FTIR Spectroscopy of Alcohol and Formate Interactions with Mesoporous TiO2 Surfaces, The Journal of Physical Chemistry B, 110 (2006) 12494-12499.

[123] K. Goto, T. Kawashima, N. Tanabe, Heat-resisting TCO films for PV cells, Solar Energy Materials and Solar Cells, 90 (2006) 3251-3260.

[124] C. Sima, C. Grigoriu, S. Antohe, Comparison of the dye-sensitized solar cells performances based on transparent conductive ITO and FTO, Thin Solid Films, 519 (2010) 595-597.

[125] L. Han, N. Koide, Y. Chiba, T. Mitate, Modeling of an equivalent circuit for dye-sensitized solar cells, Applied Physics Letters, 84 (2004) 2433-2435.

[126] P. Veerender, V. Saxena, A. Gusain, P. Jha, S. Koiry, A. Chauhan, D. Aswal, S. Gupta, Effect of Co-sensitization and acid treatment on TiO photoanodes in dye-sensitized solar cells, AIP Conference Proceedings, 1512 (2013) 778.

[127] P. Veerender, V. Saxena, A. Gusain, S. Koiry, P. Jha, A. Chauhan, D. Aswal, S. Gupta, A simple method for increasing the efficiency of Rhodamine 19 perchlorate based dye sensitized solar cells, Nanoenergy Symposia, 12 (2013) 163.

[128] P. Veerender, V. Saxena, P. Jha, S. Koiry, A. Gusain, S. Samanta, A. Chauhan, D. Aswal, S. Gupta, Free-standing polypyrrole films as substrate-free and Pt-free counter electrodes for quasi-solid dye-sensitized solar cells, Organic Electronics, 13 (2012) 3032-3039.

[129] S.P. Koiry, V. Saxena, D. Sutar, S. Bhattacharya, D.K. Aswal, S.K. Gupta, J.V. Yakhmi, Interfacial synthesis of long polyindole fibers, Journal of Applied Polymer Science, 103 (2007) 595-599.

[130] S.S. Jeon, C. Kim, J. Ko, S.S. Im, Spherical polypyrrole nanoparticles as a highly efficient counter electrode for dye-sensitized solar cells, Journal of Materials Chemistry, 21 (2011) 8146-8151.

[131] S.S. Jeon, H.H. An, C.S. Yoon, S.S. Im, Synthesis of ultra-thin polypyrrole nanosheets for chemical sensor applications, Polymer, 52 (2011) 652-657.

[132] J. Lei, Z. Cai, C.R. Martin, Effect of reagent concentrations used to synthesize polypyrrole on the chemical characteristics and optical and electronic properties of the resulting polymer, Synthetic Metals, 46 (1992) 53-69.

[133] Z. Zhang, P. Chen, T.N. Murakami, S.M. Zakeeruddin, M. Grätzel, The 2,2,6,6-Tetramethyl-1-piperidinyloxy Radical: An Efficient, Iodine- Free Redox Mediator for Dye-Sensitized Solar Cells, Advanced Functional Materials, 18 (2008) 341-346.

[134] C.-K. Hsieh, M.-C. Tsai, C.-Y. Su, S.-Y. Wei, M.-Y. Yen, C.-C.M. Ma, F.-R. Chen, C.-H. Tsai, A hybrid nanostructure of platinum-nanoparticles/graphitic-nanofibers as a three-dimensional counter electrode in dye-sensitized solar cells, Chemical Communications, 47 (2011) 11528-11530.

[135] T. Makris, V. Dracopoulos, T. Stergiopoulos, P. Lianos, A quasi solid-state dye-sensitized solar cell made of polypyrrole counter electrodes, Electrochimica Acta, 56 (2011) 2004-2008.

[136] N. Wang, H. Lin, J. Li, X. Li, Improved quasi-solid dye-sensitized solar cells by composite ionic liquid electrolyte including layered alpha-zirconium phosphate, Applied Physics Letters, 89 (2006) 194104-194103.

[137] S.Y. Huang, G. Schlichthörl, A.J. Nozik, M. Grätzel, A.J. Frank, Charge Recombination in Dye-Sensitized Nanocrystalline TiO2 Solar Cells, The Journal of Physical Chemistry B, 101 (1997) 2576-2582.

[138] F. Nunzi, E. Mosconi, L. Storchi, E. Ronca, A. Selloni, M. Gratzel, F. De Angelis, Inherent electronic trap states in TiO2 nanocrystals: effect of saturation and sintering, Energy & Environmental Science, 6 (2013) 1221-1229.